SPECTROSCOPIC PROPERTIES OF $PbMoO_4$ AND $PbWO_4$ SINGLE CRYSTALS DOPED WITH Pr^{3+} AND Nd^{3+}
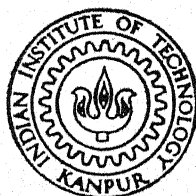
By

BHANU PRATAP SINGH

DEPARTMENT OF PHYSICS

INDIAN INSTITUTE OF TECHNOLOGY KANPUR

AUGUST, 1983

SPECTROSCOPIC PROPERTIES OF PbMoO$_4$ AND PbWO$_4$
SINGLE CRYSTALS DOPED WITH Pr^{3+} AND Nd^{3+}

A Thesis Submitted
In Partial Fulfilment of the Requirements
for the Degree of

DOCTOR OF PHILOSOPHY

By

BHANU PRATAP SINGH

to the
DEPARTMENT OF PHYSICS
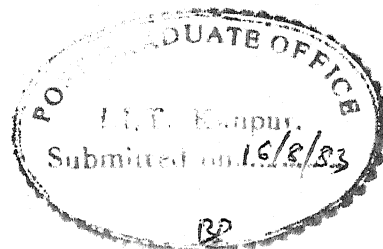INDIAN INSTITUTE OF TECHNOLOGY KANPUR
AUGUST, 1983

PHY-1983-$\boxtimes$-SIN-SPE

IN

THE HALLOWED MEMORY

OF

SRI C.P.K. REDDY

Twenty five times have I encircled the

Blazing sun, and many times more has the

Moon encircled my smallness; yet, I have

Not learned the secrets of light, neither

Do I comprehend the mystery of darkness.

<div align="right">— Khalil Gibran</div>

CERTIFICATE

Certified that the work 'SPECTROSCOPIC PROPERTIES OF $PbMoO_4$ AND $PbWO_4$ SINGLE CRYSTALS DOPED WITH Pr^{3+} AND Nd^{3+}' has been carried out by Mr. B.P. Singh under my supervision and that the same has not been submitted elsewhere for a degree.

K K Sharma

K.K. Sharma
Assistant Professor
Department of Physics

August 16, 1983

ACKNOWLEDGEMENT

to Mr. J.S. Sharma, Mr. Ram Singh and all other members of Physics Workshop for their involvement in the work at various stages;

Finally to Mr. K.N. Islam for the meticulous typing of rather difficult manuscript and Mr. Lallu Singh Rathaur, Mr. H.K. Panda and Mr. Dilip for cyclostyling and xeroxing.

In the end I bow my head to my parents.

BHANU PRATAP SINGH
Department of Physics
IIT - Kanpur

CONTENTS

Page

LIST OF FIGURES

SYNOPSIS

Bhanu Pratap Singh
Ph.D.
Department of Physics
Indian Institute of Technology, Kanpur, India
May 1983

SPECTROSCOPIC PROPERTIES OF $PbMoO_4$ AND $PbWO_4$
SINGLE CRYSTALS DOPED WITH Pr^{3+} AND Nd^{3+}

In this thesis, the results of an investigation
undertaken to interpret the absorption, fluorescence and
Raman spectra of single crystals of $PbMoO_4$ and $PbWO_4$
doped with Pr^{3+} and Nd^{3+} are reported. These host crys-
tals belong to the scheelite family.

Samples for spectroscopic measurements were cut from
large size single crystals grown by Czochralski technique
in our laboratory. A resistance type furnace with a sta-
bilised D.C. power supply (1.5 KVA) was constructed. A
cold finger glass dewar was fabricated for spectroscopic
measurements at low temperatures. The fluorescence and
Raman scattering measurements were carried out using an
Ar^+ ion laser, a double monochromator and a lock in ampli-
fier. Asbsorption studies were carried out using the
same monochromator and lock in amplifier. A 1000 watts

water cooled tungsten halogen lamp was used as a white
light source. A signal controller was fabricated to control
the base line in absorption measurements. Polarized
fluorescence, absorption and Raman spectra of the samples
were recorded at liq. N_2 temperature. These samples when
excited with blue lines of Ar^+ ion laser (488 nm, 476.5 nm
and 457.9 nm) exhibit a very strong visible fluorescence.
Nd^{3+} ion is not known to give any fluorescence in the
visible region in other scheelite crystals. Analysis of
the fluorescence and absorption data established that the
observed visible fluorescence is due to Pr^{3+} impurity.
We have estimated Pr^{3+} concentration in the samples to
be less than 1 ppm. Attempts to determine this concen-
tration by atomic absorption and PIXE techniques were
however unsuccessful. The near IR fluorescence has been
attributed to Nd^{3+} and Pr^{3+} ions. Based on the fluore-
scence and absorption data, energy level schemes for Pr^{3+}
and Nd^{3+} have been constructed. Observed crystal field
splittings for Nd^{3+} are in good agreement with the earlier
works.

Unusually strong fluorescence of Pr^{3+} from such
dilute samples prompted us to undertake a detailed quan-
titative analysis of its fluorescence and absorption data.
To our knowledge, observation of a strong visible fluore-
scence and crystal field parameters for Pr^{3+} in molybdate
and tungstate scheelite hosts are being presented here

for the first time. The basic theoretical approach followed here for the interpretation of the absorption and fluorescence data is to parameterize quantities which can not be obtained from ab-initio calculations. The angular parts of the matrix elements are calculated exactly and radial parts are treated as adjustable parameters in an effort to match the experimental and theoretical results. Free ion levels are obtained from the 'centres of gravity' of the observed groups of lines. The free ion and crystal field radial parameters have been calculated.

The Raman measurements were helpful in sorting out the interfering Raman lines in the fluorescence spectrum. Symmetry of the vibrations have been assigned and compared with earlier works on these and other similar crystals.

Chapter I contains some introductory remarks on the crystal spectra of rare earths and a few comments on the specific system of interest i.e. $PbMO_4:Pr^{3+}$ and Nd^{3+} (where M = Mo or W). It has been pointed out that Pr^{3+} ion which has not received sufficient attention in the past may be useful for solid state laser applications. The approach followed for the interpretation of the data has been briefly outlined.

Chapter II gives an account of the experimental details and contains the experimental data.

In chapter III theoretical details relevant to the present investigation are presented.

Chapter IV presents the results of our calculations using the framework of Chapter III and experimental data of Chapter II.

The significance and the scope of the results obtained are discussed in the fifth and final chapter.

The details of calculations and programming are given in the appendix.

CHAPTER I

INTRODUCTION

Elements of the lanthanide series possess the Xe Core Structure $(1s^2\ 2s^2\ 2p^6\ 3s^2\ 3p^6\ 3d^{10}\ 4s^2\ 4p^6\ 4d^{10}\ 5s^2\ 5p^6)$, $4f^N$ electrons and two or three loosely bound outer electrons. In the crystal spectra of rare-earths, one is primarily concerned with the triply ionized atoms. These ions possess 4f electrons besides the Xe core.

In 1907 Becquerel[1] could for the first time resolve the bands in the spectra of crystalline lanthanide compounds at low temperature. In 1929 Bethe[2] published the theory for term splitting which results from the influence of the crystalline electric field of a given symmetry. Due to difficulties in preparing high purity lanthanide compounds, it could only be possible in 1934 to obtain some of the lanthanide's solution absorption spectra[3]. Racah in 1942 developed the tensor operator techniques[4] and Stevens in 1952 the equivalent operator techniques[5] for the theoretical interpretation of the spectra of such complex atoms and ions. It was in 1957 that Satten[6] for the first time analysed the spectrum of Nd^{3+} in $Nd(BrO_3)_3.9H_2O$ using LS-coupling scheme. Latter studies[7,8] suggested the suitability of the intermediate coupling scheme for the treatment of low lying levels in the crystal spectra of almost all the lanthanide compounds. Since then considerable progress has been made in the interpretation of the spectra of lanthanides[9]. The spectra of

rare earths consist of well separated groups of sharp lines. Each group corresponds to the Stark structure of a given free ion level. The relative positions of the free ion levels do not change much from one host material to another. This implies that we are essentially dealing with localized electrons. The observed spectra of triply ionized rare earths originate from transitions among the states of the $4f^N$ configuration. The $4f^N$ electrons are shielded[10] by the $5s^2 5p^6$ electrons, as a result they interact only weakly with their environment.

The study of the spectroscopic properties of rare earth ions provides an excellent method in probing the crystalline fields. Moreover, the rare earth ions due to their high quantum conversion efficiency and fast relaxing states above the ground level are extremely useful in the development of solid-state lasers[11]. A study of the spectral properties of rare earths, keeping this application in view, becomes still more important.

Trivalent neodymium possesses most of the characteristics needed for an efficient laser action. Its fluorescence in crystals most suited for lasers (e.g. $CaWO_4$, YAG, etc.) lies in the infrared. The strongest fluorescence corresponds to the transition $4F_{3/2} \longrightarrow 4I_{11/2}$ around 1060 nm. Most of the Nd^{3+} based lasers operate around this frequency. Though the visible fluorescence[12,13] has been observed in $NdCl_3$ $NdBr_3$ crystals but these being soft crystals, are unsuitable

for lasers. Trivalent praseodymium should be equally interesting with the added possibility of lasing action in the visible region[14-17]. Recently Esterowitz and coworkers[18,19] have analysed the absorption and fluorescence spectra of $LiYF_4:Pr^{3+}$ and reported laser action[20] at 479 nm at room temperature.

In the present work detailed studies of fluorescence and absorption spectra of $PbMoO_4$ and $PbWO_4$ single crystals doped with Pr^{3+} and Nd^{3+} (grown by Czochralski technique) have been undertaken. Polarized fluorescence and absorption spectra of these systems are obtained in the visible and near IR region. The results are analysed within the framework of the crystal field theory. Apart from the fluorescence and absorption spectra, the Raman spectra of the host materials are also recorded using Ar^+ ion laser for excitation. The results of Raman measurements have been compared with the earlier works[21-22] on these and similar crystals. These spectra have been helpful in sorting out the interferring Raman lines from the fluorescence spectrum.

Since the rare earth ions interact weakly with the crystalline environment, the natural course in the quantitative interpretation of their spectra is to treat the crystal field as a small perturbation to the free-ion Hamiltonian.

In the theoretical treatment of the spectra of free rare earth ions, the noncentral interactions like the electrostatic, the spin-orbit and the configuration interactions are treated as perturbations to the central field Hamiltonian. The matrix elements are calculated in the intermediate coupling scheme. Here the basis states $|UWSLJ\rangle$ involve S, L, J as the composite spin, orbital and total angular momenta and U and W are additional quantum numbers introduced by Racah for a complete classification of the states. The angular parts of the matrix elements are evaluated exactly but the radial parts are treated as adjustable parameters in an effort to match experimental and theoretical results.

Each free ion level is (2J+1) fold degenerate. The crystal field with less than spherical symmetry removes this degeneracy partially or completely. Matrix elements of the crystal field interactions are calculated using the intermediate coupling wavefunctions as zero order functions. The radial parts are again treated as adjustable parameters. Following this approach free-ion and crystal field parameters and wavefunctions for $PbMoO_4$ and $PbWO_4$ doped with Pr^{3+} have been obtained.

REFERENCES

1. J. Becquerel, Radium $\underline{4}$, 328 (1907).

2. H. Bethe, Ann. Physik $\underline{3}$, 133 (1929).

3. W. Prandtl and K. Sheiner, Z. Anorg. Alge Chem. $\underline{220}$, 107 (1934).

4. G. Racah, Phys. Rev. $\underline{62}$, 438 (1942).

5. K.W.H. Stevens, Proc. Phys. Soc. (London), $\underline{A65}$, 209 (1952).

6. R.A. Satten, J. Chem. Phys. $\underline{21}$, 637 (1953).

7. G.H. Dieke and H.M. Crosswhite, Appl. Opt., 2, 675 (1963).

8. G.H. Dieke, Advances in Quantum Electronics (Columbia Univ. Press, New York, 1961).

9. G.H. Dieke, Spectra and Energy Levels of Rare Earth Ions in Crystals (John Willey and Sons, New York, 1968).

10. M.G. Mayer, Phys. Rev. $\underline{60}$, 184 (1941).

11. M.J. Weber, Methods of Experimental Physics, Vol. 15, Pt A, Quantum Electronics, Ed. C.L. Tang (Academic Press, 1979, p. 167).

12. G.H. Carlson and G.H. Dieke, J. Chem. Physics, $\underline{29}$, 229 (1958).

13. G.H. Carlson and G.H. Dieke, J. Chem. Physics, $\underline{34}$, 1602 (1961).

14. A. Yariv, S.P.S. Porto and K. Nassau, J. Appl. Phys. $\underline{33}$, 2519 (1962).

15. R. Solom n and L. Meuller, Appl. Phys. Letters $\underline{3}$, 133 (1963).

16. V.L. Bakumenko, et al, Opt. and Spect. $\underline{19}$, 68 (1965).

17. K.R. German, A. Keil and H. Guggenheim, Phys. Rev. B, $\underline{11}$, 2436 (1975).

18. L. Esterowitz, F.J. Bartoli and R.E. Allen, Journal of Luminescence 21, 1 (1979).

19. L. Esterowitz, F.J. Bartoli, R.E. Allen, D.E. Wortman, C.A. Morrison and R.P. Leavitt, Phys. Rev. B, 19, 6442 (1979).

20. L. Esterowitz, R. Allen, M. Kruer, F. Bartoli, L.S. Gold berg, H.P. Jenssen, A. Linz, V.O. Nicolai, J. Appl. Phys. 48, 650 (1979).

21. R.K. Khanna, W.S. Brower, B.R. Guscott and E.R. Lippincott, Jl. of Research of the National Bureau of Standards – A. Physics and Chemistry, 72A, 81 (1968).

22. S.P.S. Porto and J.F. Scott, Phys. Rev. 157, 716 (1967).

CHAPTER II

EXPERIMENTAL DETAILS

1. GENERAL

Several scheelite crystals[1-4] (e.g. $CaWO_4$, $PbMoO_4$, $LiYF_4$ etc.) have proved to be good host materials for their applications in lasers mainly for the following reasons. These are hard and stable materials. Sufficiently large size crystals needed for lasers can be easily grown. These crystals can be doped with divalent and trivalent impurity ions. Since the scheelites are free from rare earth impurities, they have an advantage over other host materials for the study of rare earth ions. Further, $PbMoO_4$ finds use in optoacoustic devices for modulating and deflecting light beams.

In the present work absorption, fluorescence and Raman scattering studies of $PbXO_4$ (where X = Mo or W)[+] single crystals doped with rare earth ions are taken. $PbXO_4$ crystals are transparent between 2000 cm^{-1} - 25000 cm^{-1}. Following sections outline its structure and doping by rare earth ions.

[+]Henceforth we will use this notation to refer to $PbMoO_4$ and $PbWO_4$.

2. CRYSTAL STRUCTURE

Lead molybdate and lead tungstate belong to the tetragonal system of crystals and possess the scheelite type structure with space group $C_{4h}^{6}-I_{4\ 1}/a$. Figure II-1 shows the position of atoms in the unit cell. For simplicity only Pb and X ions are shown. Unit cell contains four Pb, four X and sixteen oxygen atoms occupying the following positions:

Pb : 0 1/4 5/8; 0 3/4 3/4 ; 1/2 3/4 1/8 ; 1/2 1/4 1/8

X : 0 1/4 1/8 ; 0 3/4 7/8 ; 1/2 3/4 5/8 ; 1/2 1/4 3/8

O : (0 0 0, 1/2 1/2 1/2) $\pm$ (x y z, $\bar{x}$ 1/2 -y z,
    3/4-y 1/4+x 1/4+z, 1/4+y 1/4-x 1/4+z)

Crystallographic information for some scheelite crystals is summarized in Table 1(a). Table 1(b) gives interatomic distances and angles for $PbMoO_4$ which will be very nearly the same for $PbWO_4$ crystals. Main features of the structure are discussed below. Each X ion is surrounded by 4 oxygen ions forming a slightly distorted tetrahedron (cf. Fig. II-2). Thus considering the nearest neighbours only, X ion has nearly a cubic environment. The distance ($\sim$ 1.772 Å) between X and oxygen ions is less than the sum ($\sim$ 1.992 Å) of Pauling ionic radii (cf. Table II-2) of X and O-ions indicating a covalent bonding within the XO_4

O — Pb site

o — X site
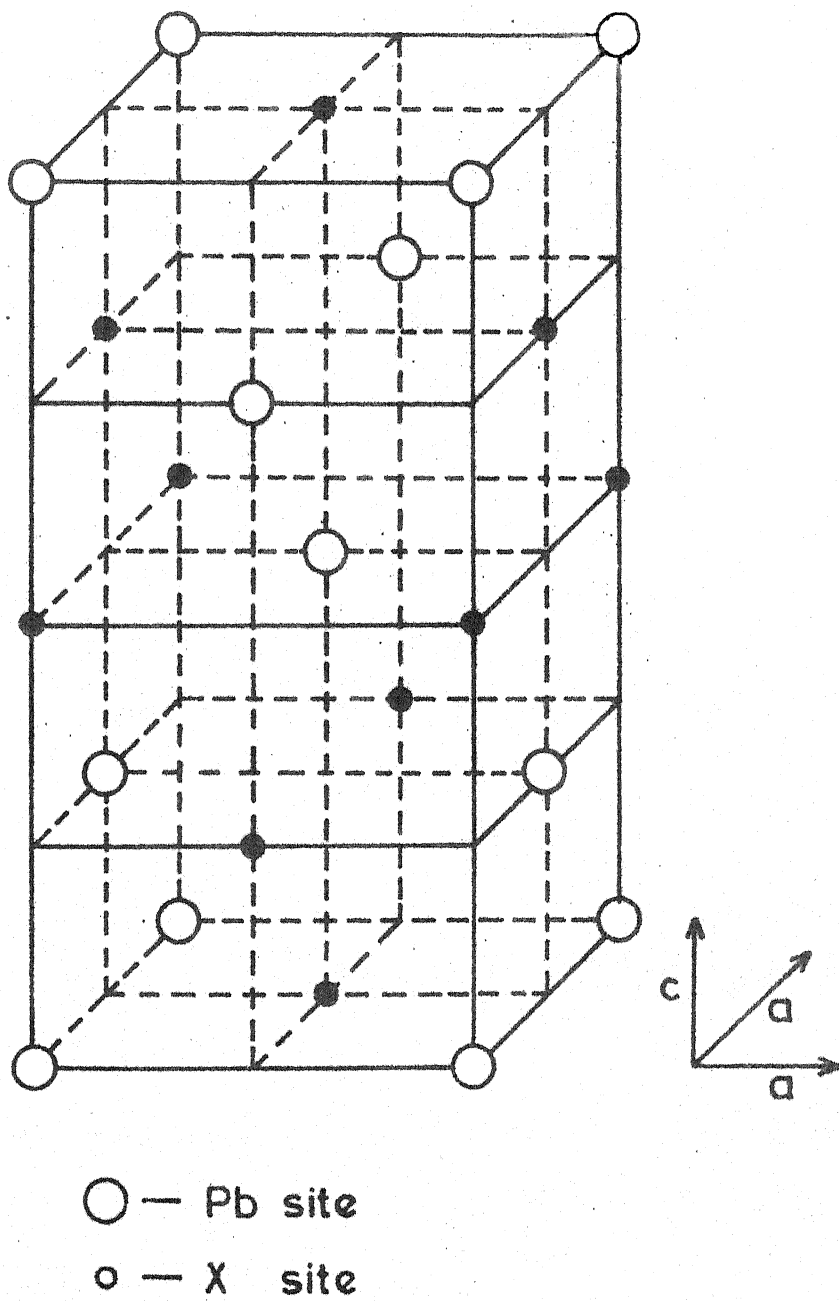
Fig.II.1   Unit cell of PbMoO$_4$ single crystal
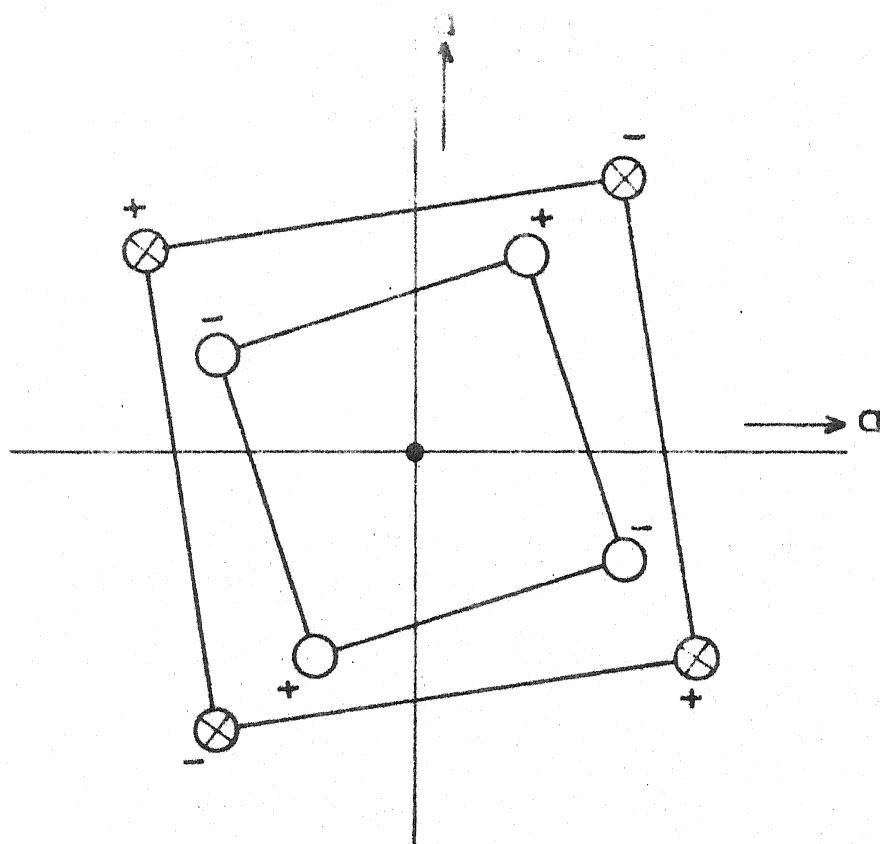
○ — Oxygen ions (nearest neighbour)

⊗ — Oxygen ions (next nearest neighbour)

● — Pb ions

+ ···· Ions above the horizontal plane

− ···· Ions below the horizontal plane.

Fig. II.2 Oxygen enviornment of Pb^{2+} ions.

TABLE II-1(a)

Crystallographic Data for Some Scheelites[*]

S.N.	Crystal	Parameters				
		a(Å)	c(Å)	x/a	y/a	z/c
1	$PbMoO_4$	5.41	12.08	0.25	0.13	0.075
2	$PbWO_4$	5.44	12.01	0.25	0.13	0.075
3	$CaMoO_4$	5.23	11.44	0.25	0.15	0.075
4	$CaWO_4$	5.24	11.38	0.25	0.15	0.075
5	$SrMoO_4$	5.35	11.94	0.25	0.14	0.075
6	$SrWO_4$	5.40	11.90	0.25	0.14	0.075

x, y and z here are with respect to X ion at (0,0,0)

TABLE II-1(b)

Interatomic Distances and Angles for $PbMoO_4$[**]

Distances (Å)		Angles	
Mo—O	Pb—O	O—Mo—O	O—Pb—O
1.772	2.610 2.630	$112°$–50'	$76°$–43' $127°$–57'
		$107°$–40'	$98°$–0' $130°$–12'

* Data taken from Ref. 6

** Data taken from Ref. 7

TABLE II -2

Pauling Ionic Radii

Ion	Radii ($\overset{\circ}{A}$)
Pb^{2+}	1.26
Mo^{6+}	0.65
W^{6+}	0.62
O^{2-}	1.32
Nd^{3+}	0.99
Pr^{3+}	1.00

tetrahedron. Each Pb ion is surrounded by 8 oxygen ions each belonging to 8 different XO_4 units. Four of the oxygen ions are at a distance of 2.61 $\overset{O}{A}$ from the Pb ion and four others lie at a slightly larger distance of 2.630 $\overset{O}{A}$. The sum of Pauling ionic radii for Pb and oxygen ions corrected for a coordination number 8 is ~ 2.70 $\overset{O}{A}$ which is comparable to Pb-O distance. These oxygen atoms are at the corners of two interpenetrating tetrahedra forming a somewhat distorted cube as shown in Fig. II-2. The nature of these distortions is such that the site symmetry at both X and Pb sites is S_4. The characteristic element of this point group is a fourfold rotary reflection axis. It can be seen from Fig. II-1 that four nearest (out of eight) X ions surrounding a Pb ion lie on the corners of a square with X-Pb distance of ~ 3.84 $\overset{O}{A}$ and the next four at the corners of a tetrahedron with Pb-X distance of 4.05 $\overset{O}{A}$. This constitutes a D_{2d} symmetry at Pb site. However, this is reduced to S_4 due to the presence of oxygen ions. Similarly each X ion is in turn surrounded by 8 lead ions.

3. RARE EARTH ION DOPING IN $PbXO_4$ CRYSTALS

Like other crystals having scheelite structure $PbXO_4$ crystals can be readily doped with rare earth ions. Excluding the possibility of interstitial substitution in view of the compact structure of these crystals, rare earth ions

will substitute for Pb^{2+} or X^{6+} ions. If the rare earth ions were to replace X^{6+}, the resulting optical spectra would be very nearly unpolarized due to approximately cubic environment of the X-ion. The fact that the observed spectra are highly polarized indicates that the rare earth ions do not replace X^{6+} ions. Moreover, the spectrum of an impurity ion substituting for X^{6+} is expected to show effects of its covalent bonding to the surrounding oxygen ions. The observed spectra of rare earth impurity ions in these hosts consist of well separated groups of sharp lines - thus retaining the free ion structure of rare earths. This suggests that the bonding between the impurity ion and its surrounding ions is predominantly ionic. One may therefore, conclude that the rare earth impurity ions substitute for Pb^{2+} and not for X^6 ions in these hosts. Substitution of Pb^{2+} by a rare earth impurity ion is favoured due to better matching of their ionic radii (cf. Table II-2) and also because of a smaller charge imbalance left by the substitution. Because of the heterovalent nature of the substitution, it is necessary to compensate the surplus charge which would otherwise result in the creation of vacancies in the lattice. Such defects contribute to some extra lines in the spectra of these crystals[8,9] which usually disappear upon charge compensation. Charge compensation can be achieved through any of the following ways.[10]

(a) by creating the vacancies at the cation sites

(b) by lowering the valence of X^{6+} to X^{5+}

(c) by the pairing of impurity ions

(d) by the replacement of X^{6+} by pentavalent ions

(e) by the introduction of Na^+ ions in the lattice, replacing Pb^{2+} ions

4. SAMPLE PREPARATION

Neodymium doped samples of $PbMoO_4$ and $PbWO_4$ were prepared from large size single crystals[+] (typical dia ~1 cm and length 3.0 cms) of good optical quality. These crystals were grown from a mixture of analytic grade PbO and XO_3[*] (where X = Mo or W) using Czochralski technique. An excess of 0.05% by weight of XO_3 was added to the mixture in order to compensate for losses due to its fast evaporation. Neodymium doping in these crystals was achieved by adding Nd_2O_3 (99.9% pure from Apache chemicals and 99.999% pure from Koch-light laboratory, England) to the above mentioned mixture. Charge compensation was accomplished by adding $NaXO_4 \cdot 2H_2O$. The Nd concentration in the melt varied from 0.1 to 0.4 atomic percent whereas Na concentration in the melt ranged from one to five times the concentration of Nd. A chemical analysis of the

[+] These crystals were grown by Dr. I.S. Minhas[11]

[*] Chemicals were obtained from Fischer Scientific Co., New Jersey, U.S.A.

crystals grown with 0.1% Nd in the melt puts the Nd concen-
tration at 180 ppm. These crystals have a tendency to grow
along a direction closely aligned with one of the a-axis.
As the thermal expansion along c-axis is much larger than
the expansion along a-axis and thermal gradient along ver-
tical direction is much larger than the transverse direc-
tion, less strains would result in the crystals growing
along one of the a-axis. Further, one can usually notice
two small flats (180° - apart) on the crystal surface
which are normal to the c-axis. These two facts greatly
simplify the process of crystal orientation.

5. SAMPLE ORIENTATION AND POLISHING

For ascertaining the orientation of the crystal
by X-ray back reflection laue method, it was glued to a
goniometer head using paraffin wax. Oriented crystal was
then cut by a string saw and polished on plate glass using
water solution of different abrasives. Polishing was ini-
tiated with relatively rough abrasive (9μ - 3μ grain size
Alumina powder). Alumina powders of 1μ and 0.3μ grain
size were used at the final stage of polishing. A silk
cloth was placed on top of the plate glass to avoid scrat-
ches on the optical surfaces of the sample. Typical dimen-
sions of a polished sample are ∼ 6 mm x 6 mm x 10 mm. A
polarzing microscope was used for the confirmation of the
orientation of a finished sample.

6. EXPERIMENTAL SET UP FOR SPECTROSCOPIC MEASUREMENTS

The low temperature absorption spectrum provides a direct map of energy levels lying above the ground state and fluorescence spectrum maps low lying levels relative to the excited states. Experimental arrangements for fluorescence, Raman and absorption measurements were built around the same monochromator, cryogenics and the electronic detection system. Before we describe the experimental arrangements for different measurements, a description of these common elements is in order.

A. Spectral detection

The core of our measuring set up is a Carl-Zeiss grating double monochromator GDM 1000. Its spectral range (from 7500 cm^{-1} to 17500 cm^{-1} in first order and from 15000 cm^{-1} to 35000 cm^{-1}) in second order and high resolving power (< 0.5 cm^{-1}) at high intensities makes it specially suited for spectral detection even at low light levels. GDM 1000 incorporates one 25 Hz chopper for making measurements with alternating light. For wavenumber drive, add on Carl-Zeiss G1B1 recorder was used. The wavenumber read out of the instrument was calibrated using several wavelengths of Ne discharge. Some details of the GDM 1000 and a calibration chart are given in Appendix I.

B. Cryogenics

For measurements at liq. N_2 temperature a glass dewar was fabricated. This dewar employed a cold finger for sample cooling. The cryostat and sample holder are shown in Fig. II-3. Sample holder was made from a copper piece and brazed to the cold finger to provide better thermal conduction. A copper heat shield with five apertures (one in the bottom and four on the sides) reduces the absorption of radiation from the surrounding. The dewar was fitted with 4 windows of Corning's 7059 glass (soda free glass) plates and two thermocouples for measuring the temperature of the sample.

C. Detection electronics

The spectrally dispersed light falls upon a photomultiplier tube M12FC51 with S-20 cathode or on a PbS detector[+] (installed for near IR measurements). Figure II-4 shows the biasing circuit for PbS detector. The detector output is synchronously detected by the lock-in technique using PARC Model HR-8 lock-in amplifier. In lock-in technique the signal is passed through the time internal domain[12] to improve signal to noise ratio. For this a reference time signal is required. The specifics of the lock-in-technique are as follows.

If the light falling on the detector is chopped at some frequency, the output will also pulse periodically.

[+]Mfd. by Santa Barbara Research Centre, USA.

Thermocouple leads

Glass to metal seal

Kovar metal tube

Sample holder

Copper heat shield

To pump

Window

Fig.II.3   Cryostate and sample holder.

Fig. II.4 Biasing circuit for PbS detector.

The waveform of this output signal is characterized by
its amplitude (dependent upon the strength of the light
pulse), frequency (set by the chopper), phase (on-off time
with respect to the reference) and the duty cycle (on time
divided by the sum of on-off times. This depends upon the
size and number of chopper slits). The waveform property
of interest in our measurement is amplitude. White noise
is a signal random in amplitude, frequency and phase. One
can abstract the light signal, which is periodic, from the
random noise by appropriate electronics.

Lock-in-amplifier selects a band of frequencies from
a signal spectrum applied to its input and converts the
information there into an equivalent bandwidth about d-c.
The output of the detector is first amplified by a high
quality tuned amplifier, which selectively amplifies all
signals (including noise) of the same frequency as that
of the chopper. This selectively amplified signal is then
passed to a phase-sensitive demodulator in which the input
signal is mixed with a synchronous reference signal to pro-
vide sum and difference frequencies. Because the difference
frequency produced by that component of input signal at the
reference frequency and synchronous with it is zero, the
fundamental is converted to a d-c level on which the other
frequencies (noise) are superimposed. A low pass filter
at the output of the mixer rejects the high frequency

components corresponding to the sum frequency and passes the difference frequency which lies within its passband. By making the bandwidth of the filter narrow, the effect of input noise on the output can be greatly reduced. The output becomes simply a d-c level proportional to the fundamental component of the input signal, the noise averaging to zero. The output signal then is due almost exclusively to the light radiated by the sample cell (amplitude). In the following subsections we will discuss the experimental arrangements specific to the particular spectroscopy.

6.1 Absorption Measurement Set up

The experimental arrangement for the absorption measurements is shown in Fig. II-5. Various details are given as below.

6.1.1 Light source: Light from a white light source is focussed into the sample cell parallel to the direction of observation and perpendicular to the c-axis of the crystal. A tungsten halogen lamp of 1000 watts with linear filament (Mfd. by Tungsram, W. Germany) was used as a light source for visible and near IR region. Colour temperature for these lamps is 2800 K. For continuous operation over long periods of time, efficient cooling of the lamp is necessary. A water cooling arrangement as shown in Fig. II-6 was made.

S — Light source
A — Aperture
L_1, L_2 — Sample illuminator
L_3, L_4 — Entrance slit illuminator ($f/5.5$)
P_1 — Polarizer
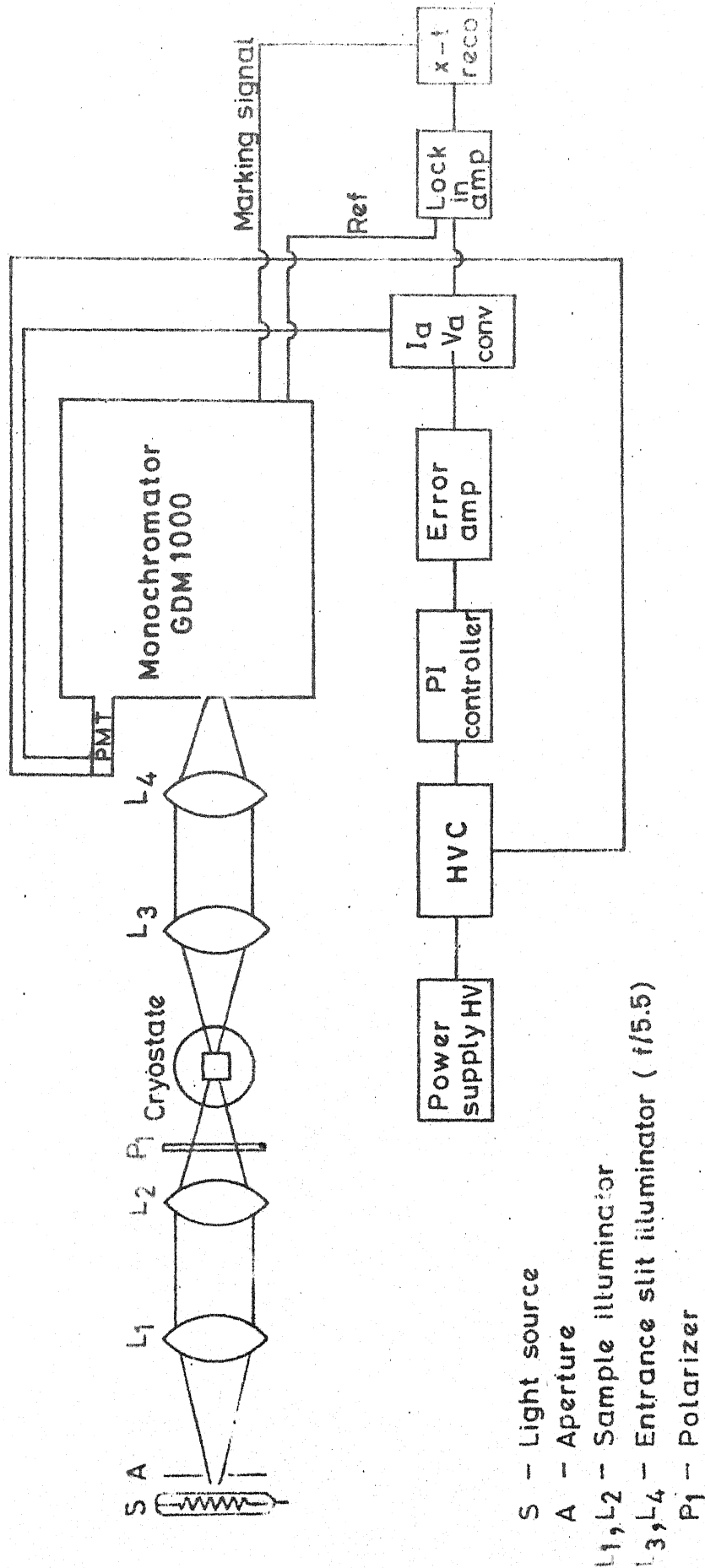
Fig. II.5   Absorption   measurement set-up.

Water outlet

Clamping nut

Strip spring

Teflon washers

Space

Halogen lamp

Teflon washer

Cooling jacket

Lamp housing

Spacer

Teflon washers

Strip spring

Clamping nut
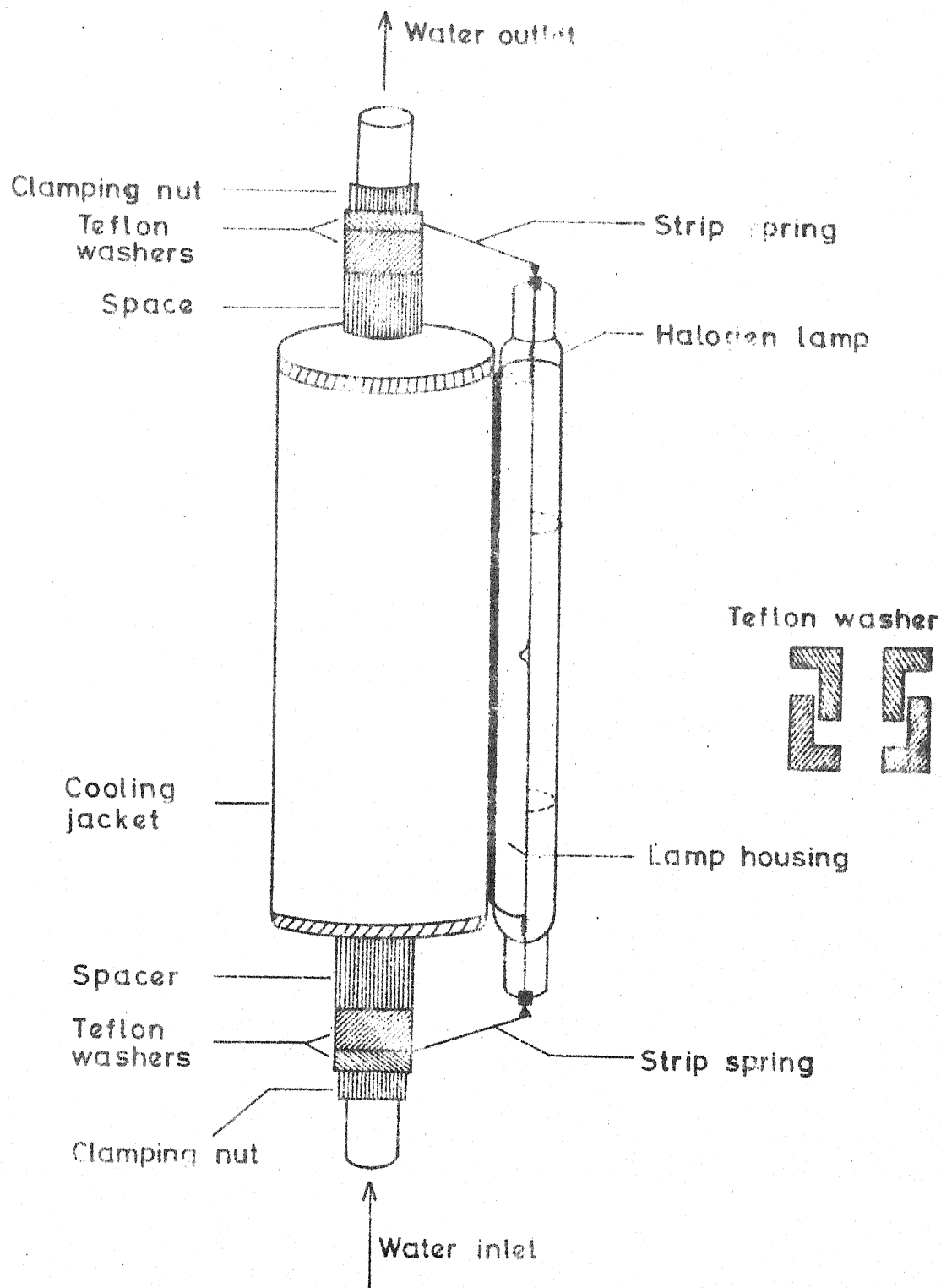
Water inlet

Fig. II.6   Cooling jacket

A copper tube of 1 cm dia having a 8 mm wide aper-
ture along its entire length meant for housing the lamp
was brazed back to back with another 2.5 cm diameter copper
tube plugged at both ends with water inlet/outlet connections.
Electrical contacts to the ends of the lamp are provided
through two metallic strip springs clamped to the inlet/
outlet connections. These strips were insulated from the
rest of the assembly by two pairs of teflon washers. A
polaroid sheet analyzer is used for selecting the polariza-
tion of the light.

6.1.2 <u>High voltage controller</u>: In a single beam spectro-
meter used for absorption measurements, large variations in
the response occur due to emission characteristics of lamp
and detection sensitivity of PMT. To remove base-line varia-
tion, a signal controller based on the one described by
Obink et al[13] was fabricated with some modifications. The
underlying principle of the device and its functioning is
described below.

The output from the PMT for modulated light input
is composed of a d-c and an alternating current

$$I_{dc} = G \phi_0 \, e^{-D} \qquad\qquad (2.1)$$

and

$$I_{ac} = G \phi_0 \, e^{-D} (\, \Delta D J_1 (\delta_m) \mathrm{Sin} \, \omega_0 t) \qquad (2.2)$$

where

G is the gain of the PMT,

ϕ_0 is the luminous flux,

D is the optical density of the sample,

$J_1(\xi_m)$ is the Bessel function of first degree,

ξ_m is the modulation amplitude and

ω_0 is the modulation frequency.

d-c current can be kept constant by varying the flux ϕ_0 or by varying the PMT gain G. Flux ϕ_0 can be varied by changing the dimensions of the slit of the monochromator, the so called slit servo method which has been used extensively in the commercial instruments[14]. In what follows we describe the circuit of a high voltage controller for varying the gain of PMT. It uses the varying d-c signal for correcting the varying base-line.

Figure II-5 shows schematically the measuring set up including the voltage control device. This device (cf. Fig. II-7) is merely a closed loop system with proportional and integrative action in the feedback-loop. Anode current of the photomultiplier tube is converted to an equivalent voltage by I_a-V_a converter. This voltage is then compared with a set point voltage by an error amplifier (with high common mode rejection). The error signal V_e controls the low voltage section of the circuit. This section consists of a PI controller whose output V_c determines the gain of

the PMT, an error amplifier to compare V_c to a set point voltage and voltage controlled current source driving the L.E.D. of the optoisolator to activate the high voltage section of the controller. Optoisolator provides the galvanic isolation between low voltage and high voltage sections. The emitter current of the phototransistor of the optoisolator has a linear relationship with the current in L.E.D., thus assuring a stable current behaviour.

The emitter of phototransistor is coupled to the base of a high voltage transistor (BU 205) having the dynode resistance chain in series with its collector. Obink et al[13] used this transistor in parallel with dynode chain. The series connection has some advantages over this configuration which we will point out later. High voltage transistor changes current through dynode chain in accordance with V_c just like a voltage controlled resistance. Owing to this variation in current, voltage over the dynode chain is changed thereby adjusting the PMT amplification to keep d-c term constant. The connection of the dynode chain in series with high voltage transistor avoids the necessity of high wattage resistance in the emitter circuit of BU205 and allows much more capacity of voltage variation. Voltage variations of -100 to -1400 volts can be realized, thus accommodating correction for very wide light intensity changes. A 15 V zener diode provides an auxillary supply

for the phototransitor while 180 volts Zener is used to
maintain constant voltage drop between cathode and first
dynode of PMT. Ground loops were completely eliminated
by connecting the lock-in-amplifier just after the I_a-V_a
converter.

Base line plots with and without HVC controller
are shown in Fig. II-8. Some salient features of this
approach are summarized below.

(i) Changes in the resolution due to variation in the
slit width is eliminated.

(ii) Accessible region is determined completely by the
light source, optics and detector.

(iii) It can be used with a conventional high voltage
supply as an add on device.

6.2 Fluorescence and Raman Measurement Set up

Experimental set up for Raman and fluorescence
measurements is shown in Fig. II-9. A C.W. Ar^+ ion
laser (Carl Zeiss Model ILA 120) was used for exciting
the samples. Unlike conventional light sources lasers
emit highly concentrated beam of coherent radiation.
Greater sensitivity achieved by laser excitation makes
the detection of very weak lines which can not be
detected by excitation with the conventional incoherent
sources, also feasible. Laser beam traverses the samples
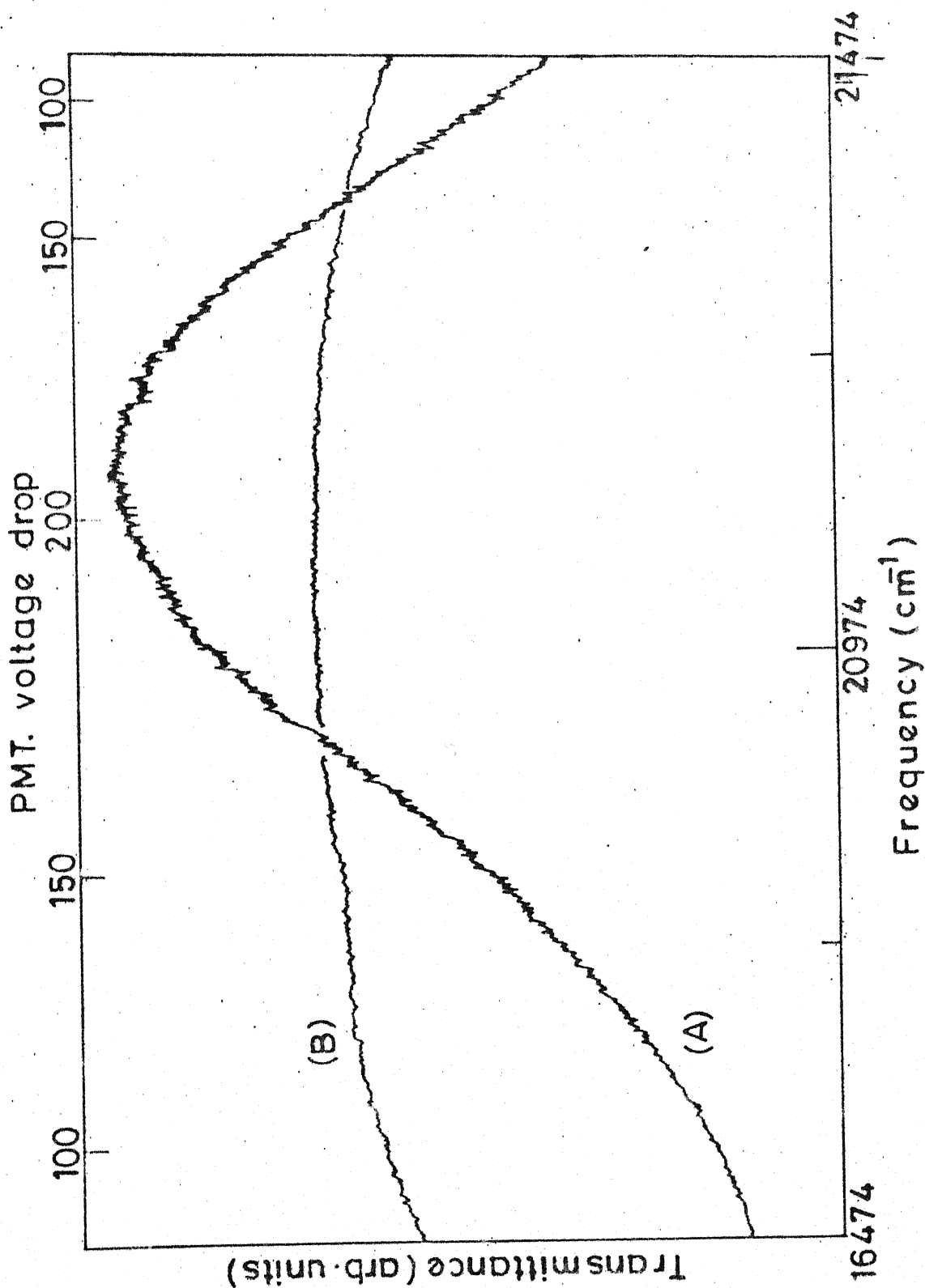
Fig. II.8   Base line for GDM 1000   (A) Without high voltage
controller (B) with high voltage controller.

Fig. II.9 Fluorescence measurement set-up.

R₁ — Polarization rotator
P₁ — Analyzer
L₃, L₄ — Entrance slit illuminator
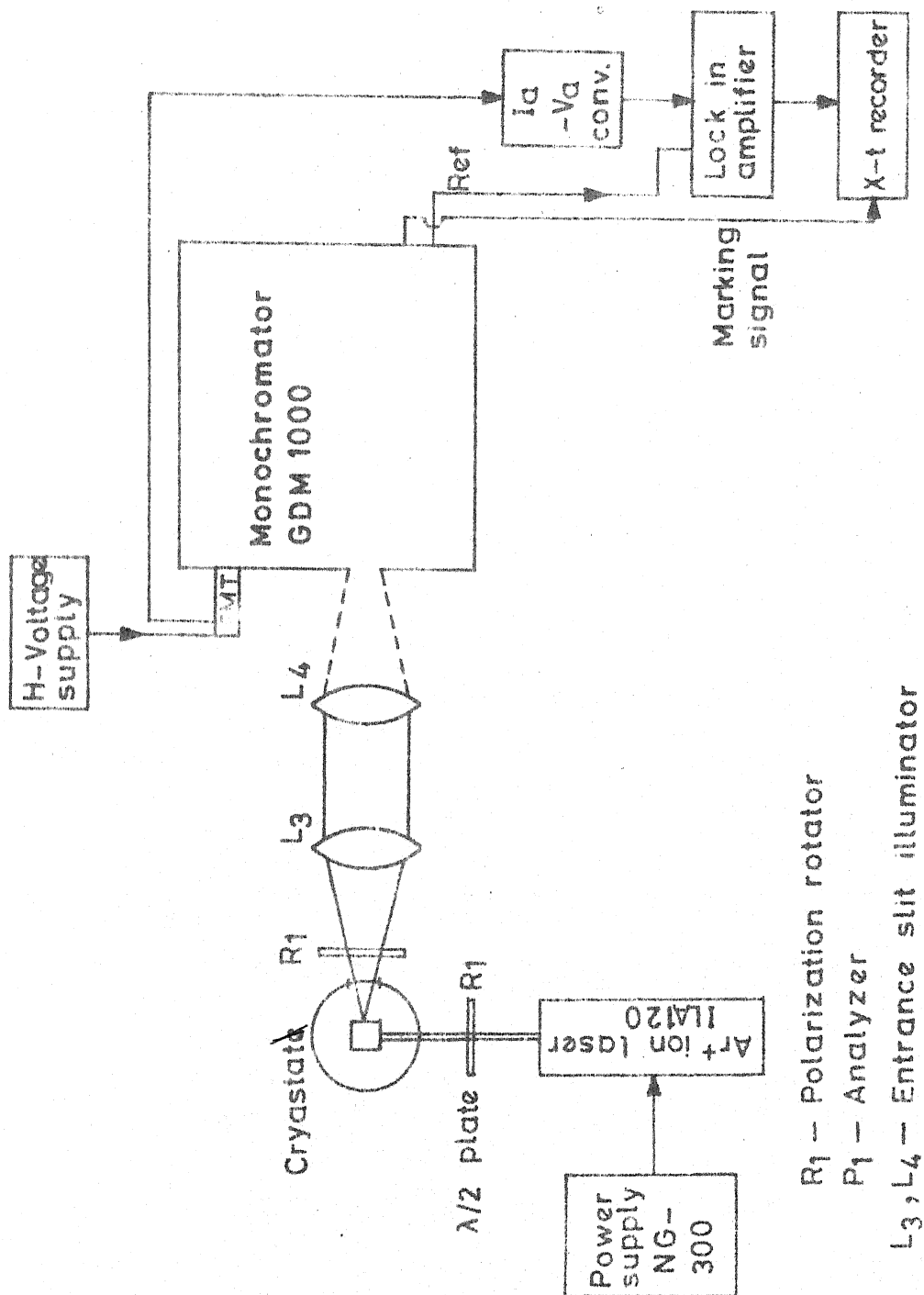
along an a-axis and perpendicular to the direction of observation. For efficient pumping of samples for fluorescence measurements and in order to select various geometries for Raman measurements, a half wave plate was used for rotating the polarization of the laser beam. A metallic reflector placed above the sample was used to reflect the laser beam back to avoid unnecessary heating of the sample-holder. A polaroid sheet was used for selecting the polarization of the resulting radiation from the sample. A set of neutral density filters was used for studying the dependence of fluorescence signal on the input power. Due to the absence of any servicing facility of the laser from the manufacturers, a detailed study of the laser circuits etc. was made to take up repairs required at various stages of this work. The Appendix II includes some notes on the troubleshooting.

7. CRYSTAL GROWTH OF RARE EARTH DOPED SAMPLES

Growth of Er^{3+} doped $PbMoO_4$ crystals by Czochralski technique was undertaken. Various details of the technique and growth conditions are outlined in ref. 11 . Initially crystals could not be grown due to some defects like wobbling of the pulling mechanism which arose due to the over-use of the system in the past. Also during these efforts, need for a furnace which would have low thermal inertia

was realized so that the temperature changes required
at various stages of crystal growth could be carried
out within a short period. A furnace using resistive
heating was fabricated to this effect. Special care
was taken to minimize the vertical temperature gradient.
A regulated d-c power-supply (75 volts, 20 Amp) was also
made to have more stable operation of the furnace. The
circuit diagram for this supply is given in Fig. II-10.
At this stage it became possible to grow the crystal
but the progress was further hampered due to nonavaila-
bility of a continuous supply of electricity for the
duration of a single run.
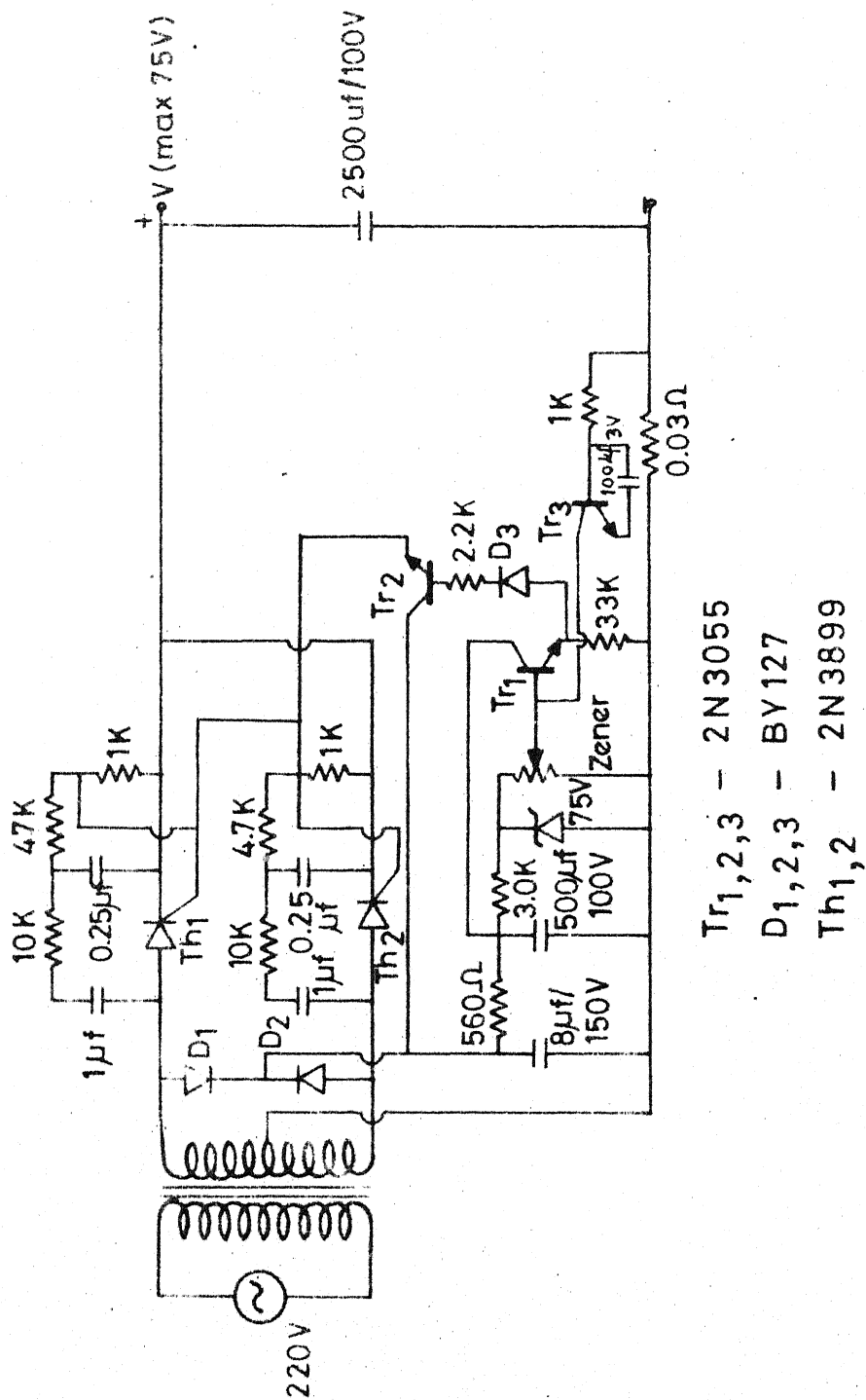
Fig. II.10 · Regulated D.C. power supply for the furnace.

8. EXPERIMENTAL DATA

Experimental data of fluorescence, absorption and
Raman measurements on $PbMoO_4$ and $PbWO_4$ samples are pre-
sented here. The wavenumber positions of spectral lines
recorded with PMT were read directly from the wavenumber
readout of the instrument. The results are reproducible
to within ± 1 cm^{-1}. However, the wavenumber position of
spectral lines recorded with IR detector could not be
taken from the wavenumber readout of the instrument due
to the noisy signal. The absolute wavenumber accuracy is
better than 1 cm^{-1}.

A. Fluorescen data

The polarized fluorescence spectra of polished
samples of doped $PbMoO_4$ and $PbWO_4$ crystals were recorded
at 90 K. The samples grown with 99.9% pure Nd_2O_3, when
exposed to 4880, 4765, 4727 and 4579 Å lines of Ar^+ ion
laser show very strong visible fluorescence. Nd^{3+} is not
known to give any visible fluorescence in these hosts.
In a later chapter we have shown that the observed
visible fluorescence is due to Pr^{3+} impurity in our
samples. Near IR fluorescence is due to Nd^{3+} and Pr^{3+}
ions. Attempts were made to measure Pr^{3+} concentration
by atomic absorption and PIXE techniques. PIXE spectra
of Nd_2O_3 (99.9% and 99.999%) pure) are reproduced in
Fig. II-11. Pr impurity concentration in these chemicals
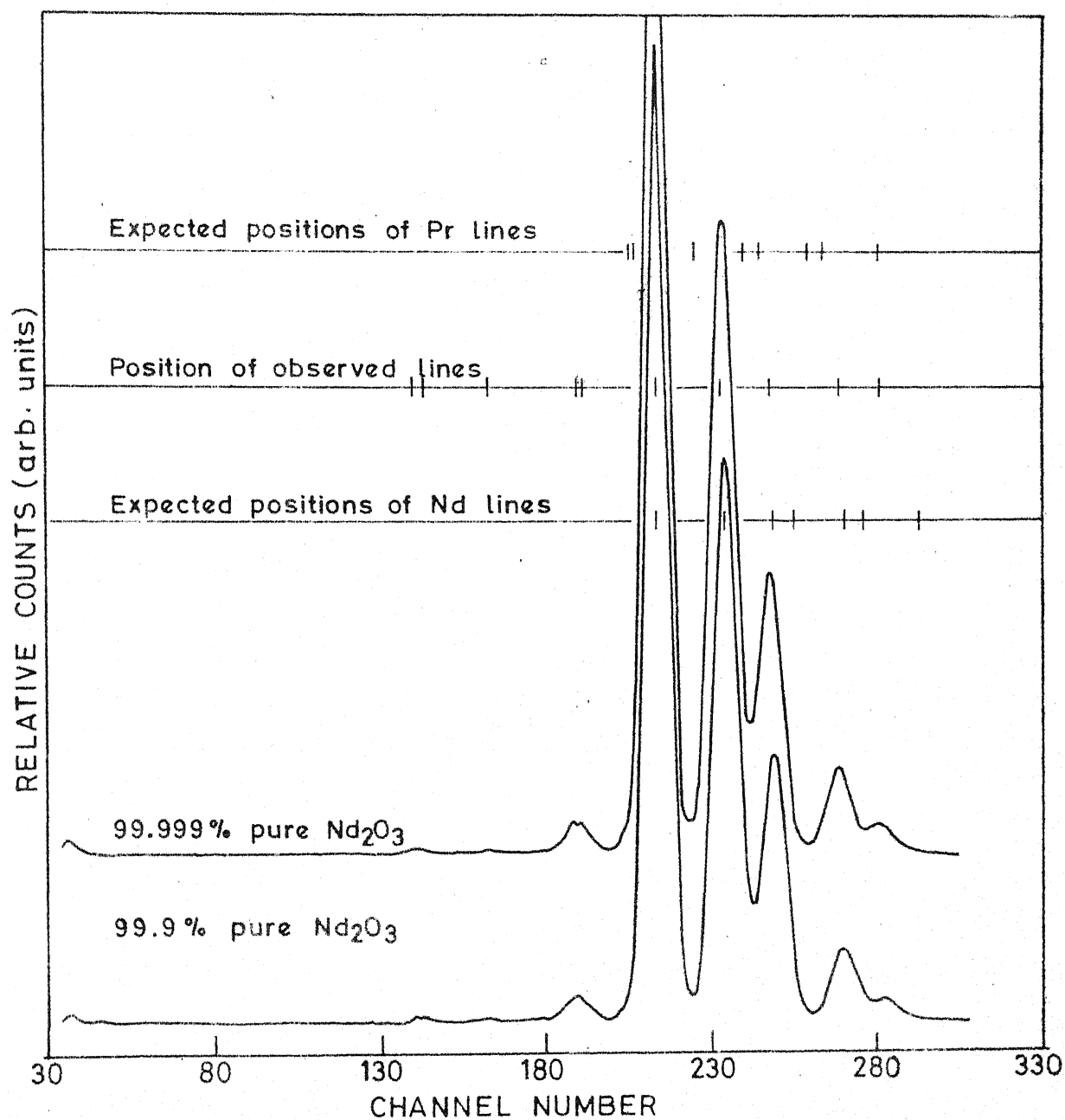
Fig. II.11   PIXE spectra of Nd_2O_3 (99.999% Koch light laboratory, England) and Nd_2O_3 (99.9% pure Apache chemicals, New Jersey, U.S.A.)

was beyond the detection limits of these methods. Assuming the 0.1% impurity in 99.9% pure Nd_2O_3 solely of Pr^{3+}, puts the Pr^{3+} concentration in samples having 180 ppm concentration of Nd^{3+} to be less than 1 ppm. Slit widths of 40 Å - 100 Å were used for recording the visible fluorescence spectra. However, due to the degraded performance of our IR detector the signal was very weak and noisy. Slit width of 3 mm size had to be used for recording near IR region fluorescence. Only the highest power blue line of Ar^+ laser (i.e. 4880 Å) was used to record the fluorescence in the near IR region to achieve a stronger signal. Most of the recorded data correspond to the monochromator scanning speed of 20 cm^{-1}/min in Ist order and 40 cm^{-1}/min in IInd order. The data tables have been arranged according to the impurity ions. Fluorescence spectra of $PbMoO_4$ samples are reproduced in Figs. II-12 - II-15. Lines marked with asterisks correspond to Nd^{3+} fluorescence. In Table II-3 the data for the fluorescence observed from $^3P_0$ level of Pr^{3+} in $PbMoO_4$ crystal is presented. Table II-4 presents the data for the fluorescence from $^1D_2$ level of Pr^{3+} in $PbMoO_4$ sample. Table II-5 contains the data for the fluorescence from $^4F_{3/2}$ level of Nd^{3+}. Fluorescence spectra for $Pr^{3+}:PbWO_4$ are reproduced in Fig. II-16 - II-17. Data for the fluorescence from $^3P_0$ level of Pr^{3+} in $PbWO_4$ crystals is presented in Table II-6 and

that corresponding to the fluorescence from $^1D_2$ level is given in Table II-7. Assignments of the lines of Pr^{3+} and Nd^{3+} are also mentioned in these Tables.

B. Absorption data

Polarized absorption spectra for $PbMoO_4$ and $PbWO_4$ samples were recorded at 90 K. The absorption spectra of $PbMoO_4$ samples recorded on the set up shown in Fig. II-5 in the region 16500 - 25000 cm^{-1} is reproduced in Fig. II-18. The lines marked with asterisks have been identified to belong to Pr^{3+} impurity and are listed in Table II-8. The absorption spectrum of $^4F_{3/2}$ state of Nd^{3+} is given in Fig. II-19 and the corresponding data is listed in Table VI-9. Slit width of 50 μm and scanning speed of 100 cm^{-1}/min were used for recording this spectrum. Absorption spectrum of doped $PbWO_4$ samples was recorded on Carry 14. Part of it is reproduced in Figs. II-20 - II-21. The absorption lines marked with the asterisks, we believe are due to Pr^{3+} impurity. These are listed in Table II-10.

C. Raman data

Raman spectra of pure host crystals (i.e. $PbMoO_4$ and $PbWO_4$) were recorded at 90 K and room temperature. In Figs. II-22 and II-23, the Stokes and antiStokes

Raman spectra for $PbMoO_4$ are reproduced and those corresponding to $PbWO_4$ are shown in Figs. II-23 – II-24. These spectra were recorded using various lines of Ar^+ ion laser (e.g. 4880, 4763, 4579 and 5145 $\overset{\circ}{A}$ etc.). Slit widths of 50-100 μm and scanning speeds of 100 cm^{-1}/min were used for these measurements. Observed Raman lines and their relative intensities in various geometries for $PbMoO_4$ and $PbWO_4$ single crystals are listed in Tables II-11 and II-12 respectively.
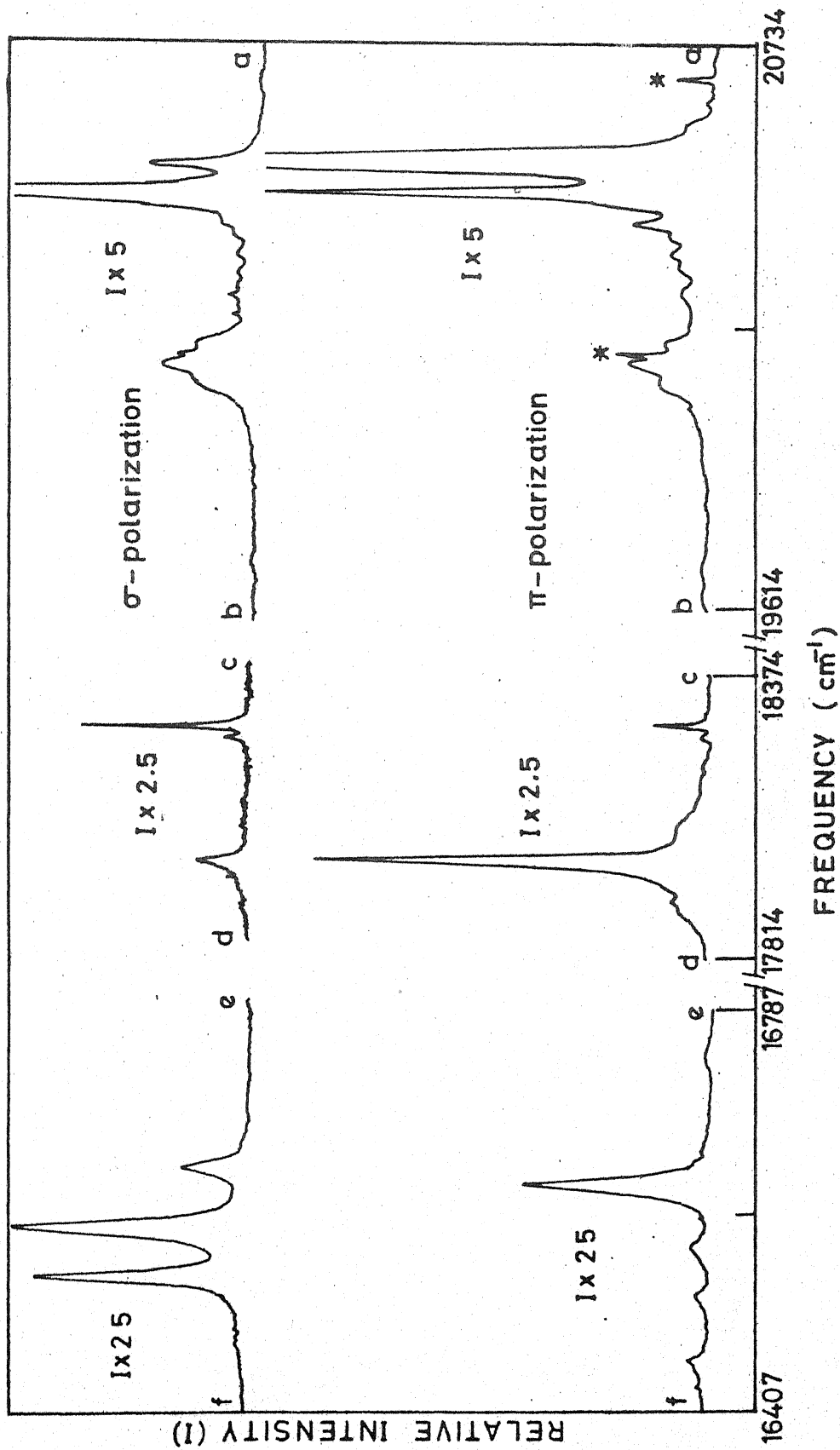
Fig.II.12 Fluorescence spectra of Pr^{3+} in $PbMoO_4$ single crystals at 90K.
* Raman lines.

40
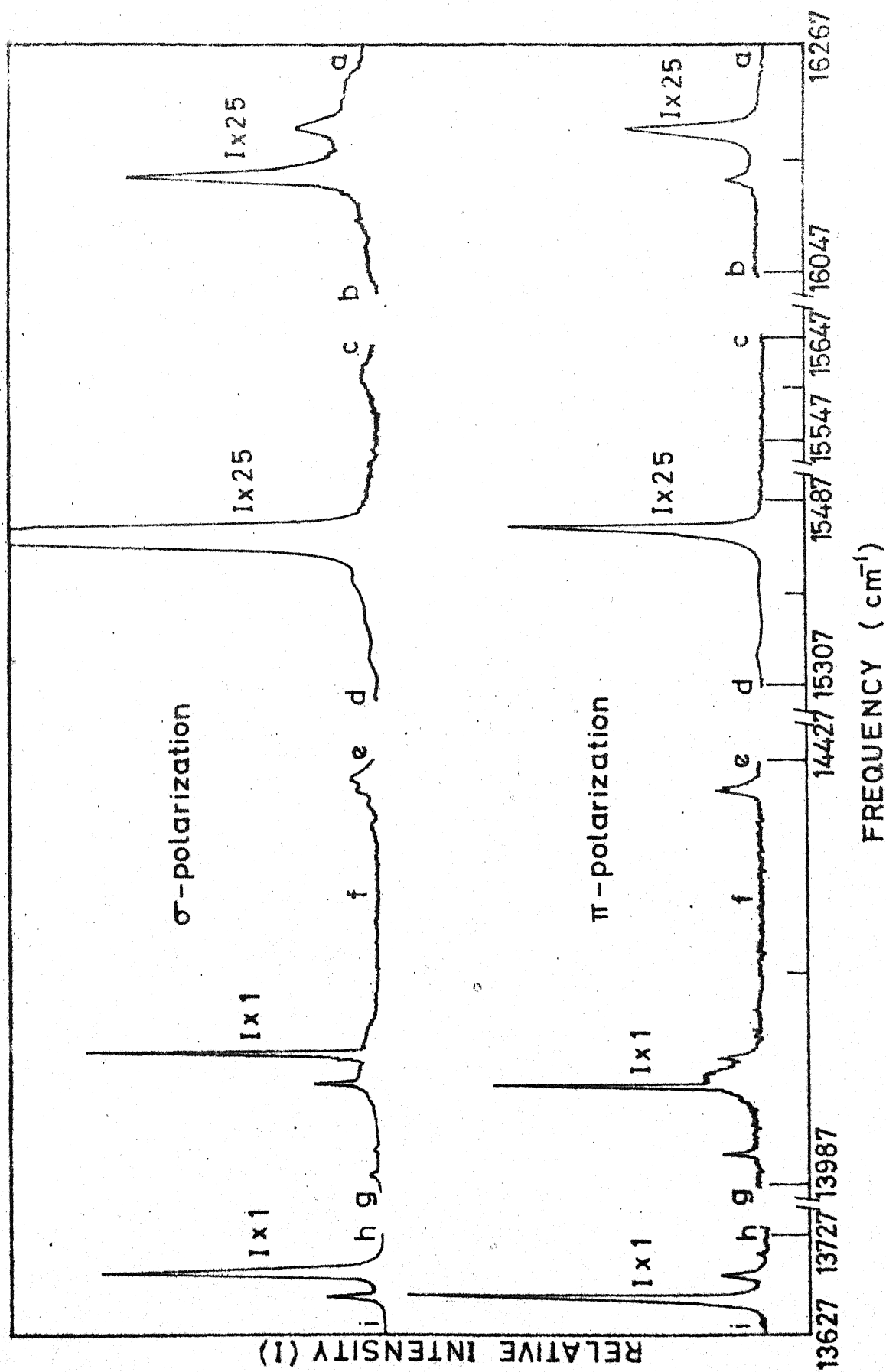
Fig. II.13 Fluorescence spectra of Pr³⁺ in PbMoO₄ single crystals at 90K.
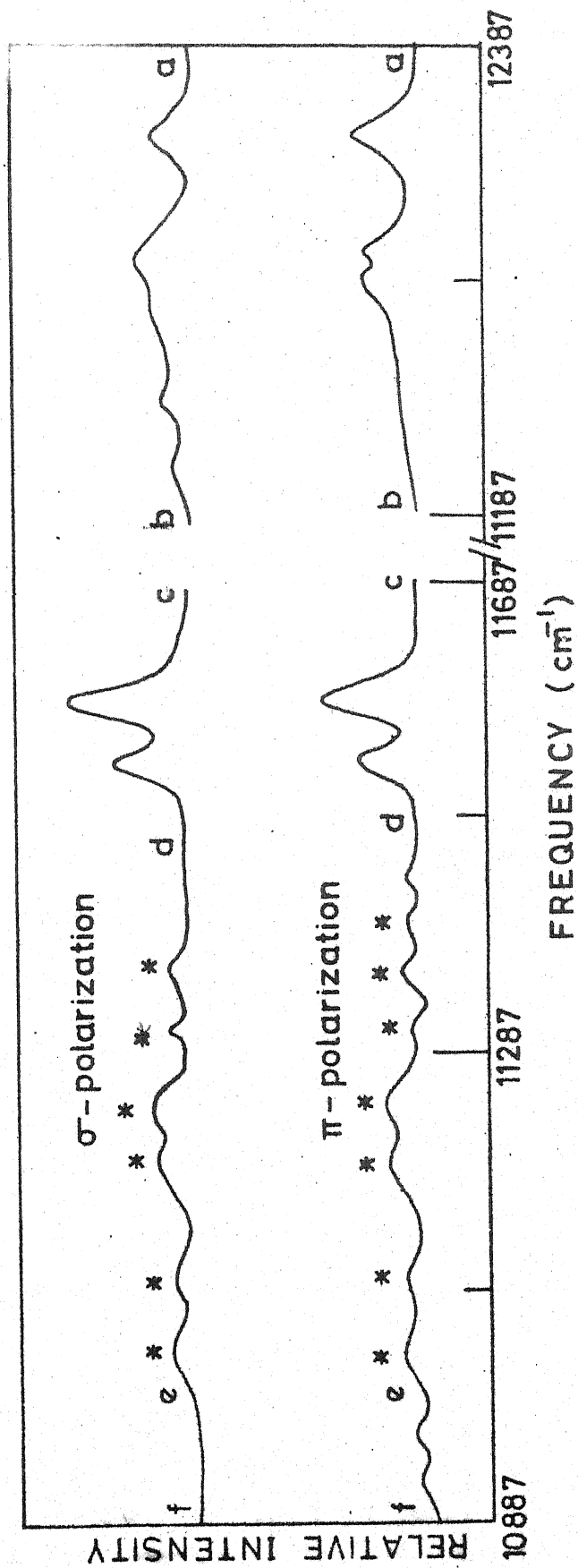
Fig.II.14 Fluorescence spectra of Pr^{3+} and Nd^{3+} in $PbMoO_4$ single crystals at 90

* – Lines correspond to the fluorescence of Nd^{3+}.
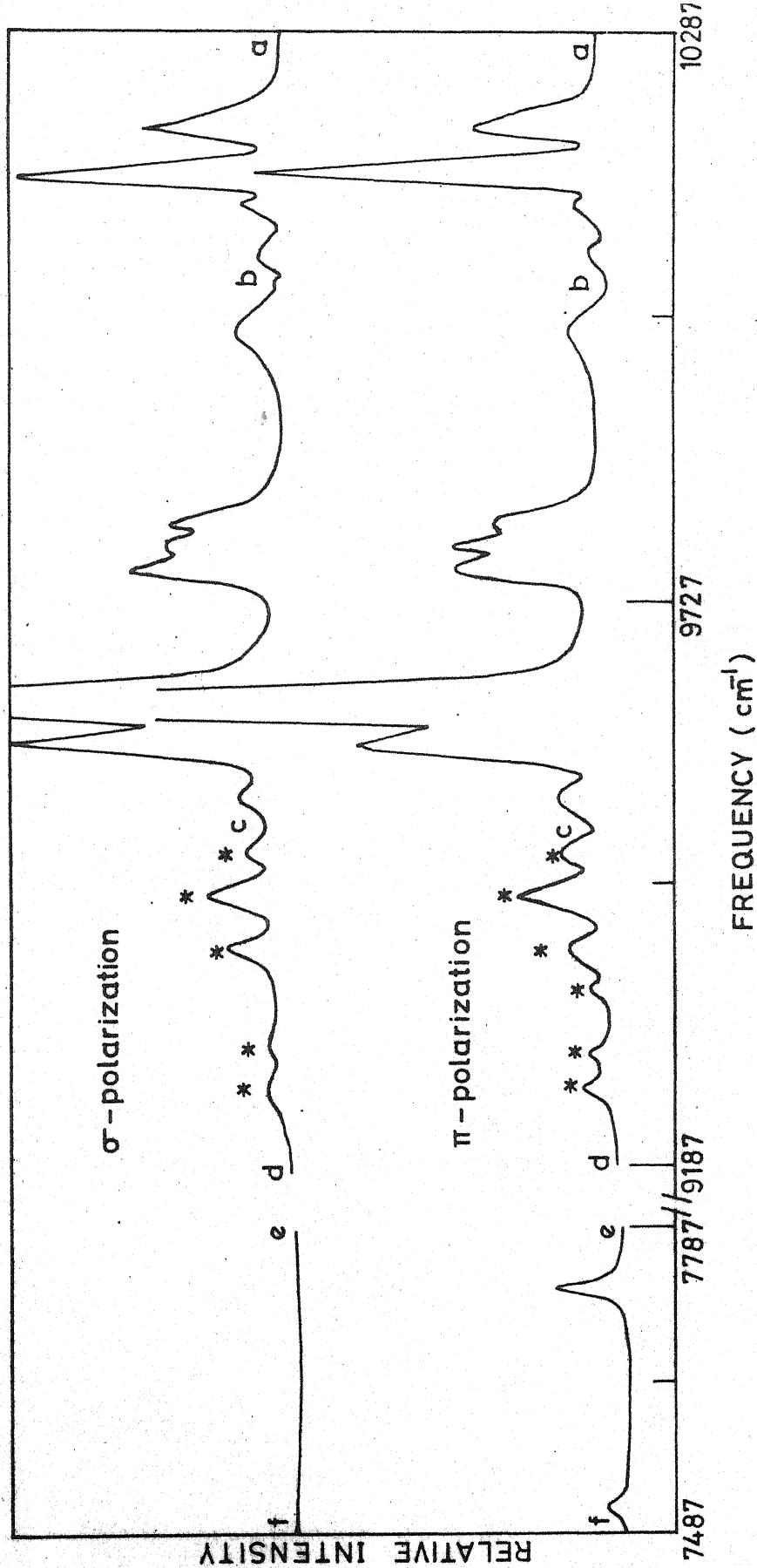
Fig. II.15 Fluorescence spectra of Pr^{3+} and Nd^{3+} in $PbMoO_4$ single crystals at 90K.

* – Lines correspond to the fluorescence of Nd^{3+}.

43

TABLE II-3

Observed Fluorescence from $^3P_0$ Level of Pr^{3+} in $PbMoO_4$ at 90 K

Terminal multiplet	Line Position (cm^{-1})	FWHM (cm^{-1})	Relative Intensity (arbitrary Units) I_π	I_σ	Stark Components (cm^{-1})	S_4 Symmetry assignments
$^3H_4$	20499	16	9850	445	0	$\Gamma_1 \to \Gamma_2$
	20438	11	1800	5400	61	$\Gamma_1 \to \Gamma_3$
	20378	30	990	170	–	
	20324[a]	–	–	–	–	
	20317[a]	35	185	100	–	
	20176	–	–	–	–	
	20101	60	340	385	398	$\Gamma_1 \to \Gamma_3$
$^3H_5$	18278	7	110	330	2221	$\Gamma_1 \to \Gamma_3$
	18254	8	20	45	2245	$\Gamma_1 \to \Gamma_3$
	18010	19	770	95	2489	$\Gamma_1 \to \Gamma_2$
$^3H_6$	16180	11	2700	1575	4319	$\Gamma_1 \to \Gamma_2$
	16133	11	700	4900	4366	$\Gamma_1 \to \Gamma_3$
$^3F_2$	15461	6	4900	–	5038	$\Gamma_1 \to \Gamma_2$
	15452	9	–	8460	5047	$\Gamma_1 \to \Gamma_3$
	15406	50	72	20	–	
	15336	25	108	115	–	
$^3F_3$	14115	3	36	220	6384	$\Gamma_1 \to \Gamma_3$
	14086	3	208	48	6403	$\Gamma_1 \to \Gamma_2$
	14019	4	32	4	6413	$\Gamma_1 \to \Gamma_2$
	13990	3	–	8	6480	$\Gamma_1 \to \Gamma_3$

contd.

TABLE II-3 (contd.)

Terminal Multiplet	Line Position (cm^{-1})	FWHM (cm^{-1})	Relative Intensity (arbitrary units)		Stark Components (cm^{-1})	S_4 Symmetry assignments
			I_{π}	I_{σ}		
$^3F_4$	13687	5.5	36	224	6812	$\Gamma_1 \to \Gamma_3$
	13662	4.5	282	44	6837	$\Gamma_1 \to \Gamma_2$
$^1G_4$	10960[b]	–	5	–	9539	$\Gamma_1 \to \Gamma_2$
	10916[b]	–	4	–	9583	$\Gamma_1 \to \Gamma_2$

a – refers to the vibronic lines.
b – refers to the lines recorded with PbS detector.

TABLE II-4

Observed Fluorescence From $^1D_2$ Level of Pr^{3+} in $PbMoO_4$ at 90 K

Terminal Multiplet	Line Position (cm^{-1})	FWHM (cm^{-1})	Relative Intensity arbitrary units		Stark Component (cm^{-1})	S_4-Symmetry Assignment
			I_π	I_σ		
$^3H_4$	16755	—	v.w.	—	61	$\Gamma_3 \to \Gamma_3$
	16632	16	3700*	1050	0	$\Gamma_1 \to \Gamma_2$
	16571	16	400	4700	61	$\Gamma_1 \to \Gamma_3$
	16522	12	300	4300	61	$\Gamma_2 \to \Gamma_3$
	16452	—	500	—	131	$\Gamma_1 \to \Gamma_2$
$^3H_5$	14387	22	—	20		
	14375	8	32	16		
	14361	8	—	8	2221	$\Gamma_2 \to \Gamma_3$
	14338	5	—	2		
$^3H_6$	12310	—	22	12	4319	$\Gamma_1 \to \Gamma_2$
	12210	—	18	18	4366	$\Gamma_2 \to \Gamma_3$
	12187	—	20	—	4396	$\Gamma_2 \to \Gamma_1$
	12085	—	8.0	10	4555	$\Gamma_1 \to \Gamma_3$
	12028	—	—	6		$\Gamma_2 \to \Gamma_3$

TABLE II-4 (contd.)

Terminal Multiplet	Line Position (cm^{-1})	FWHM (cm^{-1})	Relative Intensity (arbitrary units)		Stark Component (cm^{-1})	S_4 Symm. Assignment
			I_π	I_σ		
$^3F_2$	11587	—	36	46	5047	$\Gamma_1^7 \rightarrow \Gamma_3^7$
	11534	—	24	30		$\Gamma_2^7 \rightarrow \Gamma_3^7$
$^3F_3$	10195	—		52	6388	$\Gamma_1^7 \rightarrow \Gamma_3^7$
	10153	—	142	106	6480	$\Gamma_1^7 \rightarrow \Gamma_2^7$
	10121	—	22		6509	$\Gamma_1^7 \rightarrow \Gamma_3^7$
	10072	—				$\Gamma_2^7 \rightarrow \Gamma_3^7$
$^3F_4$	9813	—	52	40	6812	$\Gamma_1^7 \rightarrow \Gamma_3^7$
	9792	—	58	48	6837	$\Gamma_1^7 \rightarrow \Gamma_2^7$
	9767	—	76	58	6812	$\Gamma_2^7 \rightarrow \Gamma_3^7$
	9638	—	400	390	6944	$\Gamma_2^7 \rightarrow \Gamma_1^7$
	9598	—	--	--	6985	$\Gamma_2^7 \rightarrow \Gamma_3^7$
	9541	—	20	—	7044	$\Gamma_2^7 \rightarrow \Gamma_1^7$

A very weak but observable

*with 4765 Å laser excitation and 50 μ slit width, this line
generates 25 nA PMT anode current (PMT M12FC51 sensitivity
= 109 μA/lm).

TABLE II-5

Fluorescence of Nd^{3+} in $PbMoO_4$ at 90 K from the Level $^4F_{3/2}$

Terminal Multiplet	Line Position (cm^{-1})	Relative Intensity arbitrary units I_π	I_σ	Position of Stark Component (cm^{-1})	S_4 Symmetry assignment
$^4I_{9/2}$	11435[a]	70	–	–	?
	11397[b]	60	–	0	$\Gamma_7 \to \Gamma_7$ (?)
	11355	90	80	96	$\Gamma_6 \to \Gamma_7$
	11304	50	75		$\Gamma_7 \to \Gamma_7$
	11251	160	140	146	$\Gamma_7 \to \Gamma_6$
	11191	160	140	206	$\Gamma_7 \to \Gamma_6$
	11089	80	50	363	$\Gamma_6 \quad \Gamma_7$
	11033	100	100		$\Gamma_7 \quad \Gamma_7$
$^4I_{11/2}$	9490	189	118	1961	$\Gamma_6 \to \Gamma_7$
	9447	355	284	2004	$\Gamma_6 \to \Gamma_7$
	9394	165	213		$\Gamma_6 \to \Gamma_7$
	9357	118	–	2040	$\Gamma_7 \to \Gamma_6$
	9294	118	–	2157	$\Gamma_6 \to \Gamma_7$
	9262	142	–	2135	$\Gamma_7 \to \Gamma_6$

a - Origin of the line could not be understood

b - Polarization is not in accordance to the selection rules

49
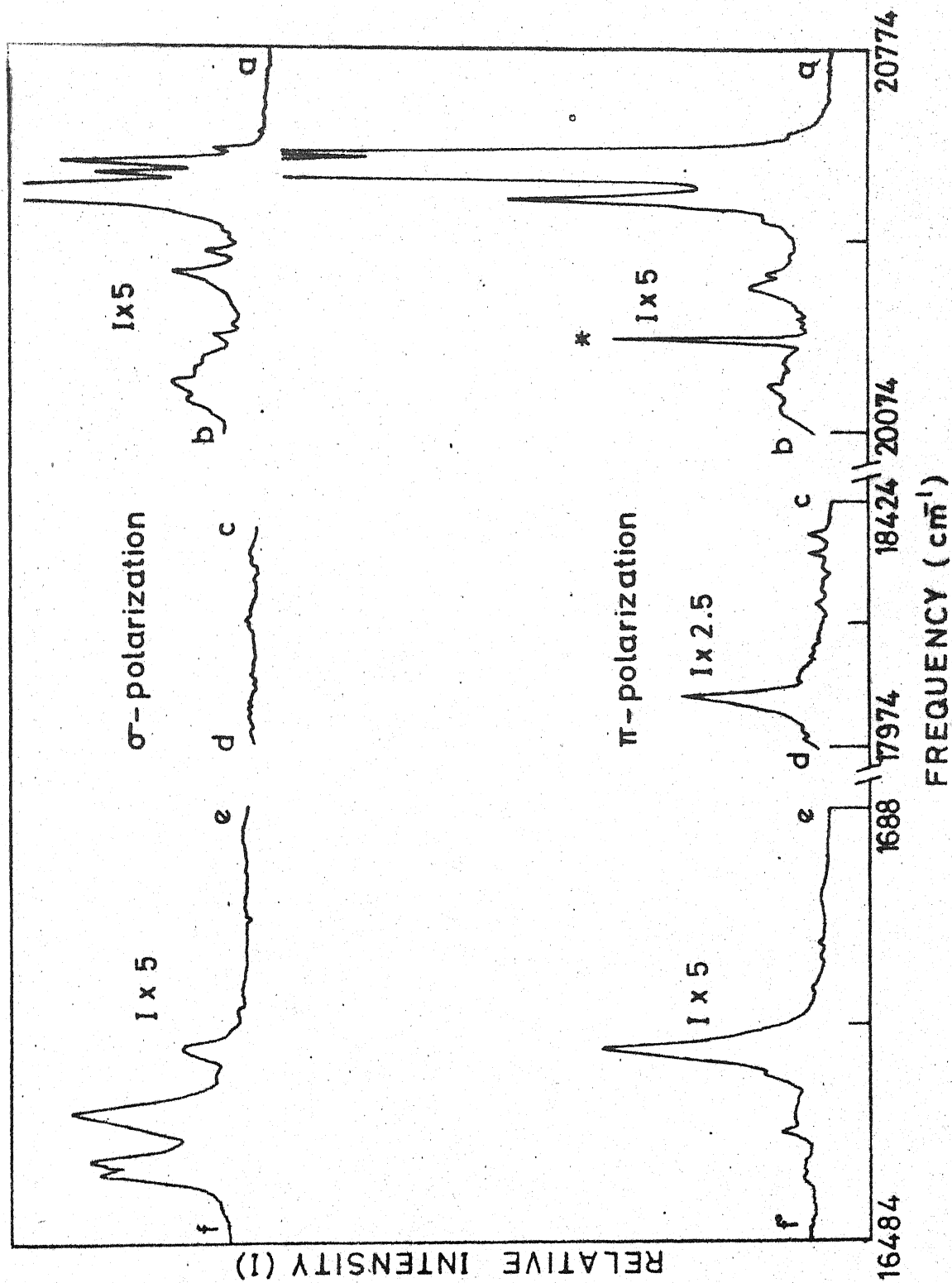
Fig. II.16 Fluorescence spectra of Pr³⁺ in PbWO₄ single crystals at 90K.
*—Raman lines
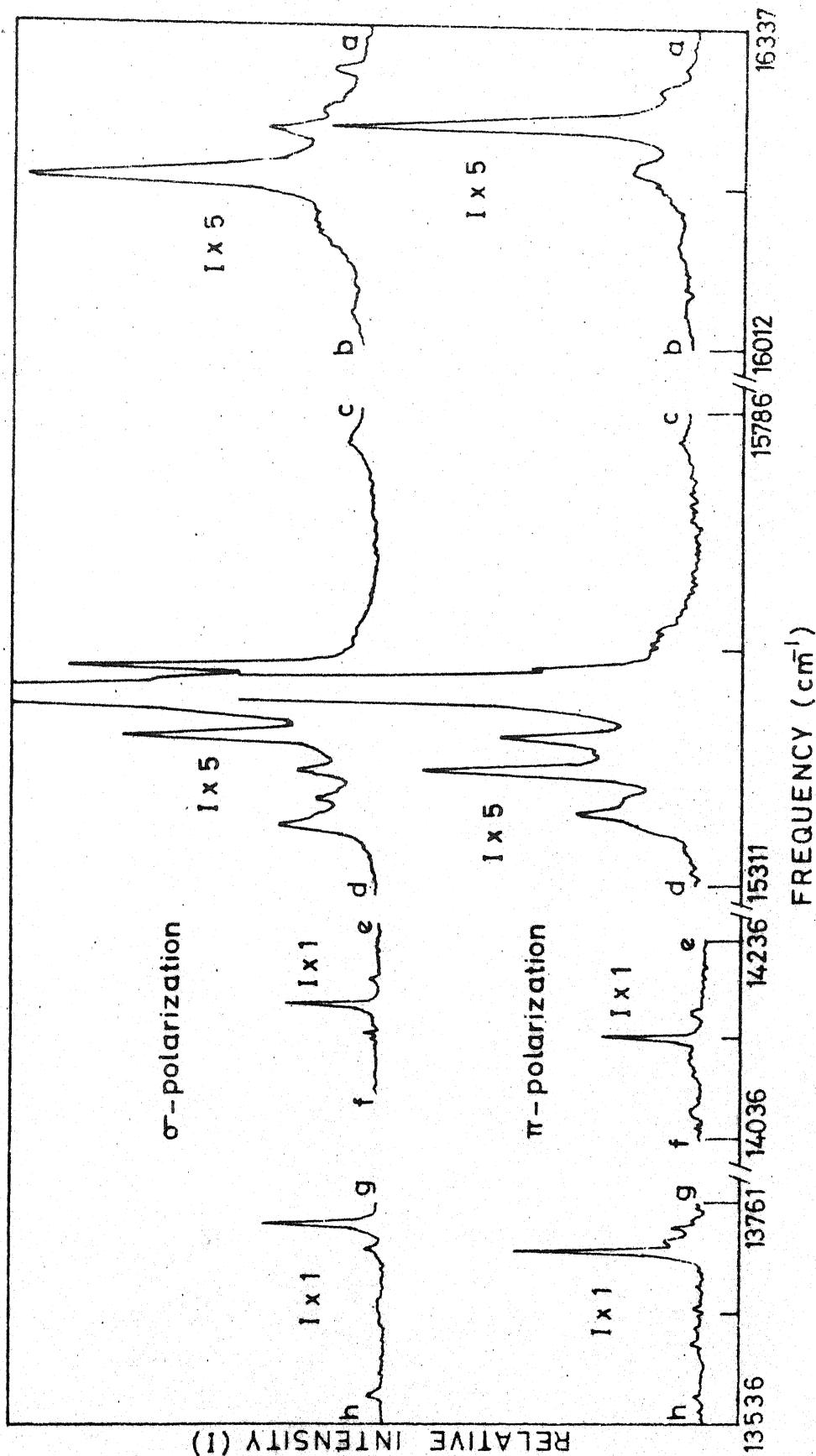
Fig. II.17 Fluorescence spectra of Pr^{3+} in $PbWO_4$ single crystals at 90 K.

50

TABLE II-6

Fluorescence of Pr^{3+} in $PbWO_4$ from $^3P_0$ Level at 90 K

Terminal Multiplet	Line Position (cm^{-1})	FWHM (cm^{-1})	Relative Intensity arbitrary units		Stark Component (cm^{-1})	S_4 Symmetry Assignment
			I_π	I_σ		
$^3H_4$	20586	12	1500	100		$\Gamma_1 \rightarrow \Gamma_2$
	20564	12	9300	370	0	$\Gamma_1 \rightarrow \Gamma_2$
	20543	15	—	320		$\Gamma_3 \rightarrow \Gamma_2$
	20502	18	—	2000	62	$\Gamma_1 \rightarrow \Gamma_3$
	20398[a]	20	—	120		
	20362[a]	35	120	170		
	20335[a]	45	150	—		
	20245[a]	—	—	—		
	20155	35	120	170	409	$\Gamma_1 \rightarrow \Gamma_3$
$^3H_5$	18061	25	140	—	2503	$\Gamma_1 \rightarrow \Gamma_2$
$^3H_6$	16299[b]	10	30	70		
	16277[b]	15	85	—		
	16239	14	735	200	4325	$\Gamma_1 \rightarrow \Gamma_2$
	16191	20	140	695	4373	$\Gamma_1 \rightarrow \Gamma_3$

contd.

TABLE II-6 (contd.)

Terminal Multiplet	Line Position (cm^{-1})	FWHM (cm^{-1})	Relative Intensity arbitrary units		Stark Component (cm^{-1})	S_4 Symmetry Assignment
			I_π	I_σ		
$^3F_2$	15527	10	330	625	5056	$\Gamma_1 \to \Gamma_2$
	15507	10	890	–		$\Gamma_1 \to \Gamma_2$
	15501	9	–	4250	5063	$\Gamma_1 \to \Gamma_3$
	15458[b]	12	390	510		
	15424[b]	15	550	160		
	15397[b]	12	–	120		
	15381[b]	15	245	–		
	15369[b]	12	–	200		
$^3F_3$	14191	3	–	6	6399	$\Gamma_1 \to \Gamma_3$
	14165	3	6	38		$\Gamma_1 \to \Gamma_3$
	14137	3	40	5	6427	$\Gamma_1 \to \Gamma_2$
$^3F_4$	13737	6	14	50	6827	$\Gamma_1 \to \Gamma_3$
	13721	6	16	–		$\Gamma_3 \to \Gamma_3$
	13710	6	76	9	6854	$\Gamma_1 \to \Gamma_2$

a - refers to vibronic transition

b - origin of this line not understood

TABLE II-7

Fluorescence from $^1D_2$ of Pr^{3+} in $PbWO_4$ at 90 K

Terminal Multiplet	Line pos. (cm^{-1})	FWHM (cm^{-1})	Relative Intensities (arb. units) I_π	I_σ	Stark Component (cm^{-1})	S_4 Symm. Assignment
$^3H_4$	16865	–	–	10	0	$\Gamma_3 \to \Gamma_2$
	16661	20	420	75	0	$\Gamma_1 \to \Gamma_2$
	16601	27.5	–	340	61	$\Gamma_1 \to \Gamma_3$
	16557	22.5	–	310	61	$\Gamma_1 \to \Gamma_3$
	16545[a]	17.5	–	290		?

a - Origin not clear
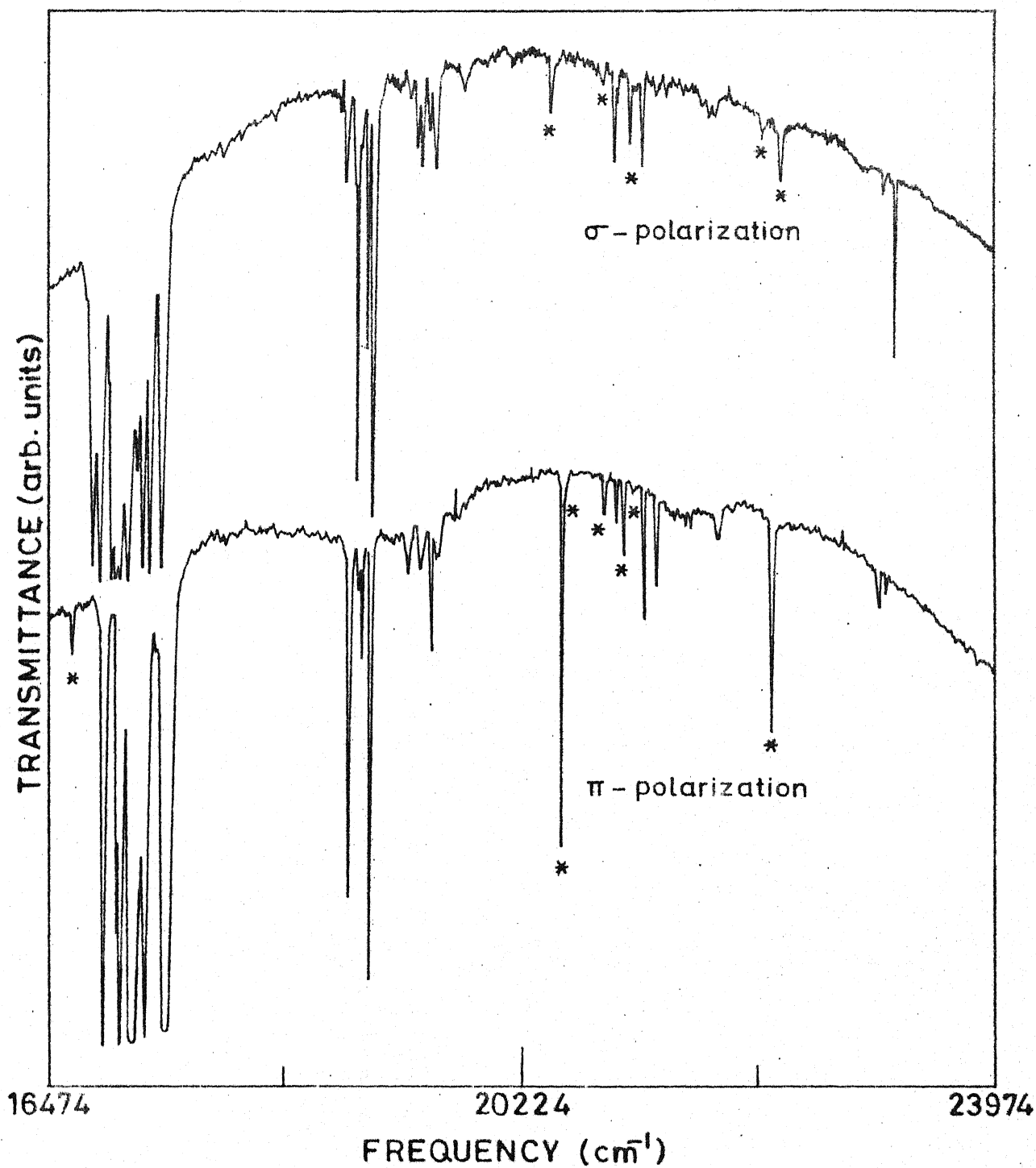
Fig. II. 18   Absorption spectra of Pr^{3+} and Nd^{3+} in $PbMoO_4$ single crystal at 90 K.

✻ – Lines correspond to Pr^{3+}.

TABLE II-8

Absorption Data for Pr^{3+} in $PbMoO_4$ at 90 K

Multiplet	Absorption Energy (cm^{-1})	FWHM (cm^{-1})	Relative Intensity (arbitrary units) I_π	I_σ	Assignments
$^3F_4$	6807^a	–	–	–	$\Gamma_2 \to \Gamma_1$
$^1D_2$	16632	16.0	225	–	$\Gamma_2 \to \Gamma_1$
$^3P_0$	20438	15.0	–	150	$\Gamma_3 \to \Gamma_1$
	20499	11.0	1400	–	$\Gamma_2 \to \Gamma_1$
$^1I_6$	20522	–	100	–	$\Gamma_2 \to \Gamma_1$
	20834^b	20.0	250	–	?
$^3P_1$	20992	20.0	250	–	$\Gamma_3 \to \Gamma_3$
	21053	12.5	50	225	$\Gamma_2 \to \Gamma_3$
	22112	30.0	–	100	$\Gamma_3 \to \Gamma_1$
	22175	23.0	1100	–	$\Gamma_2 \to \Gamma_1$
	22260	25.0	–	500	$\Gamma_2 \to \Gamma_3$

a - This line was recorded on Carry-14.

b - The interrogation mark "?" in the last column indicates that the origin of this line is not understood.
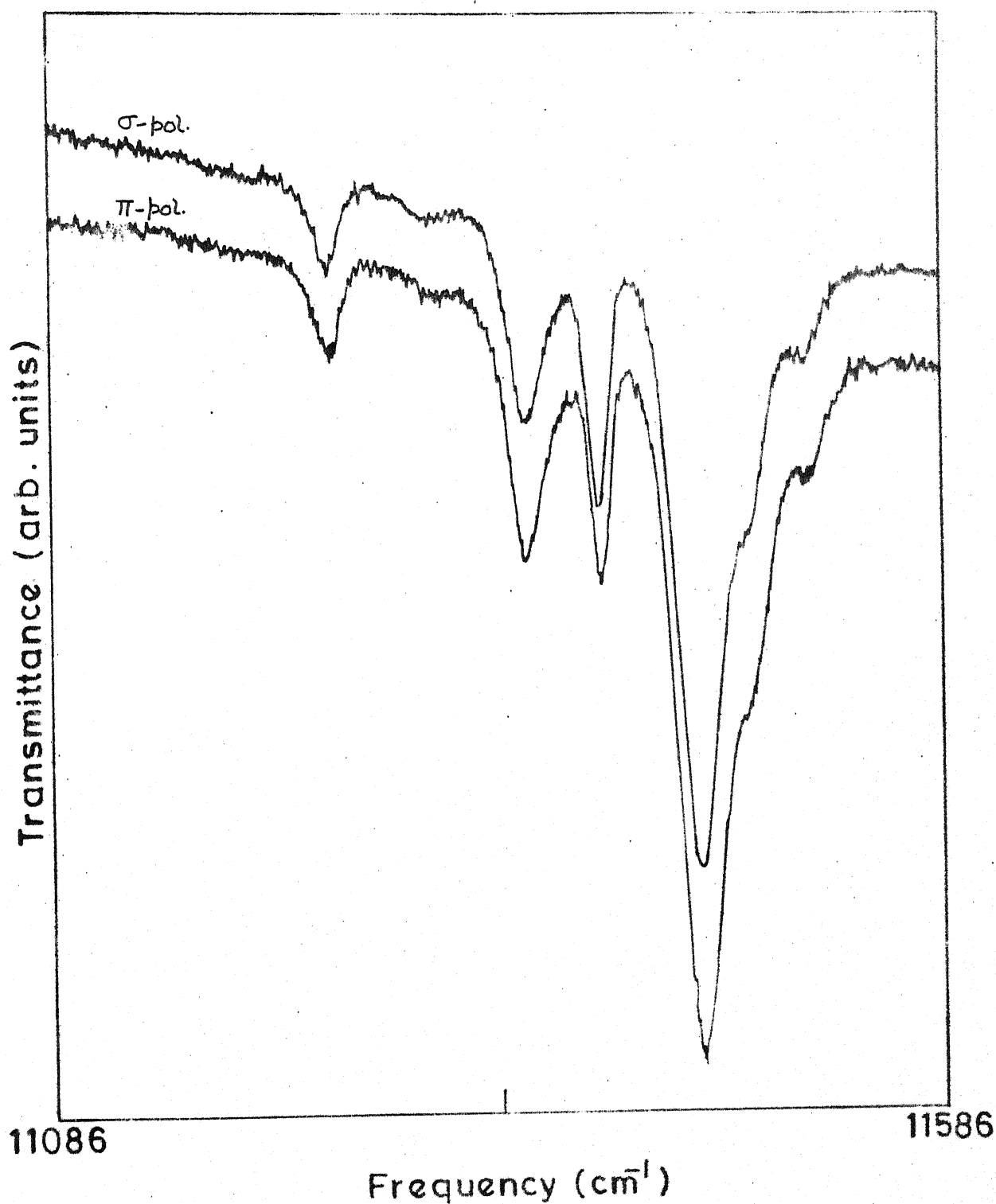
Fig.II.19   Absorption from $^4I_{9/2} \longrightarrow {}^4F_{3/2}$ state
Nd^{3+} in PbMoO$_4$

TABLE II-9

Absorption Data for $^4I_{9/2}$, $^4F_{3/2}$ Level of Nd^{3+} in $PbMoO_4$ at 90 K.

Absorption Energy (cm^{-1})	Relative Intensity		Energy of $^4I_{9/2}$ Stark Component (cm^{-1})	S_4 Symmetry Assignment
	I_π (arbitrary units)	I_σ		
11451	1560	1340	0	$\Gamma_7 \rightarrow \Gamma_6$
11397	500	500	0	$\Gamma_7 \rightarrow \Gamma_7$
11355	500	360		$\Gamma_7 \rightarrow \Gamma_6$
11306	30	40	96	$\Gamma_7 \rightarrow \Gamma_7$
11246	200	180	205	$\Gamma_6 \rightarrow \Gamma_7$

Fig. II. 20   Absorption spectra of Pr^{3+} and Nd^{3+} in PbWO$_4$ single crystal at 90 K.

* – Lines correspond to Pr^{3+}.
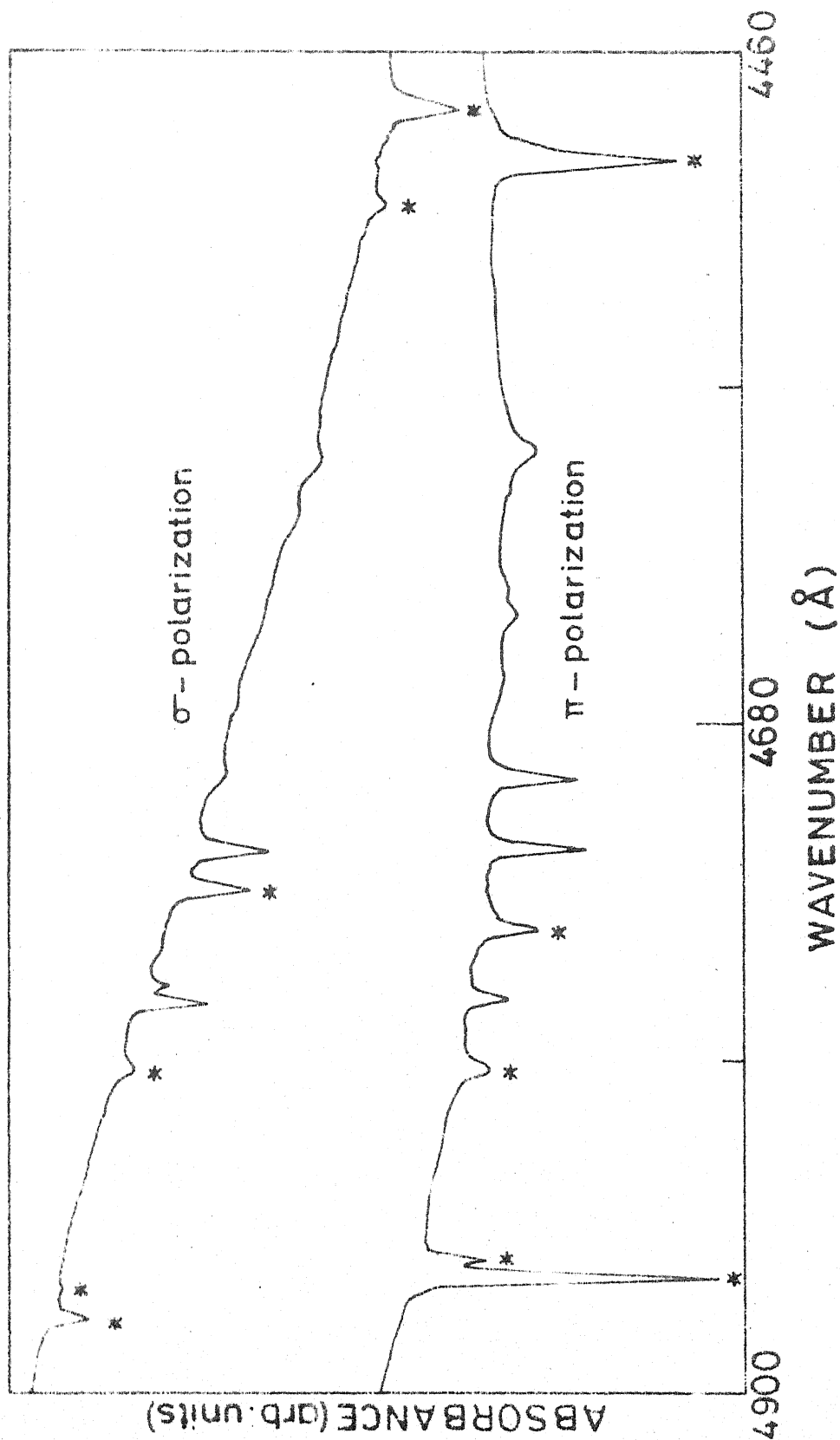
Fig. II.21 Absorption spectra of Pr^{3+} and Nd^{3+} in $PbWO_4$ single crystals at 90K.

∗ - Lines correspond to Pr^{3+}.

TABLE II-10

Absorption Data for Pr^{3+} in $PbWO_4$ at 90 K

Multiplet	Absorption Energy (cm^{-1})	FWHM (cm^{-1})	Relative Intensity arbitrary units		S_4-Symmetry assignment
			I_π	I_σ	
$^1D_2$	16661	15	140	–	$\Gamma_2 \rightarrow \Gamma_1$
$^3P_0$	20502	15	–	100	$\Gamma_3 \rightarrow \Gamma_1$
	20564	15	820	–	$\Gamma_2 \rightarrow \Gamma_1$
$^1I_6$	20543	–	–	v.w.*	$\Gamma_2 \rightarrow \Gamma_3$
	20586	14	170	–	$\Gamma_2 \rightarrow \Gamma_1$
	20859[a]	18	80	50	?
$^3P_1$	21056	21	150	–	$\Gamma_3 \rightarrow \Gamma_3$
	21118	21	–	190	$\Gamma_2 \rightarrow \Gamma_3$
$^3P_2$	22179	23	–	50	$\Gamma_3 \rightarrow \Gamma_1$
	22241	26	500	–	$\Gamma_2 \rightarrow \Gamma_1$
	22321	29	–	200	$\Gamma_2 \rightarrow \Gamma_3$

a – Origin of the line not understood.
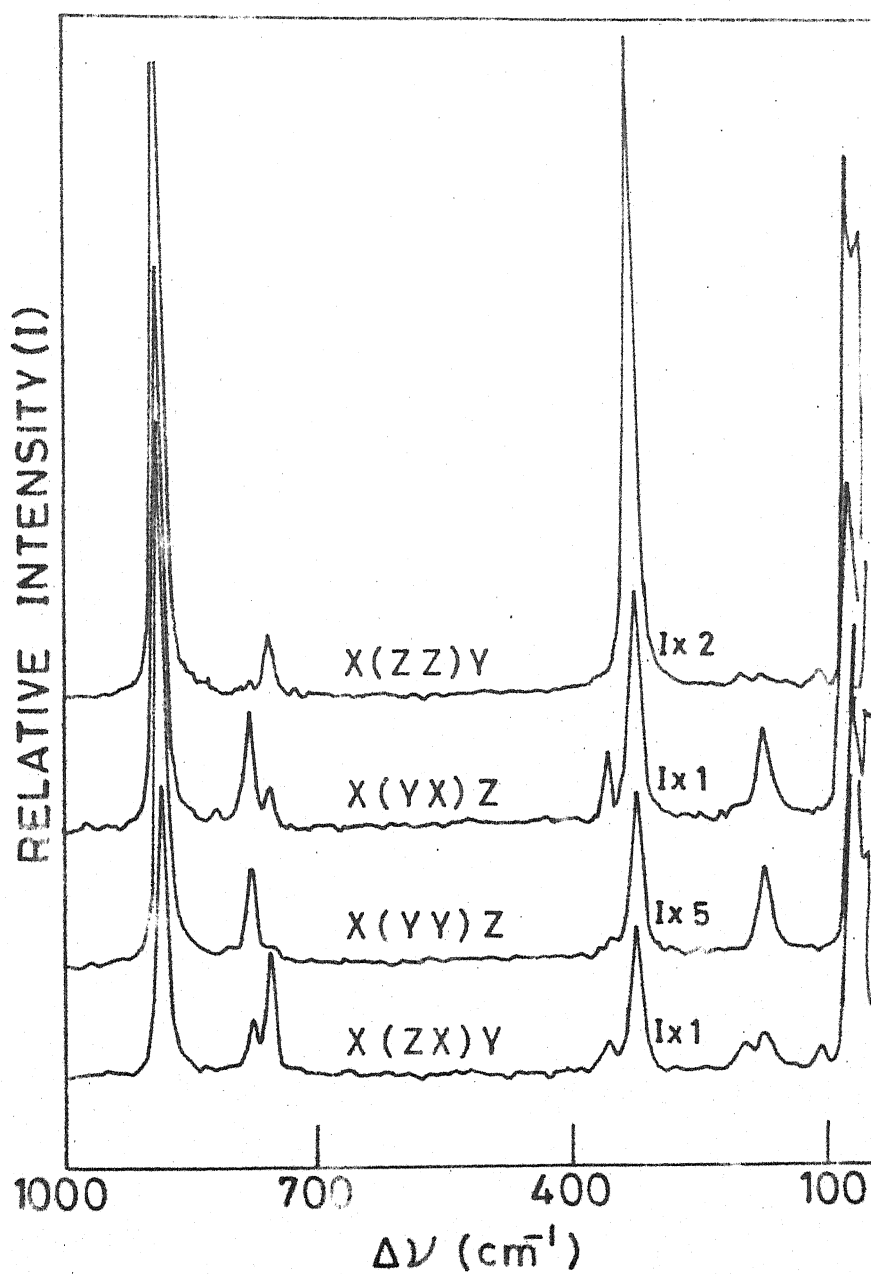
Fig. II. 22   Raman spectra (stokes) of $PbMoO_4$
single crystal at room temperature.
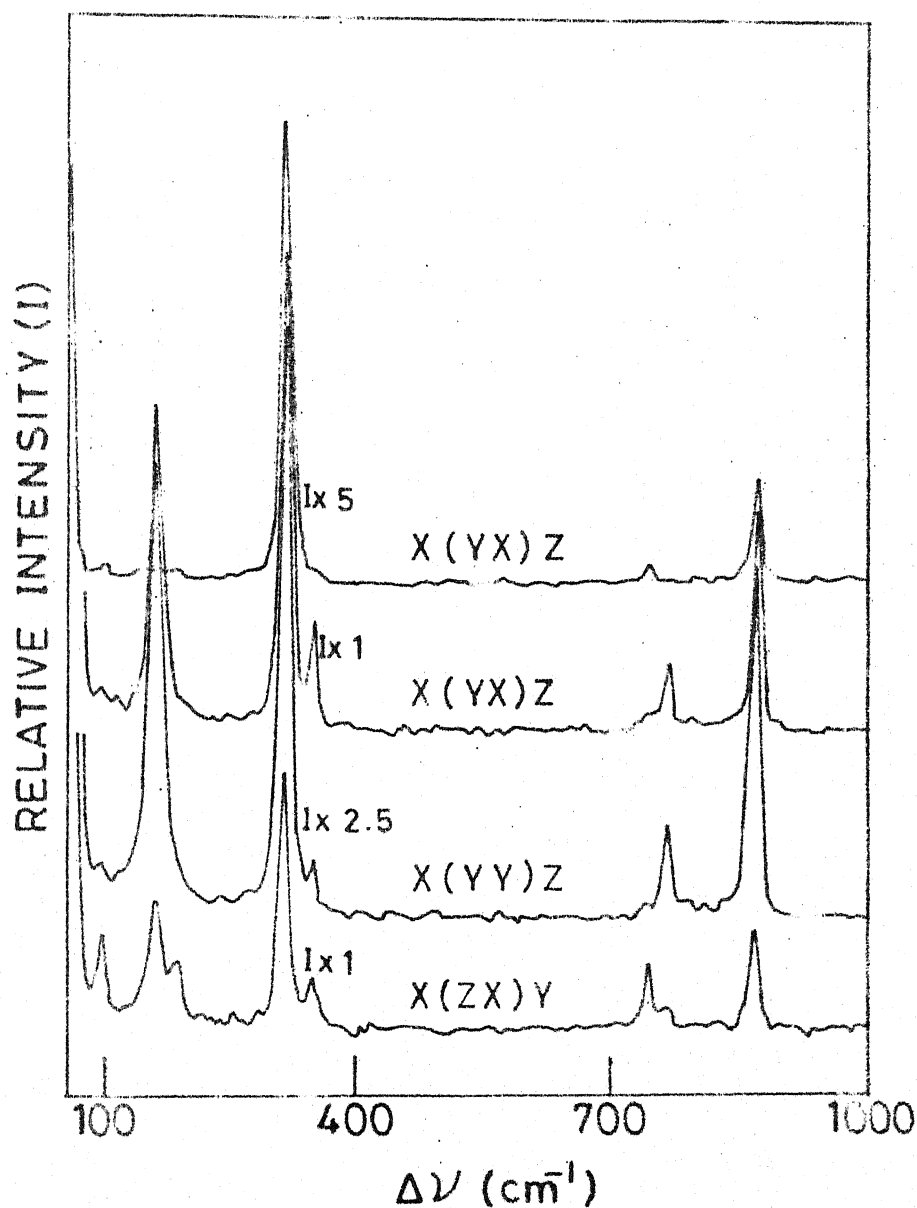
Fig.II.23   Raman spectra(antistokes) of $PbMoO_4$ single crystal at room temperature.

TABLE II-11

<u>Room Temperature Relative Intensities of Raman Active</u>
<u>Vibrational Frequencies of PbMoO$_4$ Single Crystal in</u>
<u>Various Geometries.</u>

Vibrational Frequency (cm^{-1})	Relative Intensity (arb. units)			
	x(zz)y	x(zx)y	x(yy)z	x(yx)z
871	1950	340	6500	590
768	–	50	1050	120
744	–	140	–	40
350	–	35	–	–
348	–	–	250	70
319	1500	170	1900	–
318	–	–	–	270
191	–	30	–	–
167	20	40	950	100
102	–	25	–	–
74	–	–	–	–
65	–	–	1500	165
62	–	350	–	–
54	v.w.	–	–	v.w.
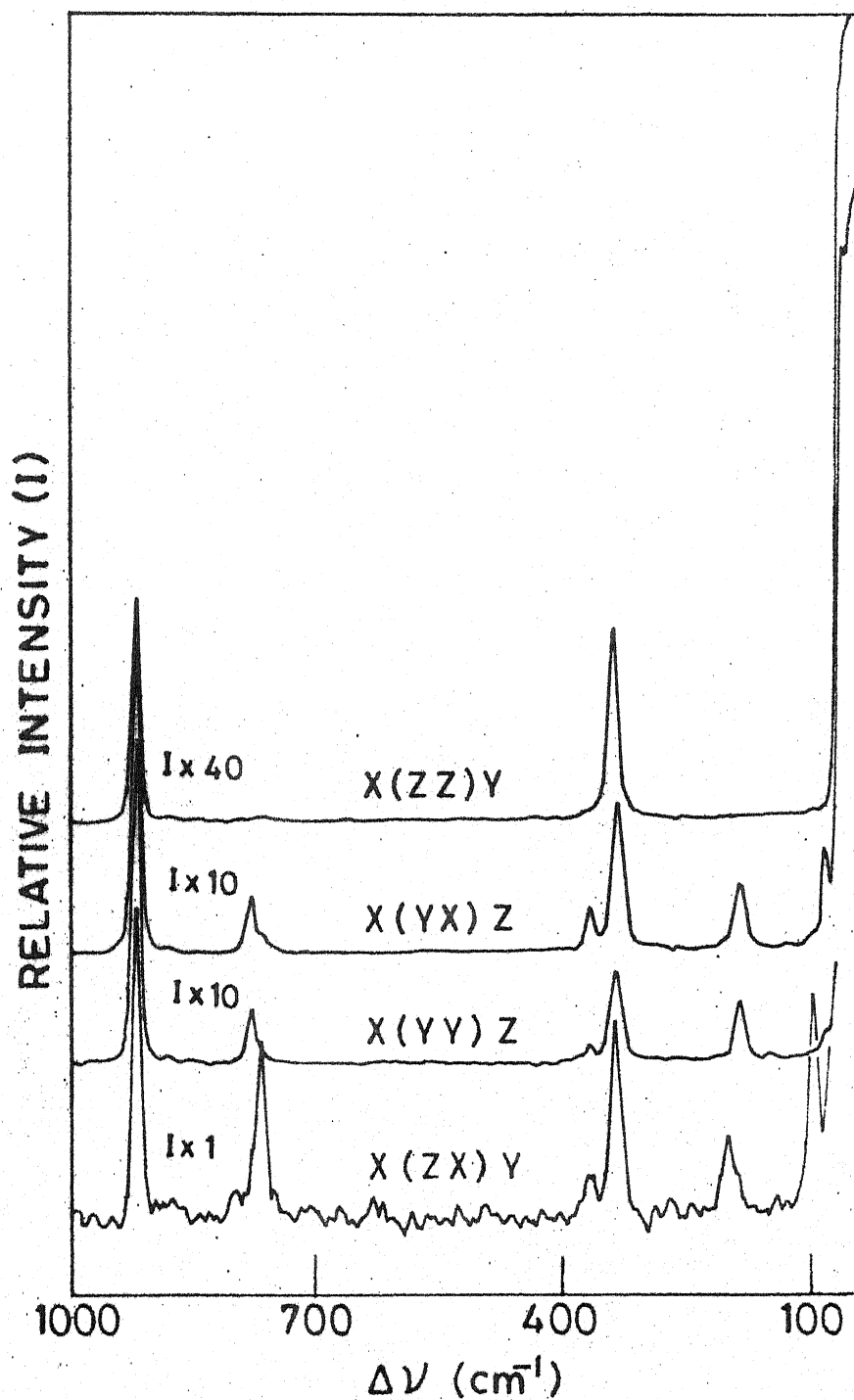
Fig. II. 24   Raman spectra (stokes) of $PbWO_4$ single crystal at room temperature.

RELATIVE INTENSITY (I)
I x 4
X(Z Z)Y
I x 2
X(YX)Z
I x 1
X(YY)Z
I x 1
X(ZX)Y
100
400
700
1000
$\Delta\nu$ (cm^{-1})
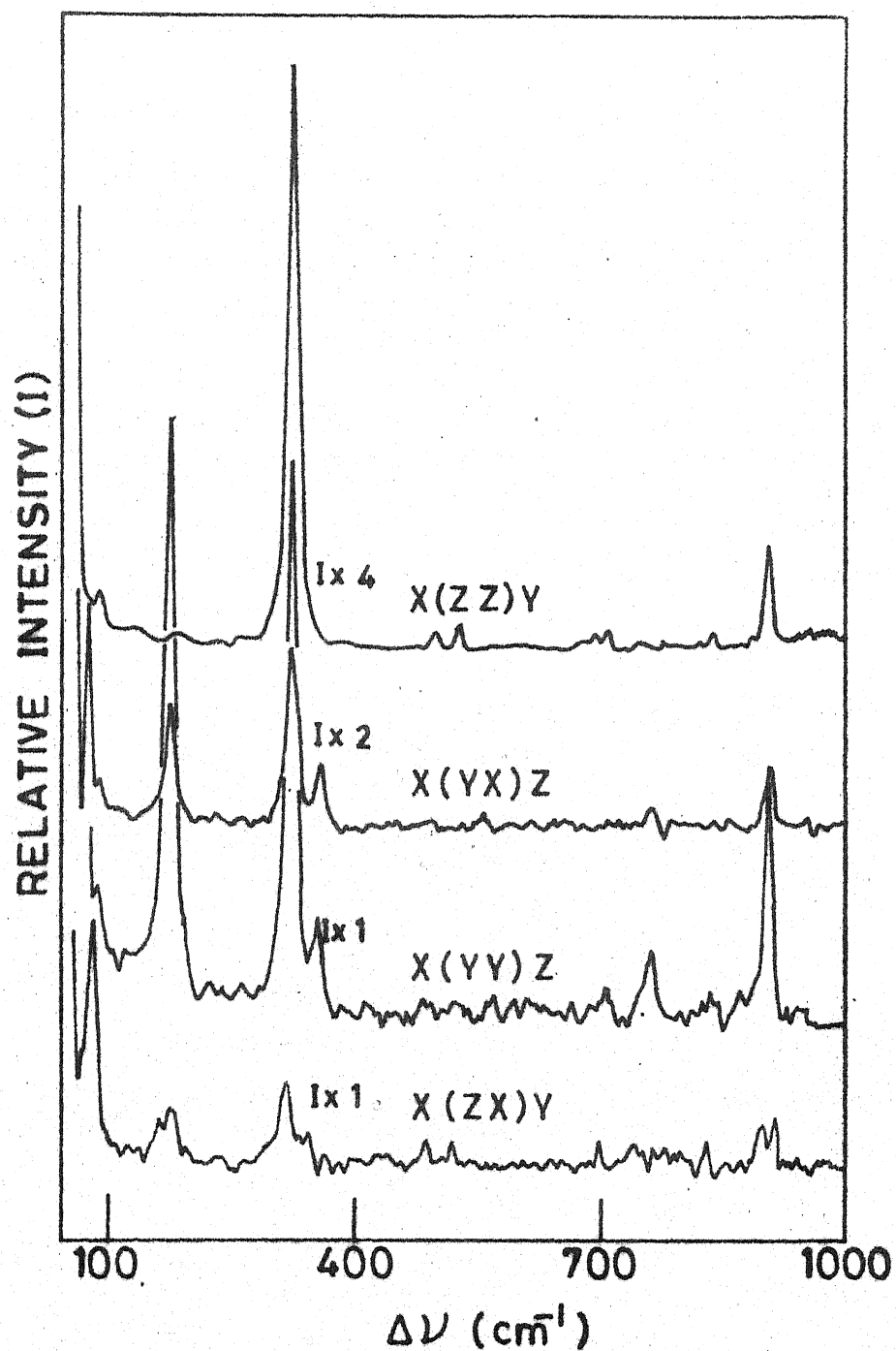
Fig.II.25 Raman spectra (antistokes) of $PbWO_4$ single crystal at room temperature.

TABLE II-12

<u>Room Temperature Relative Intensities of Raman Active Vibrational</u>
<u>Frequencies of $PbWO_4$ Single Crystal in Various Geometries</u>

Vibrational Frequency (cm^{-1})	Relative Intensity (arb. units)			
	x(zz)y	x(zx)y	x(yy)z	x(yx)z
905	1100	40	1520	385
766	–	3.5	280	70
753	–	22	–	10
360	–	5.0	–	–
358	–	–	80	50
328	840	23.5	340	–
325	–	–	200	175
193	–	10	–	–
178	–	4	280	80
89	–	25	–	–
76	–	–	–	80
62	–	130	–	–
54	1920	256	980	450
52	–	–	–	250

REFERENCES

1. L.F. Johnson, J. Appl. Phys. (USA) $\underline{34}$, 897 (1963).

2. V.L. Bakumenko et al., Opt. and Spect. $\underline{19}$, 68 (1965).

3. A.A. Kaminskii and S.E. Sarkisov, Sov. J. of Q. Electronics (USA) $\underline{3}$, 248 (1973).

4. L. Esterowitz et al., J. Appl. Phys. (USA) $\underline{48}$, 650 (1977).

5. Douglas A. Pinnow, IEEE Journal of Quantum Electronics, $\underline{qE-6}$, 223 (1970).

6. R.W.G. Wyckoff, Crystal Structures Vol.II (Interscience Publishers, Inc., New York) 1960.

7. Janusz Leciejewicz, Zeitschrift fur Kristallographie, Bd $\underline{121}$, S158-164 (1965).

8. K. Nassau and G.M. Loiacono, Phys. Chem. Solids $\underline{24}$, 1503 (1963).

9. G.R. Jones, Optical Properties of Ions in Crystals (Interscience Publishers, New York 1967) pp 85-103; Editors: H.M. Crosswhite and H.W. Moos.

10. K. Nassau and A.M. Broyer, J. Appl. Phys. $\underline{33}$, 3064 (1962).

11. I.S.Minhas, A Study of the Optical Properties of $Nd^{3+}:PbMoO_4$ System – Ph.D. dissertation.

12. T. Shiga, K. Shiga and M. Kuroda, Anal. Biochem. $\underline{44}$, 291 (1971).

13. J.H. Obink and M.F. Hezemans, Journal of Physics E : Scientific instruments $\underline{10}$, 769 (1977).

14. N.S. Tukarov, Instruments and Experimental Tech. $\underline{2}$, 1195 (1967).

CHAPTER III

THEORETICAL FRAMEWORK

1. INTRODUCTION

In the sixth period, the lanthanides (Ce; Pr; Nd; Pm; Sm; Eu; Gd; Tb; Dy; Ho; Er, Tm; Yb) and in the seventh period the actinides (Th; Pa; U; Np; Pu; Am; Cm; Bk; Cf) have ground configurations containing f-optical electrons. The neutral lanthanides have, in addition to 4f-electrons, a xenon closed shell structure of electrons ($1s^2$, $2s^2$, $2p^6$, $3s^2$, $3p^6$, $3d^{10}$, $4s^2$, $4p^6$, $4d^{10}$, $5s^2$, $5p^6$) and $6s^2$ or $6s^2 5d$ outer electrons. The loosely held 5d and $6s^2$ electrons are readily detached from the atoms giving rise to stable trivalent ions both in pure metals and in salts. Though the 3+ oxidation state is most stable for the lanthanides, other oxidation states also have been found to exist.

Mayer and others[1,2] have shown that the imperfect shielding among the 4f-electrons results in an increased nuclear attraction for f-electrons as atomic number increases in the lanthanide series. Development of this potential well near the nucleus causes the reduction in the spatial extension of the $4f^n$ shell such that the 4f radial wavefunction peak lies closer to the nucleus than the peaks of $5s^2$ and $5p^6$ radial wavefunctions[3]. The shielding of the 4f-electrons by the outer $5s^2 5p^6$ electrons prevents any strong interaction of the f-electrons

with their environment. Consequently, the natural course
of our approach for the theoretical interpretation of
rare earth ions will be to neglect their interaction with
the crystalline environment at the first stage of calcu-
lation and concentrate on the free ion interactions. Fair
amount of information on the free ion levels of rare earth
ions can be extracted from 'centres of gravity' of the
observed groups of lines in their crystal spectra. The
crystal field interaction can then be treated as small
perturbation to the free ion Hamiltonian.

2. FREE ION TREATMENT

2.1 Central Field Approximation

For the theoretical interpretation of free ion
spectrum, one is required to solve the Schrodinger equation

$$H_F \Psi_{CF} = E_F \Psi_{CF}. \tag{3.1}$$

Free ion Hamiltonian H_F for N electrons can be written
as

$$H_F = -\frac{\hbar^2}{2m} \sum_i \nabla_i^2 - \sum_i \frac{Ze^2}{r_i} + \sum_{i<j} e^2/r_{ij}$$

$$+ \sum_i \zeta(r_i).(\hat{l}_i.\hat{s}_i) \tag{3.2}$$

$$\text{where } \zeta(r_i) = \frac{\hbar^2}{2m^2c^2} \frac{1}{r_i} \frac{dU(r_i)}{dr_i} \tag{3.3}$$

r_i represents the distance between ith electron and the nucleus, r_{ij} is the interelectronic distance and other quantities have their usual meaning. In equation (3.2) summation is carried over all the N electrons.

The first term in the Hamiltonian is the sum of the kinetic energy of all the electrons, the second term is the potential energy of all the electrons in the field of the nucleus, the third term is the repulsive Coulomb interaction between the electrons and the last term represents the spin-orbit interaction.

For atoms containing more than one electron (even for the simplest ones), the Schrodinger equation can not be solved directly, neither analytically nor numerically. Therefore, the systematics of the spectra of multi electron systems should be based on some approximate models. A schematic treatment would be suitable in which the concept of the individual state of an electron in an atom is retained, and the state of an atom as a whole is determined by the aggregate of the states of the electrons, taking into account their interactions. To describe electron states in an atom one proceeds from the assumption that each electron moves in a centrally symmetric field created by the nucleus and all the other electrons. This approximation is called the central field approximation.[4] For the systematization of the spectrum, there is no need

to specify this field in a concrete form. A whole series of results can be obtained on the basis of general theory of motion of a particle in centrally symmetric field. A more detailed examination requires a treatment of the non-central part of the electrostatic interaction and also of the magnetic interaction, particularly the spin orbit interaction. In the theory of atomic spectra, these interactions are usually treated as small perturbations to the centrally symmetric field. The free-ion Hamiltonian may be rewritten in the following form :

$$H = \sum_{i=1}^{N} \left[-\frac{\hbar^2}{2m} \nabla_i^2 + U(r_i) \right] + \left[\sum_{i<j} e^2/r_{ij} \right.$$

$$\left. - \sum_{i=1}^{N} \frac{Ze^2}{r_i} - U(r_i) \right] + \sum_{i=1}^{N} \zeta(r_i)(\hat{l}_i \cdot \hat{s}_i)$$

$$= H_{CF} + H'_{Coul} + H'_{SO} \qquad (3.4)$$

where

$$H'_{Coul} = \left[\sum_{i<j} e^2/r_{ij} - \sum_{i=1}^{N} Ze^2/r_i \right] - U(r_i) \qquad (3.5)$$

The Schrodinger equation for the central field Hamiltonian,

$$H_{CF} \Psi_{CF} = E_{CF} \Psi_{CF} \qquad (3.6)$$

can be separated into individual electron coordinates by

choosing a solution such that

$$\Psi_{CF} = \prod_{i=1}^{N} \Phi_i \, (a_i) \qquad (3.7)$$

and

$$E_{lf} = \sum_{i=1}^{N} E(a^i) \qquad (3.8)$$

Each electron in the central field will satisfy the equation :

$$\left[- \frac{\hbar^2}{2m} \nabla^2 + U(r)\right] \Phi(a^i) = E(a^i) \Phi(a^i) \qquad (3.9)$$

where a^i represents a set of quantum numbers $(nlm\mu)$.

This equation differs from the equation of hydrogen atom only in that the central potential $U(r)$ appears here instead of the Coulomb potential $- Ze^2/r$. We can therefore use the results from the theory of hydrogen atom. The angular momentum is conserved during motion in a centrally symmetric field, therefore, each stationary state can be characterized by the assignment of quantum number and its Z component m. In a manner analogous to the theory of hydrogen atom, the wavefunction $\Phi(a^i)$ for stationary states can be written as

$$\Phi(r, \theta, \Phi) = r^{-1} R(r) \, Y_{lm}(\theta, \Phi) \qquad (3.10)$$

where $Y_{lm}(\theta, \Phi)$ are the spherical harmonics defined by

$$Y_{lm}(\theta, \Phi) = (-1)^m \left\{ \frac{(2l + 1)(l - m)!}{4\pi(l + m)!} \right\} P_l^m(\cos \theta) \, x \, e^{im\Phi}$$

$$.. \quad (3.11)$$

and

$$P_1^m(X) = \frac{(1 - x^2)^{m/2}}{2^1 1!} \frac{d^{1+m}}{dx^{1+m}}(x^2 - 1)^1 \qquad (3.12)$$

The radial part of the wavefunction R(r) satisfies the equation

$$\frac{1}{r^2} \frac{d}{dr}(r \frac{dR}{dr}) - \frac{1(1 + 1)}{r^2} R + \frac{2m}{\hbar^2}[E - U(r)] R = 0 \qquad (3.13)$$

Determination of the function R(r) requires an exact knowledge of U(r), usually this information is not available and one resorts to some sort of selfconsistent field calculations. For the interpretation of the spectra of trivalent rare earths, the radial quantities are generally treated as adjustable parameters to fit the experimental data. The parameterization procedure is particularly helpful for the consideration of configuration interactions as we shall see later.

The spin of the electron is taken into account by taking the product of $\bar{\phi}$ with α or β states, corresponding to the two possible orientations of the spin. Thus

$$\bar{\phi}(nlm\mu) = \delta(\sigma, \pm \frac{1}{2})r^{-1}R_{nl}(r) Y_{lm}(\theta, \varphi) \qquad (3.14)$$

where σ is spin coordinate operator. Properly antisymmetrized wave functions of a system consisting of N-noninteracting electrons can be expressed as a slater determinant

of the single electron functions $\bar{\phi}_i(a^i)$. Thus

$$\Psi_{CF} = \frac{1}{\sqrt{N}} \begin{vmatrix} \phi_1(a^1) & \phi_2(a^1) \ldots \ldots \phi_N(a^1) \\ \phi_1(a^2) & \phi_2(a^2) \ldots \ldots \phi_N(a^2) \\ \vdots \\ \vdots \\ \phi_1(a^N) & \phi_2(a^N) \ldots \ldots \phi_N(a^N) \end{vmatrix} \qquad (3.15)$$

Solutions of equation (3.6) give rise to a series of energy
levels called configurations. Each configuration is charac-
terized by the quantum numbers (n, l) for all the electrons
under consideration. Since the low lying configurations
are quite far apart, one can do the perturbation calcula-
tions for the H'_{Coul} and H'_{so} in single configuration using
the above mentioned determinantal product states as the
basis states. It can be shown that the closed shells shift
the configuration as a whole but do not affect the relative
separation of the level in the configuration[4]. Thus for an
isolated configuration one needs to consider the electrons
in unfilled shells only. This procedure will be suitable
only for most elementary configurations. Calculations
tend to be more cumbersome for configurations involving
f electrons. The complexity of the situation can be
illustrated by the fact that $4f^N$ configuration is
$14! / (14-N)! \, N!$ fold degenerate. Thus even for simplest

f^2 configuration, one is required to solve the 91x91 secular determinant consisting of the matrix elements of H'_{Coul} and H'_{SO} among 91 degenerate basis functions. This will be a very tedious task. The calculations tend be even more complicated as N increases. Moreover, this procedure does not provide any insight into the structure of a configuration. In the forthcoming sections we will discuss the techniques which will simplify these calculations.

2.2 Classification of States

As a rule, several identical terms arise from f^N like multi-electron configurations. Additional quantum numbers are then required for unambiguous identification of the | LS> states in such configurations.

Racah proposed a group theoretical approach[5],[6] for the classification of the states of f^N configuration. According to Racah the states can be classified by their properties under certain groups of transformation. The irreducible representations of these groups can then be used to label the basis states. For the complete speci-fication of these states four transformation groups required are

$$U_7 \text{ , } R_7 \text{ , } G_2 \text{ , } R_3$$

where

$$R_3 \subset G_2 \subset R_7 \subset U_7$$

The operators of the group U_7 consists of all tensor operators V^k, where $0 < k < 6$ and commute with spin $\hat{S}$. Therefore all the states of the configuration with given SM_s form the bases for the representations of the group U_7. The $(2l+1)$ integers $[\lambda_1, \lambda_2, \lambda_3 \ldots \ldots \lambda_{2l+1}]$ are required for the specification of the irreducible representations of the group U_{2l+1}. Since the representation does not depend upon M_s, the labelling of states by integers $[\lambda_1, \lambda_2, \lambda_3 \ldots \ldots \lambda_{2l+1}]$ is equivalent to the specification of total spin S. Similarly the irreducible representation D_L of R_3 classifies the states according to the total orbital angular momentum L. Labelling of states by quantum numbers L and S is preferred over these groups as they have more direct physical meaning. The irreducible representations of R_7 and G_2 are used for complete specification of the states, though these do not have any direct physical meaning. The irreducible representation of R_7 are characterized by a set of three integers $W = [w_1, w_2, w_3]$ and those of G_2 by a set of two integers $U = (u_1, u_2)$ such that $2 \geq w_1 \geq w_2 \geq w_1 \geq 0$ and $2 \geq u_1 \geq u_2 \geq 0$.

An alternative scheme for labelling (again due to Racah) is through the concept of the seniority number. According to this approach all identical terms S, L of the configuration l^N divide into two classes. The states $SLJJ_z$

belonging to terms of the first category can be obtained from the states of the same type in the configuration 1^{n-2} by the addition of two electrons, forming the closed pair 1^2; L=0, S=0. Terms of the second category cannot be obtained by these means from definite SL terms of the configuration 1^{n-2} and in this sense they appear for the first time in the given configuration.

Some of the SL terms of the configuration 1^{n-2} can be obtained in their turn from definite SL terms of the configuration 1^{n-4} by the addition of closed pair 1^2 and so on.

Continuing this reasoning we arrive at the configuration 1^v in which the term SL is met for the first time in the sense that it cannot be obtained from any definite term of the configuration 1^{v-2} by the addition of the pair $1^2 [\, 00]$. The assignment of the number v, the so called seniority number uniquely determines the whole chain of terms generated by the term SL of configuration 1^v. The classification of the terms through seniority number v is equivalent to labelling by the irreducible representations of R_7. Terms of the configurations f^2 and f^3 classified in this manner are listed in Table III-1 and III-2 respectively.

TABLE III-1

Terms of f^2 Configuration

S. No.	w_1, w_2, w_3	u_1, u_2	Seniority Quantum Number v.	L	Neilson and Koster Notation $(2S+1)L$
1	(110)	(11)	2	P	3P
2	(110)	(10)	2	F	3F
3	(110)	(11)	2	H	3H
4	(000)	(00)	0	S	1S
5	(200)	(20)	2	D	1D
6	(200)	(20)	2	G	1G
7	(200)	(20)	2	I	1I

TABLE III-2

Terms of f^3 Configuration

S. No.	w_1, w_2, w_3	u_1, u_2	Seniority Quantum Number v	L	Neilson and Koster's Notation (2S+1)L
1	(111)	(00)	3	S	4S
2	(111)	(10)	3	F	4F
3	(111)	(20)	3	D	4D
4	(111)	(20)	3	G	4G
5	(111)	(20)	3	I	4I
6	(100)	(10)	1	F	2F1
7	(210)	(11)	3	P	2P
8	(210)	(11)	3	H	2H1
9	(210)	(20)	3	D	2D1
10	(210)	(20)	3	G	2G1
11	(210)	(20)	3	I	2I
12	(210)	(21)	3	D	2D2
13	(210)	(21)	3	F	2F2
14	(210)	(21)	3	G	2G2
15	(210)	(21)	3	H	2H2
16	(210)	(21)	3	K	2K
17	(210)	(21)	3	L	2L

2.3 Choice of Basis States

Corrections to the zeroth order eigenvalues require
the calculation of matrix elements of perturbation Hamil-
tonian. These matrix elements can be calculated by defin-
ing a complete set of basis states in a well defined
coupling scheme. The chosen coupling scheme should be
close to the physical coupling. The choice between diffe-
rent coupling schemes(LS or jj) is influenced by the fact
that which interaction (electrostatic interaction or spin-
orbit interaction) has a decisive value. In the case of
rare earth ions, the relative strengths of these interac-
tions lead to a coupling which is intermediate between the
LS and jj coupling schemes. However, matrix elements can
still be calculated in some known coupling scheme and then
a transformation can be made to the actual physical coupling.
In order to perform the energy calculations in the inter-
mediate coupling scheme, it is necessary to solve the
secular equation composed of the matrix elements of the
perturbation $H'_{Coul} + H'_{so}$. One can choose the central field
wavefunctions Ψ_{CF} as the zeroth approximation functions
or any independent linear combination of these functions.
A judiciously chosen set of basis states can simplify the
calculations a great deal. In particular, one can proceed
from the functions Ψ_{SLJJ_z}. In this case the matrix of the
electrostatic interaction H'_{Coul} is diagonal with respect to

$SLJJ_z$, which substantially simplifies the calculations. Since the matrix of H'_{so} is also diagonal with respect to J, J_z (but not with respect to SL), the secular equation corresponding to the specific values of JJ_z has the form

$$\begin{vmatrix} \langle S_1L_1JJ_z \mid H'_{Coul}+H'_{so} \mid S_1L_1JJ_z \rangle - \epsilon \;\; ; \;\; \langle S_1L_1JJ_z \mid H'_{so} \mid S_2L_2JJ_z \rangle \\ \langle S_2L_2JJ_z \mid H'_{so} \mid S_1L_1JJ_z \rangle \;\; ; \;\; \langle S_2L_2JJ_z \mid H'_{Coul}+H'_{so} \mid S_2L_2JJ_z \rangle - \epsilon \\ \cdots\cdots\cdots\cdots\cdots\cdots\cdots\cdots\cdots\cdots\cdots\cdots\cdots\cdots\cdots \\ \cdots\cdots\cdots\cdots\cdots\cdots\cdots\cdots\cdots\cdots\cdots\cdots\cdots\cdots\cdots \end{vmatrix} = 0$$

$$\cdots (3.16)$$

The roots of this equation ϵ_1 , ϵ_2 , $\epsilon_3 \ldots$ are the required corrections to the energy. Having solved the secular equation, it is possible to find the eigenfunction Ψ_{JJ_z} also .

It should be noted here that the states $\mid SLJJ_z \rangle$ are of composite nature where as the interactions H'_{Coul} and H'_{so} are functions of coordinates of individual electrons and cannot be expressed as function of SL, J and J_z. This would create extra complications by requiring the actual calculations of matrix elements to be carried out in determinantal product states. In order to avoid these complications, Racah developed the tensor operator techniques[7] where one can directly calculate the matrix elements in the composite states $\mid SLJJ_z \rangle$ by suitably transforming the Hamiltonian.

2.4 Coefficient of Fractional Parentage

Group theoretical classification uniquely specifies the states without having to calculate the particular linear combination of the determinantal states but does not extend any help in calculating the matrix elements. Racah introduced the concept of fractional parentage[8] to sort out this problem. The solution of the problem lies in assigning the initial term, usually spoken of as assignment of origin or parentage of the term, to the state $\Psi(1^N\gamma SL)$ of a group 1^n of equivalent electrons.

The state $\langle 1^n\gamma SL|$ of a group 1^n of equivalent electrons can be expanded as a linear combination of the functions $|1^{n-1}[\bar{\gamma}\ \bar{S}\ \bar{L}]\ , 1\rangle$ corresponding to the different initial term $\bar{S}\ \bar{L}$ of the configuration 1^{n-1}. Here, however, it is necessary to take into account the fact that among the states $|1^n[\bar{\gamma}\ \bar{S}\ \bar{L}]\ 1,SL\rangle$ obtained by the general rule of addition of angular momenta there will be some which are forbidden by the Pauli exclusion principle. Any well defined linear combination of functions $|1^{n-1}[\bar{\gamma}\ \bar{S}\ \bar{L}]1, SL\rangle$

$$|1^n r SL\rangle = \sum_{\bar{\gamma}\ \bar{S}\ \bar{L}} G^{SL}_{\bar{\gamma}\ \bar{S}\ \bar{L}}\ |1^{n-1}[\bar{\gamma}\ \bar{S}\ \bar{L}]\ 1, rSL\rangle \tag{3.17}$$

will comply with Pauli principle. The coefficients $G^{SL}_{S'L'}$ are called the fractional parentage coefficients and are denoted by means of $|1^{n-1}[\bar{\gamma}\ \bar{S}\ \bar{L}]\ 1;\ SL\}1^n\gamma SL\rangle$ following

Racah. General method for the calculation of these coeffi-
cients has been developed by Racah. These coefficients
have been tabulated by Neilson and Koster[8] for all equi-
valent electron configurations.

2.5 Tensor Operators and Matrix Elements

In calculating the matrix elements of various
operators it is advisable to classify these operators
according to their behaviour on rotation of the system
of coordinates. From this point of view the usual defini-
tion of tensor in the Cartisean system of coordinates is
unsuitable for the reason that from the components of a
tensor of rank $k = 2$ a number of linear combinations can
be formed which behave differently on rotation of the
coordinate system. The need naturally arises for a defi-
nition of a tensor for which all its components and any
linear combination of these components are transformed
in the same way on rotation of coordinate system. This
condition is satisfied by the $(2k+1)$ spherical harmonics
Y_{kq} ; $q = k, k-1, \ldots\ldots k$. We shall therefore, define
a tensor of rank k as a set of $(2k+1)$ quantities which
transform as spherical harmonics Y_{kq} on rotation of coor-
dinate system. The tensors defined in this way are called
spherical tensors or irreducible tensors. In accordance,
with this definition the irreducible tensor T_k of rank k
is a set of $(2k+1)$ operators T_{kq} , $q = k, k-1 \ldots\ldots -k$

obeying the same commutation relations with the angular momentum of the system J as Y_{kq}. These commutation relations[7] have the form

$$[(J_x \pm iJ_y), T_q^{(k)}] = \sqrt{(k \mp q)(k \pm q + 1)}\ T_{q\pm 1}^{(k)} \qquad (3.18)$$

and

$$[J_z, T_q^{(k)}] = qT_q^{(k)} \qquad (3.19)$$

Matrix elements of $T_q^{(k)}$ in the JM representation are given by the Wigner-Eckart theorem

$$< \gamma JM|T_q^{(k)}|\gamma'J'M'> = (-1)^{J-M} < \gamma J ||T^{(k)}||\ \gamma'J'> \times \begin{pmatrix} J & k & J' \\ -M & q & M' \end{pmatrix}$$

$$.. \ (3.20)$$

The factor $< \gamma J|| T^k || \gamma'J'>$ not dependent on MM' and q, are called the reduced matrix elements. Another type of tensor operator $X_q^{(K)}$ which will be required for the calculation of matrix elements of perturbation Hamiltonian is the tensor product of two irreducible tensor operators $T^{(k_1)}$ and $U^{(k_2)}$. The tensor product of two tensor operators $T^{(k_1)}$ and $U^{(k_2)}$ is defined as below :

$$X_q^{(K)} = \sum_{\nu, \lambda} <k_1 k_2 \nu \lambda | k_1 k_2 kq>\ T_\nu^{(k_1)}\ U_\lambda^{(k_2)} \qquad (3.21)$$

where $<k_1 k_2 \nu \lambda | k_1 k_2 kq>$ are C.G. coefficients, and is represented as

$$X_q^{(K)} = \left[T^{(k_1)} \times U^{(k_2)}\right]_q^K \qquad (3.22)$$

With the aid of eqn. (3.21) one can construct $(2k_1+1)$, if $k_1 \leq k_2$ or $(2k_2+1)$ if $k_2 > k_1$, of operators $\left[T^{(k_1)} \times U^{(k_2)}\right]$. If $k_1 = k_2 = k$ then among the possible values of K there is K = 0. Thus from two tensors of the same rank one can construct a scalar

$$\left[T^{(k)} \times U^{(k)}\right]^0_0 = \sum_q \langle kk\nu -\nu \mid kk00\rangle \; T^k_\nu \, U^k_{-\nu}$$

$$= \frac{(-1)^k}{(2k+1)} \sum_\nu (-1)^\nu \; T^k_{-\nu} \, U^k_{-\nu} \qquad (3.23)$$

one can put this scalar in a more convenient form

$$(T^k U^k) = \sum_\nu (-1)^\nu \, T^k_\nu \, U^k_{-\nu} = \sum_\nu (-1)^\nu \, T^k_{-\nu} U^k_\nu \qquad (3.24)$$

Expression (3.24) is called the scalar product of the two tensor operators. Two examples of such operators are H'_{Coul} and H'_{so} (both are scalars i.e. $k = \nu = 0$). A typical matrix element for the scalar product of tensor operators is given by

$$\langle \gamma J_1 J_2 J J_z \mid T^{(k)} U^{(k)} \mid \gamma J'_1 J'_2 J' J'_z\rangle$$

$$= \delta(J,J') \cdot \delta(J_z, J'_z) \times (-1)^{J'_1 + J_2 + J}$$

$$\times \begin{Bmatrix} J'_1 & J'_2 & J \\ J_2 & J_1 & k \end{Bmatrix} \times \sum_{\gamma} \langle \gamma J_1 \mid\mid T^k \mid\mid \gamma'' J'_1 \rangle$$

$$\times \langle \gamma'' J_2 \mid\mid U^k \mid\mid \gamma' J'_2 \rangle \qquad (3.25)$$

where the quantum numbers J_1 and J_2 refer to operators

$T^{(k)}$ and $U^{(k)}$ respectively and J to the composite system.

The quantity $\begin{Bmatrix} J_1' & J_2 & J \\ J_2 & J_1 & k \end{Bmatrix}$ is called the Winger's 6-j symbols.

Both 3-j and 6-j symbols have been tabulated by Rotenberg[9].

In what follows now we will outline the evaluation of matrix

elements of various interactions.

2.6 Matrix Elements of the Electrostatic Interaction

The tensor operator for this interaction can be

obtained by transforming the expression for the energy of

the interaction e^2/r_{ij} in such a way as to separate the

radial and angular variables. We shall use the fact that

$1/r_{ij}$ can be expanded in a series of Legendre polynomials

$$(r_i^2 + r_j^2 - 2r_i r_j \cos\omega)^{-1/2} = \sum_{k=0} \frac{r_<^k}{r_>^{k+1}} P_k(\cos\omega) \qquad (3.26)$$

Here the smaller and greater of the magnitudes of the

vector r_i and r_j are denoted by $r_<$ and $r_>$; and ω is the

angle between the vectors r_i and r_j i.e. between the direc-

tions $\theta_i \phi_i$ and $\theta_j \phi_j$. By using the theorem for the addi-

tion of spherical functions, $P_k(\cos\omega)$ can be expressed in

terms of spherical harmonics $Y_{kq}(\theta_i, \phi_i)$ and $Y_{kq}(\theta_j, \phi_j)$

Thus

$$e^2/r_{ij} = e^2 \sum_{k=0} \frac{4}{(2k+1)} \frac{r_<^k}{r_>^{k+1}} \sum_q Y_{kq}^*(\theta_i \phi_i) Y_{kq}(\theta_j \phi_j) \qquad (3.27)$$

$$= e^2 \sum_k \frac{r_<^k}{r_>^{k+1}} \sum_{q=-k}^{k} (-1)^q (C_{-q}^{(k)})_i (C_q^{(k)})_j$$

$$= e^2 \sum_k \frac{r_<^k}{r_>^{k+1}} (C_i^{(k)} \cdot C_j^{(k)}) \qquad (3.28)$$

where

$$C_q^{(k)} = \sqrt{\frac{4\pi}{2k+1}} \; Y_{kq} \qquad\qquad (3.29)$$

Thus the matrix elements for e.s. interaction in $|UWSL>$ basis can be calculated by using expression (3.25) for the scalar product of two tensor operators. Each matrix element can be expressed as a linear combination of Slater integrals

$$E = <(nf)^N \; UWSL \; | \; H_1 | \; (nf)^N \; U'W'S'L'>$$

$$= \sum_k f_k <(nf)^N \; UWSL, \; (nf)^N \; U'W'S'L'> \; \times \; F^k(nf, \; nf)$$

$$= \sum_k f_k <(nf)^N \; UWSL, \; (nf)^N \; U'W'S'L'> \; \times \; F^k(nf, \; nf)$$

$$\qquad\qquad\qquad\qquad\qquad\qquad .. \;\; (3.30)$$

For a two electron configuration

$$F^{(k)} = F_k D_k = e^2 \int_0^\infty \int_0^\infty \frac{r_<^k}{r_>^{k+1}} \left[R_{nf}(r_i) \; R_{nf}(r_j) \right]^2 \; dr_i dr_j \qquad .. \;\; (3.31)$$

and

$$f_k = f^k/D_k = <f^2 SL \; | \; C_i^{(k)} . C_j^{(k)} | \; f^2 S'L'>$$

$$= \delta(S,S')\delta(L,L')(-1)^L \begin{Bmatrix} 3 & 3 & k \\ 3 & 3 & L \end{Bmatrix} \left[<3||C^k||\, 3> \right] \qquad .. \;\; (3.32)$$

where the typical reduced matrix element $< 1 \; ||C^{(k)}|| \; 1'>$ is expressed as

$$< 1 \; ||C^k||\; 1' > = (-1)^1 \sqrt{(21+1)(21'+1)} \begin{pmatrix} 1 & k & 1' \\ 0 & 0 & 0 \end{pmatrix} \qquad (3.33)$$

Making use of the properties of 3-j symbols, this matrix element will be nonzero only if the triangular condition

$\Delta(1,1',k)$ is fulfilled and

$$(k + 1 + 1') = 2g \tag{3.34}$$

where g is an integer. From these considerations only nonzero terms in the expansion (3.30) are with k even and $k \leq 6$. Numerical quantities D_k are listed in Table 1[6] and 2[6] of reference (10). The operator $[c_i^{(k)} \cdot c_j^{(k)}]$ is invariant under the operation of R_3 but does not have the transformation properties of the groups R_7 and G_2. Thereby it makes the task of calculating its matrix elements in the states $|f^N UWSL\rangle$, for systems having more than two f electrons, more difficult. However, a linear combination can be found which will satisfy these requirements. A matrix element for such a system may then be expressed in terms of the new operators

$$E = \sum_{k=0}^{3} e_k E^k \tag{3.35}$$

Radial parts E^k's can be expressed as the linear combinations of F^k's

$$E^0 = (F_0 - 10F_2 - 33F_4 - 286F_6)$$

$$E^1 = (70F_2 + 231F_4 + 2002F_6)/9$$

$$E^2 = (F_2 - 3F_4 + 7F_6)/9 \tag{3.36}$$

$$E^3 = (5F_2 + 6F_4 - 91F_6)/3$$

While the angular parts e_k's in terms of f^k's have the following relations

$$e_0 = f^0 = N(N-1)$$

$$e_1 = 9f^0/7 + f^2/42 + f^4/77 + f^6/462$$

$$e_2 = 143 f^2/42 - 130f^4/77 + 35f^6/462 \qquad (3.37)$$

$$e_3 = 11f^2/42 + 4f^4/77 - 7f^6/462$$

Neilson and Koster[11] have tabulated these angular parts for all the f^N configurations.

2.7 Spin-orbit Interaction

The spin-orbit interaction operator H'^{SO} which is already in tensorial form mixes the states of same JJ_z but differing γSL quantum numbers. A typical matrix element of this operator in the $|f^N \gamma SL JJ_z>$ bases has the form :

$$< f^N \gamma SLJJ_z |H'| f^N \gamma'S'L'J'J'_z >$$

$$= \zeta_{nf} \delta(J,J') \delta(J_z, J'_z)$$

$$(-1)^{S'+L+J} \times [1(1+1)(21+1)]^{1/2} \times < f^N \gamma SL||V''||f^N \gamma'S'L'>$$

$$\times \begin{Bmatrix} S & S' & 1 \\ L' & L & L & J \end{Bmatrix} \qquad (3.38)$$

where

$$\zeta_{nf} = \int_0^{\infty} R_{nf}^2(r) \xi(r) dr \qquad (3.39)$$

and
$$\xi(r) = (\hbar^2/2m^2c^2)\frac{1}{r}\frac{dU(r)}{dr} \tag{3.40}$$

and

$$\langle f^N WUSL \mid\mid V'' \mid\mid f^N W'U'S'L' \rangle = 3N([S,S',L,L'])^{1/2}$$

$$x \quad (-1)^{1/2+1+S+L} x \quad x \quad \sum_\Psi \langle \Psi \{ \mid \Psi \rangle \langle \Psi \{ \mid \Psi \rangle$$

$$x \quad \begin{Bmatrix} S & 1 & S' \\ 1/2 & \bar{S} & 1/2 \end{Bmatrix} \quad x \quad \begin{Bmatrix} L & 1 & L' \\ 1 & \bar{L} & 1 \end{Bmatrix} \tag{3.41}$$

where $\langle \Psi \{ \mid \Psi \rangle$ are coefficients of fractional parentage. Matrix elements for $V^{(11)}$ for all f^N configurations are given in ref. (8). The triangular conditions of 6-j symbols give the following selection rules for the spin-orbit interaction

$$\Delta S = 0, \pm 1$$
$$\Delta L = 0, \pm 1 \tag{3.42}$$

2.8 Configuration Interactions

Perturbation calculations of combined electrostatic and spin-orbit interactions performed in the single configuration approximation for the energy levels of a particular configuration lead to large deviations (of the order of several hundred wave numbers) from the experimentally inferred energy levels, even though the radial integrals are treated as adjustable parameters.

The deficiencies of single configuration approximation can be overcome by including the effects of interacting

configurations. Configuration interaction plays a very important role in the electronic properties of rare earths, which sometimes has profound effect on their hyperfine-structure[12], intensity and their behaviour in the crystal fields[13]. If one has to include all the configuration interactions, the size of energy matrices will increase to unmanageable extent. So the approach[14] for the consideration of these interactions would be to keep the size of the matrices fixed and add to it the perturbation of neighbouring configurations. Rajank and Wybourne treated this problem for 1^N type configuration using second order perturbation theory.

The following configurations can interact with 1^N type configuration :

(1) $1^{N-2}1''^2$ and $1^{N-2}1'1''$

(2) $1'^{41'}1^{N+2}$ and $1''^{41''+1}1^{N+2}$

(3) $1'^{41+1}1^N1''$

(4) $1^{N-1}1'$

(5) $1'^{41'+1}1^{N+1}$

First three of these interact through core excitation. These interactions do not affect the structure of the configuration and hence may be excluded. Effect of the remaining two interactions may be accounted by adding to each of the electrostatic interaction matrix elements (3.35)

the quantity

$$C(\Psi, \Psi') = \frac{\sum_\tau \langle 1^N \Psi \mid G \mid m_\tau \rangle \langle m_\tau \mid G \mid 1^N \Psi' \rangle}{E_\tau} \quad (3.43)$$

where the state m_τ belongs to the interacting configuration separated from 1^N configuration by energy gap E_τ. Rajanak and Wybourne expressed this term in the form

$$C(\Psi, \Psi') = \sum_{k=0}^{21} P^k \langle f^N \Psi \mid \sum_{i>j}^N U_i^{(k)} \cdot U_j^{(k)} \mid f^N \Psi' \rangle \quad (3.44)$$

where U^k's are the normalized unit tensor operators and P^k includes the radial parts of the matrix elements and the excitation energies. For even k the matrix-elements resemble the electrostatic interaction and hence this part is automatically included by the adjustable parameters F^k's. For odd k the contribution of the interacting configurations is :

$$\delta(\Psi, \Psi') \left[\alpha(\alpha+1) + \beta G(G_2) + \gamma G(R_7) \right] \quad (3.45)$$

where $G(G_2)$ and $G(R_7)$ are the eigenvalues of Casimir's operator[10] for the groups G_2 and R_7 respectively. Angular parts of the expression (3.45) resembles those of the following expression for orbit-orbit interaction[15] H'_{0-0} but the radial parts of these two expressions have the opposite sign.

$$< f^N \tau SLJ \mid H'_{0-0} \mid f^N \tau' S'L'J' > = - \delta(\tau, \tau') \delta(J,J')$$

$$x \quad \delta(S,S') \; \delta(L,L') \; x \; [\alpha L(L+1) + \beta G(G_2) + \gamma \, G(R_7) + N\omega]$$

$$.. \quad (3.46)$$

where

$$\alpha = -2(M^0 - 5M^4/121); \quad \beta = 32(M^2 - 35M^4/121)$$

$$\gamma = -40M^2 ; \quad \text{and} \quad \omega = 8(3M^0 + M^2 + 5M^4/11)$$

and

$$M^X = \frac{\alpha^2}{4} \int \int_{r_i > r_j} R^2_{nf}(r_i) \, R^2_{nf}(r_j) \frac{r_i^X}{r_j^{x+3}} \, dr_i \cdot dr_j \quad .. \quad (3.47)$$

is a radial integral defined by Marvin[16] Hence in the
parameterization of the effects of configuration interac-
tion due to two electron excitations, the effects of the
orbit-orbit interaction will be accommodated in the derived
parameters. Wybourne[17] has generalised the configuration
interaction to higher order of perturbation which includes
more number of parameters. Such effects were not included
here as relatively small number of levels is available for
the optimization of the parameters.

3. CRYSTAL-FIELD INTERACTION

When a free ion is embedded in the crystal, its
spherical symmetry is destroyed and each level which is
(2J+1) fold degenerate will split due to the electric
field of crystalline environment possessing a well defined

symmetry. The degree to which the degeneracy is removed depends upon the point symmetry at the ion site. According to Kramer's theorem[18] the degeneracy can be completely lifted by crystal field of low enough symmetry in case of even electron system but for the odd electron system two fold degeneracy persists which can not be removed without the application of magnetic interaction.

Hamiltonian for an ion in the crystal field can be expressed as

$$H = H_F + H'_{cry} \qquad (3.48)$$

where H_F is free ion Hamiltonian and H'_{cry} represents the interaction of free ion with its environment. As we have already pointed out that rare earth ions interact weakly with their environment, H'_{cry} can be treated as small perturbation to the free ion Hamiltonian. Since the free ion possess the spherical symmetry, it would be advantageous to expand the crystal field in terms of the spherical tensor operators. Thus

$$H'_{cry} = \sum_{k,q,i} B_q^k (C_q^k)_i \qquad (3.49)$$

where the summation runs over all the electrons of the ion. Quantities $B_q^{(k)}$ form the set of expansion coefficients and will be treated as the adjustable parameters. For H'_{cry}

to be a Hermitian operator

$$B_q^k = (-1)^q \, B_q^{k \, *} \qquad\qquad (3.50)$$

The first term in the expansion with $k = q = 0$, is sphe-rically symmetric. In the first approximation, it would shift the configuration as a whole and may be neglected as far as the crystal field splittings of levels are concerned.

For f^N electrons only nonzero terms in the expan-stion (3.49) are with $k \leq 6$ for the reasons similar to the one discussed in the case of electrostatic interac-tion. Symmetry operation S_4 can be expressed by the following transformation

$$\begin{pmatrix} X \\ Y \\ Z \end{pmatrix} \longrightarrow \begin{pmatrix} X \\ -Y \\ -Z \end{pmatrix} \qquad\qquad (3.51)$$

Using this transformation and the Cartisian representation of the spherical harmonics, it can be shown readily that the relevant terms in the expansion (3.49) are

$$H'_{cry}(S_4) = B_0^2 \, C_0^{(2)} + B_0^4 \, C_0^{(4)} + B_0^{(6)} \, C_0^{(6)}$$

$$+ \sum_{k=4,6} [B_4^{(k)} (C_4^{(k)} + C_{-4}^{(k)}) + iB_4'^{\,k}(C_4^{(k)} - C_{-4}^k)]$$

$$\qquad\qquad\qquad\qquad \dots\; (3.52)$$

We have neglected here the odd terms as their matrix elements among states with the same parity (i.e. states arising from the same configuration) will be zero. From the properties of spherical harmonics, operators $(C_4^{(k)} + C_{-4}^{(k)})$ are real. Thereby their coefficients $B_4^{(k)}$ will also be real. On the other hand, operators $(C_4^{(k)} - C_{-4}^{(k)})$ are imaginary. To make H'_{cry} to be Hermitian "i" has been introduced explicitly so that $B_4'^{(k)}$ are real.

Quantities $B_q^{(k)}$ have been calculated in the past using point charge model[19-22] and other methods e.g. LCAO-MO for some host materials with little success. Newman and coworkers[21] have evaluated $B_q^{(k)}$'s for LaCl$_3$ and Garnets taking into account the overlap, covalency and exchange effects. Their results for $B_q^{(k)}$ with k = 4 and 6 are in good agreement with the empirical results. Due to lack of such calculations for other hosts, it is customary to treat them as adjustable parameters. In this treatment one needs the starting values of B_q^k which can be obtained from the point charge model. In this model, the B_q^k's can be expressed as

$$B_q^k = \rho_k \, A_q^k \qquad\qquad (3.53)$$

where A_q^k are irreducibel tensor components of the electro-static crystal field calculated from the point charge lattice sums and are ion independent, host dependent.

ρ_k are ion dependent and host independent quantities expressed as

$$\rho_k = \langle r^k \rangle_{HF} (1 - \sigma_k) / \tau^k \qquad (3.54)$$

where $\langle r^k \rangle_{HF}$ are Hartreefock expectation values given by Freeman and Watson[3] and σ_k are the linear screening factors[6]. τ is a scaling factor introduced to account for the inadequacy of Hartreefock wavefunctions and the expansion of free ion wavefunctions when the ion is embedded in the crystal. Values of ρ_k for all lanthanides are listed in Table II of reference (25). If the parameters B_q^k are known for some lanthanide ion in a given host, the host dependent part A_q^k can be determined using the values of ρ_k for this ion. Thus one can obtain the starting values of B_q^k for any other lanthanide ion in this host using the values of A_q^k and ρ_k.

3.1 Choice of Basis States

Since H'_{cry} does not commute with J and J_z, its effect is to mix states with different J and J_z. As a result, J and J_z cease to be good quantum numbers. However, one can find linear combinations of $| f^N J J_z \rangle$ states which will transform according to the irreducible representations of the point group under consideration. These irreducible representations can then

be used for labelling these basis states $|f^N J J_z \Gamma_i\rangle$

where Γ_i is the irreducible representation. Table III.3

gives the character table and bases functions for the

group S_4. For the case of half integral J values (odd

electron systems e.g. Nd^{3+}) one needs to work with double

groups of S_4. Multiplication table for S_4 is given in

Table III.4. Table III.5 describes the correlation

among the irreducible representations of full rotation

group and those of 'S_4' group (for Pr^{3+}) and 'double

group S_4'(for Nd^{3+}). From the comptability tables we

see that Γ_3 and Γ_4 are degenerate for the integral J

values and for half integral J values, $\Gamma_5 (\Gamma_7)$ and

$\Gamma_6 (\Gamma_8)$ are degenerate representations. For the crystal

field calculations one needs to choose only one out of

these degenerate representations. Thus, for Pr^{3+} ion

we will use only Γ_3 and for Nd^{3+} we will choose Γ_6

and Γ_7.

In order to construct the linear combinations

of J_z having proper transformation properties, concept

of projection operator[27] is used. Projection operator

$P_k^{(i)}$ defined for any group G when operates on a set of

functions $|JJ_z\rangle$ selects those functions which transform

according to the kth row of the ith irreducible repre-

sentation of group G. For the group S_{2n} and configura-

tion of parity p

TABLE III-3

Character Table and Basis Function for S_4

S_4	E	$\bar{E}$	S_4^{-1}	$\bar{S}_4^{-1}$	C_2	$\bar{C}_2$	S_4	$\bar{S}_4$	Time Inv.	Bases
Γ_1	1	1	1	1	1	1	1	1	a	S_z
Γ_2	1	1	-1	-1	1	1	-1	-1	a	z or xy
Γ_3	1	1	i	i	-1	-1	-i	-i	b	$-(S_x + iS_y)$ or $i(x - iy)$
Γ_4	1	1	-i	-i	-1	-1	i	i	b	$(S_x - iS_y)$ or $-i(x + iy)$
Γ_5	1	-1	ω^*	$-\omega$	i	-i	$-\omega^3$	ω	b	$\Phi(1/2 , 1/2)$
Γ_6	1	-1	$-\omega^3$	ω^3	-i	i	ω	$-\omega^3$	b	$\overline{\Phi}(1/2, -1/2)$
Γ_7	1	-1	$-\omega$	ω	i	-i	ω^3	$-\omega$	b	$\Phi(3/2, -3/2)$
Γ_8	1	-1	ω^3	$-\omega^3$	-i	i	$-\omega$	ω^3	b	$\overline{\Phi}(3/2, 3/2)$

a or b in this column indicates whether or not $\Gamma(R) = \Gamma(R)^*$ for the corresponding representation.

* $\omega = \exp(\pi i/4)$

TABLE III-4

Multiplication Table for S_4

Γ_1	Γ_2	Γ_3	Γ_4	Γ_5	Γ_6	Γ_7	Γ_8	
Γ_1	Γ_2	Γ_3	Γ_4	Γ_5	Γ_6	Γ_7	Γ_8	Γ_1
	Γ_1	Γ_4	Γ_3	Γ_7	Γ_8	Γ_5	Γ_6	Γ_2
		Γ_2	Γ_1	Γ_8	Γ_5	Γ_6	Γ_7	Γ_3
			Γ_2	Γ_6	Γ_7	Γ_8	Γ_5	Γ_4
				Γ_3	Γ_1	Γ_4	Γ_2	Γ_5
					Γ_4	Γ_2	Γ_3	Γ_6
						Γ_3	Γ_1	Γ_7
							Γ_4	Γ_8

TABLE III-5

Full Rotation Group Compatability Table for S_4

D_0^+ Γ_1

D_1^+ $\Gamma_1 + (\Gamma_3 + \Gamma_4)$

D_2^+ $\Gamma_1 + 2\Gamma_2 + (\Gamma_3 + \Gamma_4)$

D_3^+ $\Gamma_1 + 2\Gamma_2 + 2(\Gamma_3 + \Gamma_4)$

D_4^+ $3\Gamma_1 + 2\Gamma_2 + 2(\Gamma_3 + \Gamma_4)$

D_5^+ $3\Gamma_1 + 2\Gamma_2 + 3(\Gamma_3 + \Gamma_4)$

D_6^+ $3\Gamma_1 + 4\Gamma_2 + 3(\Gamma_3 + \Gamma_4)$

$D_{1/2}^-$ $\Gamma_7 + \Gamma_8$

$D_{3/2}^-$ $\Gamma_5 + \Gamma_6 + \Gamma_7 + \Gamma_8$

$D_{5/2}^-$ $2\Gamma_5 + 2\Gamma_6 + \Gamma_7 + \Gamma_8$

$D_{7/2}^-$ $2\Gamma_5 + 2\Gamma_6 + 2\Gamma_7 + 2\Gamma_8$

$D_{9/2}^-$ $2\Gamma_5 + 2\Gamma_6 + 3\Gamma_7 + 3\Gamma_8$

$D_{11/2}^-$ $3\Gamma_5 + 3\Gamma_6 + 3\Gamma_7 + 3\Gamma_8$

$D_{13/2}^-$ $4\Gamma_5 + 4\Gamma_6 + 3\Gamma_7 + 3\Gamma_8$

$D_{15/2}^-$ $4\Gamma_5 + 4\Gamma_6 + 4\Gamma_7 + 4\Gamma_8$

$D_{17/2}^-$ $4\Gamma_5 + 4\Gamma_6 + 5\Gamma_7 + 5\Gamma_8$

+ or − sign indicates even or odd parity relevant to a particular configuration (e.g. $4f^2$ − even parity and $4f^3$ odd parity).

$$P_k^{(i)} \mid J\ J_z> \ = \ \mid J\ J_z> \quad \delta(J_z\ ,\ \mu(i,k)\ +\ n\ \sigma(p)\ \pm\ 2nm)$$

$$\dots (3.55)$$

where for p : odd ($4f^3$ configuration)

$$\sigma\ =\ 1 \text{ and for p : even } (4f^2 \text{ configuration})$$

$$\sigma\ =\ 0\ ;$$

$$m\ =\ 0,\ \pm 1,\ \pm 2,\ \pm 3$$

$$\left.\right\}\dots(3.56)$$

For S_4 , n = 2

k = 1 for all irreducible representations of S_4.

$$\mu(i,1)\ =\ 0\ ,\ 2 \text{ for } i = 1,2$$

$$=\ \pm \text{ for } i = 3,4$$

$$=\ \pm \text{ for } i = 5,6$$

$$=\ \pm 3/2 \text{ for } i = 7,8$$

$$\left.\right\}(3.57)$$

Table III-6 and III-7 lists the basis functions for the irreducible representations of group 'S_4' and 'double group S_4'.

3.2 Matrix Elements of H'_{cry}

A typical matrix element of the operator H'_{cry} is given by

$$< f^N \gamma SLJJ_z \mid H'_{cry} \mid f^N \gamma'S'L'J'J_z'>$$

$$=\ \sum_{k,q}\ B_q^k\ < f^N \gamma SLJJ_z \mid U_q^{(k)} \mid f^N \gamma'S'L'J'J_z'>$$

$$(3.58)$$

$$x\ < f \mid\mid C^{(k)} \mid\mid f>\ x\ \delta(S,S')$$

where $U_q^{(k)}$ are the unit tensor operators and are defined as below

$$U^{(k)} = \sum_{i=1}^{N} u_i^{(k)} \qquad (3.59)$$

It is through eqn. (3.59) that the summation over f electrons in eq. (3.58) is taken care of. Using eqns. (3.20) and (3.25) we canwrite

$$< f^N \; \gamma \, SLJJ_z | \; U_q^{(k)} | \; f^N \; \gamma ' S'L'J'J_z' >$$

$$= (-1)^{J-J_z} \times \begin{pmatrix} J & k & J' \\ -J_z' & q & J_z \end{pmatrix} \times (-1)^{S+L'+J+k}$$

$$\times \begin{Bmatrix} J & J' & k \\ L' & L & S \end{Bmatrix} \times < f^N \; \gamma SL \; ||U^{(k)}|| \; f^N \; \gamma 'S'L' >$$

$$\ldots (3.60)$$

Reduced matrix elements for $U^{(k)}$ are listed by Neilson and Koster[8]. In eqn. (3.60) the axial term $U_0^{(k)}$ will split levels differing in J_z and $U_q^{(k)}$ terms will mix the states for which $J_z - J_z' = q$. Due to this mixing J and J_z will cease to be good quantum numbers. Though, the odd terms in crystal field potential do not contribute to the energies still they play a very important role by mixing the configurations of opposite parity. Thereby it allows the electric dipole transitions.

Diagonalization of the crystal field energy matrices give the energy eigenvalues and crystal field eigenvectors. The above procedure is general enough to be

TABLE III-6

Basis Function for S_4 Irreducible Representation : $4f^2$ Configuration

J	1		2		3		No. of Stark Components
	J_z	A	J_z	B	J_z	C	
0	0	1					1
1	0	1			1	1	2
2	0	1	±2	2	1	1	4
3	0	1	±2	2	1,$-$3	2	5
4	0,±4	3	±2	2	1,$-$3	2	7
5	0,±4	3	±2	2	1,$-$3,5	3	8
6	0,±4	3	$\pm2,\pm6$	4	1,$-$3,5	3	10

TABLE III-7

Basis Functions for S_4 Irreducible
Representation : $4f^3$ Configuration

J	6			7		No. of Stark Components
	J_z		A	J_z	B	
1/2			0	1/2	1	1
3/2	3/2		1	1/2	1	2
5/2	3/2,-5/2		2	1/2	1	3
7/2	3/2,-5/2		2	1/2,-7/2	2	4
9/2	3/2,-5/2		2	1/2,-7/2,9/2	3	5
11/2	3/2,-5/2,11/2		3	1/2,-7/2,9/2	3	6
13/2	3/2,-5/2,11/2,-13/2		4	1/2,-7/2,9/2	3	7
15/2	3/2,-5/2,11/2,-13/2		4	1/2,-7/2,9/2,-15/2	4	8
17/2	3/2,-5/2,11/2,-13/2		4	1/2,-7/2,9/2,-15/2,17/2	5	9

TABLE III-8

Electric Dipole Selection Rules for $4f^2$
Configuration in S_4 Symmetry

	Γ_1	Γ_2	Γ_3	Γ_4
Γ_1	x	π	σ	σ
Γ_2	π	x	σ	σ
Γ_3	σ	σ	π	x
Γ_4	σ	σ	x	π

TABLE III-9

Electric Dipole Selection Rules for
$4f^3$ Configuration in S_4 Symmetry

	Γ_5	Γ_6	Γ_7	Γ_8
Γ_5	σ	x	σ	π
Γ_6	x	σ	π	σ
Γ_7	σ	π	σ	x
Γ_8	π	σ	x	σ

applicable in the approximation of no J-J mixing as well as when J-J mixing is included. The details of actual calculations and programming of the matrix elements are given in Appendix III.

3.3 Selection Rules for Electric Dipole Transitions in S_4 Symmetry

It is evident from the character table for the group S_4 that the Z- component of the electric dipole operator, which is proportional to Z, transforms as Γ_1 and $-i(x + iy)$ component as Γ_3. This together with the multiplication table for the group S_4 gives rise to the selection rules for the electric dipole transitions.

Table III-8 and III-9 describe these selection rules for the configuration $4f^2(Pr^{3+})$ and $4f^3(Nd^{3+})$ respectively.

4. RAMAN SCATTERING

Light can interact with matter in various ways. It can either be absorbed, emitted or scattered. Scattering of a photon from atoms or molecules may be elastic (Rayleigh scattering) or inelastic. The intensity of Rayleigh scattered light is proportional to the fourth power of the photon's frequency. Raman scattering,

an example of inelastic scattering was first predicted theoretically by Smeckel[28] in 1923. Experimentally it was first observed by Sir C.V. Raman[29] in 1928. Inelastic collisions may cause a molecule or atom to undergo a quantum transition to a higher energy level with the result that photon looses energy and is scattered with lower energy. If the molecule or atom is already in the excited state, interaction with photon may cause it to undergo a transition to lower energy as a result the photon is scattered with increased frequency. The phenomenon in the former case is known as Stokes Raman scattering and in the later case as antiStokes Raman scattering. In case of Stokes Raman Scattering, a photon of frequency $\nu_s = \nu_e - \nu_{xg}$ is created, while one photon of frequency ν_e is annihilated resulting in the excitation of molecule from level g to level x where ν_{xg} is frequency corresponding to the energy gap between the levels x and g. Similarly, in the other process a photon of frequency $\nu_{as} = \nu_e + \nu_{xg}$ is created along with the annihilation of a photon ν_e resulting in the deexcitation of the molecule from level x to level g. Thus a pattern of shifted frequencies ($\Delta\nu$) relative to the primary frequency of the incident radiation is observed in the spectrum of scattered light. These frequency shifts - called Raman shifts -

are equivalent to the energy changes involved in the transitions of scattering sample and are therefore characteristic of it. The Stokes lines are more intense than their antiStokes counterpart.

The theoretical treatment of Raman scattering considers the perturbation of the scattering molecule by the electric field of the incident light. The electric dipole moment matrix element associated with the transition between the initial state $|n>$ and final state $|m>$ is given by :

$$P_{nm} = \int \Psi_m^* P \Psi_n \, d\tau \qquad (3.61)$$

where Ψ_n and Ψ_m are the time independent wavefunctions of the states, P is the induced dipole moment due to the electric vector of the incident radiation and the integral is extended over the whole range of coordinates. The induced dipole moments P is expressed as below

$$\vec{P} = \alpha \vec{E} \qquad (3.6)$$

where α is the polarizability, in general a second rank tensor, E is the electric field of the incident radiation.

The matrix element P_{nm} can be written as :

$$P_{nm} = 2 < m | \bar{P} | n > \cos 2\pi \nu_{mn} t$$

$$+ \sum_j \left| \frac{\nu_{mj}}{\nu_{mj} + \nu} - \frac{\nu_{jn}}{\nu_{jn} - \nu} \right| < m | \bar{P} | j > < j | \bar{P} | n >$$

$$\times \frac{\bar{E}}{h\nu} \sin 2\pi (\nu + \nu_{mn}) t + \sum_j \left| \frac{\nu_{nj}}{\nu_{nj} + \nu} - \frac{\nu_{jm}}{\nu_{jm} - \nu} \right|$$

$$\times < m | \bar{P} | j > < j | \bar{P} | n > \cdot \frac{\bar{E}}{h\nu} \sin 2\pi (\nu - \nu_{mn}) t$$

$$\dots (3.63)$$

where $\bar{E}$ is the incident electromagnetic field and ν its frequency. The quantities $< m | \bar{P} | j >$, and so on, are the matrix elements of $\bar{P} = e(x\bar{i} + y\bar{j} + z\bar{k})$ between the various eigen states of the molecule. The ν_{mj}, ν_{mn}, ν_{jn} the frequencies of transition between the states given by the subscripted letters. It can be seen here that P_{nm} contains frequency components which are the sum and difference of the perturbing and molecular vibrational frequencies. The summation over j implies that all of the possible vibrational, rotational and electronic states of the molecule may contribute to P_{nm}. It can be seen here that when ν, the frequency of the perturbing field approaches one of the ν_{jn}, P_{nm} will become very large.

The energy radiated per second by a system when perturbed by the electromagnetic field, into a Raman transition is given by

$$I = \frac{64 \pi^4}{3e^2} (\nu \pm \nu_{mn})^4 |P_{nm}|^2 \qquad (3.64)$$

The ratio of antiStokes to Stokes intensity for a given band is

$$\frac{I_{as}}{I_s} = \left| \frac{\nu + \nu_{mn}}{\nu - \nu_{mn}} \right|^4 e^{-\nu_{mn}/kT} \qquad (3.65)$$

4.1 <u>Vibrational Spectra of Crystals</u>

The dynamics of a molecule consisting of N atoms can be described in terms of 3N degrees of freedom[30,31] (3-translational + 3-rotational +(3N - 6) vibrational for a nonlinear molecule or 3-translational + 2-rotational + (3N - 5) vibrational for a linear molecule. However, when such a molecule is fixed in the lattice its spectra differs from that of a free-molecule in two ways. Firstly, the selection rules which operate are affected by the crystal symmetry as well as by the molecular symmetry. Secondly, the mode frequencies are modified. Sometimes it is possible to divide the modes into two groups - external and internal. Thus the discussion of vibrational spectra of crystals should deal with the determination of

selection rules for both the internal and external vibrations as well as with the criteria to distinguish the translational and vibrational modes.

4.2 Determination of Selection Rules

The vibrations in solids are governed by the net effect of various types of interactions leading to the complex force field potential. Hornig[32] has shown that it can be written as

$$V = \sum_n V_n + \sum_n \sum_k V_{nk} + V_l + V_{ln} \qquad (3.66)$$
$$n \neq k$$

where the four terms represent, respectively, the potential energies due to internal vibrations, interaction between internal vibrations, lattice modes and interaction between lattice and internal modes. The two most frequently used approaches for determining the selection rules are the site group approximation which effectively uses only the first term in the expression (3.66) and the factor group approximation which takes the first two terms into account.

4.3 The Site Group Approximation

Halford[33], in his theory for site group approximation, considers the molecule as moving in a potential field whose symmetry is that of the crystal. The crystal

belongs to one of the 230 space groups. Any group, S, of operations of any space group can be decomposed into a subgroup T of the translational operations and a sub-group U of rotational operations[8,9]. The subgroup U is isomorphic with one of the 32 point groups. Since

$$S = U \times T \tag{3.67}$$

Therefore, the subgroup U is a factor group of S, and the irreducible representations of U are also irreducible representations of S. The symmetry of any point in the lattice can be specified in terms of the site group which is the subgroup of the space group. The centre of mass of the molecule remains invariant under the opera-tions of the point group to which the molecule belongs and its equilibrium position is called the site. Having determined the site group, the irreducible representations of the site group corresponding to those of the molecular point group are obtained. Tables[30,31,34] for this purpose, termed as correlation tables are available. The selec-tion rules for the site group are then found by looking up the character table of the corresponding point group. Though the site group approximation provides adequate basis for determining the selection rules associated with the internal vibrations in the crystals, it is inadequate for the determination of selection rules for external vibrations.

4.4 The Factor Group Approximation.

In this approximation, the number and activity
of the vibrations of the complete unit cell is determined,
a treatment first developed by Bhagavantam and Venkatarayudu[35].
According to this approximation, a crystal composed of N
unit cells, each containing n atoms will have 3nN modes
of motions altogether. However, only those modes, in
which equivalent atoms are in phase, are active as funda-
mentals in the infrared or Raman. The remaining modes
may be seen as combination of very low intensity. This
way only the modes of motion of one unit cell need to be
determined. This can be done by considering the factor
group, which is in this sense, the subgroup U of the
space group consisting of its rotational operations.
The factor group is isomorphic with one of the 32 point
groups and is designated by the Scheonflies space group
symbol without its numerical superscript. Apart from
the factor group we need to know the symmetry operations
to which each atom is invariant, that is the site group
of each atomic position, and also the unit cell content.
The determination of the selection rules for the vibra-
tional activity is carreied out exactly the same way as
for the free molecule, using the character table of the
point group to which the factor group is isomorphic.

The next step in the factor group analysis is the classification of the vibrations of the unit cell into various types. Out of the 3n modes associated with a unit cell, 3 represent translation of the crystal as a whole which are known as acoustic modes and are not infrared or Raman active as fundamentals, but may be observed as combinations of low intensity with active fundamentals. The remaining (3n-3) modes are divided into external and internal modes. The external modes may be translational or rotational. For example, consider a crystal made up entirely of nonlinear polyatomic molecules with p atoms in the molecule and let the unit cell contain z such molecules. Then there will be 3zp modes, made up of 3 acoustic, 3z rotational, 3(z-1) translational and z(3p-6) internal.

4.5 Determination of Number of Modes Belonging to Each Irreducible Representation

If a_j is the number of times the j-th irreducible representation is contained in the reducible representation and the character of this j-th irreducible representation is $X^{(j)}(R)$, then

$$a_j = 1/h \sum_k X^{(j)}(R) \, X(R) \qquad (3.68)$$

where h is the order of the group and $X(R)$ is $X(\mu)$

or $\chi(\alpha)$ for determining infrared and Raman activity respectively. If $a_j = 0$, vibration of j-th representations are inactive, if $a_j \neq 0$, they are active. This information can be obtained from the character table of the point group.

REFERENCES

1. M.G. Mayer, Phys. Rev. 60, 184 (1941).

2. C.K. Jorgensen, J. Inorg. Nuc. Chem. 1, 301 (1955).

3. A.J. Freeman and R.E. Watson, Phys. Rev. 127, 2058 (1962).

4. E.U. Condon and G.H. Shortley, The Theory of Atomic Spectra, Cambridge University Press, Cambridge (1935).

5. B.R. Judd, Operator Techniques in Spectroscopy, McGraw-Hill Book Co., New York (1963).

6. G. Racah, Phys. Rev. 76, 1352 (1949).

7. G. Racah, Phys. Rev. 62, 438 (1942).

8. G. Racah, Phys. Rev. 63, 367 (1943).

9. M. Rotenberg, et al., 3j and 6j Symbols, M.I.T. Press, Cambridge, Mass. (1959).

10. B.G. Wybourne, Spectroscopic Properties of Rare Earths, Johnwilley and Sons, New York (1965).

11. C.W. Neilson and G.F. Koster, Spectroscopic Coefficients for p^n, d^n and f^n Configurations, M.I.T. Press, Cambridge, Mass. (1959).

12. B.R. Judd, Proc. Phys. Soc. (London), 82, 874 (1963).

13. K. Rajanak and B.G. Wybourne, J. Chem. Phys. 41, 565 (1964).

14. K. Rajanak and B.G. Wybourne, Phys. Rev. 132, 280 (1963).

15. B.G. Wybourne, J. Chem. Phys. 40, 1457 (1964).

16. H. Marvin, Phys. Rev. 71, 102 (1947).

17. B.G. Wybourne, J. Chem. Phys. 48, 2596 (1968).

18. H.A. Kramers, Proc. Amsterdam Acad. 33, 959 (1930).

19. M.T. Hutchings and D.K. Ray, Proc. Phys. Soc. 81, 663 (1963).

20. M.T. Hutchings, Solid State Physics 16, 227 (1964).

21. K. Pappalardo and D.L. Wood, J. Mol. Spectry. 10, 81 (1963).

22. G. Burns, J. Chem. Phys. 42, 377 (1965).

23. M.M. Curtis and D.J. Newman, J. Chem. Phys. 52, 1340 (1970).

24. D.J. Newman and G.E. Stedman, J. Chem. Phys. 71(6), 2366 (1979).

25. C.A. Morrison and R.P. Leavitt, J. Chem. Phys. 71(6), 2366 (1979).

26. P. Erdos and J.H. Kang, Phys. Rev. B6, 3393 (1972).

27. Donald S. Mcclure et al.,Electronic Spectra of Transition Metal Ions in Crystals, R.C.A. Labs, Project 5621, Task 56211.

28. A. Smekal, Naturwissenschaften 11, 873 (1923).

29. C.V. Raman, Ind. J. Phys. 2, 387 (1928).

30. A. Yariv, Quantum Electronics, John Willey, New York (1967).

31. Herzberg, G., Molecular Spectra and Molecular Spectra and Molecular Structure, D. Van Nostrand (Princeton) (Ist edition 1945).

32. Wilson, E.B., Decius, J.C., Cross, P.C., Molecular Vibrations, McGraw-Hill (New York), Ist Edition 1955.

33. D.F. Hornig, J. Chem. Phys. 16, 1063 (1948).

34. R.S. Halford, J. Chem. Phys. 14, 8 (1946).

35. Schonland, D., Molecular Symmetry, D. Van Nostrand (London), Ist Edition 1965.

36. Tinkham, M., Group Theory and Quantum Mechanics, McGraw-Hill (New York), Ist Edition, 1964.

37. D.M. Adam, Metal-ligand and Related Vibrations, Edward Arnold (London), Ist Edition 1967.

38. S. Bhagavantam and T. Venkataraydu, Proc. Ind. Acad. Sci. A9, 224 (1939).

CHAPTER IV

RESULTS AND DISCUSSION

1. EXPERIMENTAL RESULTS

It has already been pointed out in Chapter II
that the $PbMoO_4$ and $PbWO_4$ crystals were doped using
99.999% pure Nd_2O_3 (Koch-light laboratory, England) and
99.99% pure Nd_2O_3 (Apache Chemicals, USA). When samples
doped with 99.999% pure Nd_2O_3 were exposed to Ar^+ ion
laser radiation, no visible fluorescence was observed.
On the other hand, when samples doped with 99.9% pure
Nd_2O_3 were exposed to Ar^+ ion laser's blue lines (i.e.
20492, 20986 and 21838 cm^{-1} etc.) very strong visible
fluorescence was observed. The observed visible fluo-
rescence was not in agreement with the known energy level
scheme of Nd^{3+}[1]. Our charge compensation studies (i.e.
with varying Na^+ concentration) rule out the possibility
of Nd^{2+} being the source of the observed fluorescence.
Moreover, configuration $4f^2 5d^1$, which is an excited
configuration of Nd^{2+} lies low in energy[2]. The observa-
tion of sharp lines in the blue region is inconsistent
with such a possibility. This unusual behaviour of
samples prompted a fresh look on their absorption spectra.
Some extra lines are found in the absorption spectra of
samples doped with 99.9% pure Nd_2O_3 which are not present
in the absorption spectrum of the samples with 99.999%

pure Nd_2O_3. These extra lines which do not belong to Nd^{3+} ions are listed along with their polarizations and relative intensities in Table II-8 and II-10. From these tables we notice the near coincidence of the absorption lines in the blue region (20499 cm^{-1} for $PbMoO_4:Pr^{3+}$ and 20502 cm^{-1} for $PbWO_4:Pr^{3+}$) with the lowest energy (20492 cm^{-1}) Ar^+ laser line for which the induced fluorescence could be observed. Thus a correlation between the existence of extra lines in the absorption spectrum of $PbXO_4:Nd^{3+}$ and the appearance of visible fluorescence in these samples is clearly established. The sharpness of the fluorescence and the extra lines in the absorption spectrum indicates the presence of some additional rare earth ion impurity. A comparison of the energies of the extra lines with the spectra of rare earth ions[3] suggests the extra lines to be due to Pr^{3+} impurity which usually accompanies Nd^{3+}[4]. The near IR fluorescence observed in $PbMoO_4$ crystals is due to both Pr^{3+} and Nd^{3+} ions. In the forthcoming sections we present an interpretation of the observed fluorescence and absorption spectra of Nd^{3+} and Pr^{3+} impurity ions in these host crystals.

1.1 Fluorescence and Absorption Spectra of $PbMoO_4:Pr^{3+}$

A comparison of Pr^{3+} spectra in other hosts (e.g. $LaCl_3$, $LiYF_4$ etc.) reveals that the extra absorption lines (in our samples with 99.9% pure Nd_2O_3) in the blue region are due to transitions between the ground and the $^3P_{0,1,2}$ multiplets. Absorption line at 20499 (π) cm^{-1} corresponds to the transition $^3H_4$ (0 cm^{-1}) $^3P_0$. The multiplet $^3P_0$ does not split in the crystal field and is represented by the tetragonal symmetry representation Γ_1. On the assumption that this is an electric dipole transition, the selection rules for the f^2 configuration in S_4 symmetry (cf. Table III-8) would require the lowest Stark components of the ground multiplet $^3H_4$ to belong to the Γ_2 representation. At 90 K, the Ar^+ ion laser lines at 20492 and 20987 cm^{-1} which closely match (within the widths of these level cf Table II-8) the energy gaps for $^3P_0$ and $^3P_1$ respectively induce intense fluorescence from these multiplets. As expected this fluorescence is more intense when the incident radiation is absorbed by the samples in π-polarization. Fluorescence from $^3P_0$ state could also be observed when the samples are excited by the extreme blue line (21838 cm^{-1}) of Ar^+ ion laser. Apart from the fluorescence from the $^3P_0$ to the low lying multiplets we have observed fluorescence from $^1D_2$ multiplet

also when laser lines in the blue region are used for excitation. Esterowitz and coworkers[6] have not reported $^1D_2$ fluorescence in $LiYF_4:Pr^{3+}$ samples under similar conditions. The multiplet $^1D_2$ is populated by the transition $^3P_0 \longrightarrow {}^1D_2$. Due to the spectral range limitation of our monochromator, we were unable to ascertain the nature of this transition (radiative or nonradiative). According to Reut and Ryskin[7], $^3P_0 - {}^1D_2$ transition is primarily non-radiative. The large energy gap between $^3P_0$ and $^1D_2$ multiplets, the temperature independence of the ratio of intensities from $^3P_0$ and $^1D_2$ levels, and the constancy of this ratio under excitation to different terms of ^3P_J multiplet rule out the possibility of direct, Raman, Orbach or multiphonon process es being responsible for the non-radiative transition to $^1D_2$. Further at these low levels of Pr^{3+} concentration the ion pair cross relaxation process will also be ineffective. Reut and Ryskin have proposed that the de-excitation can take place through the interaction of charge transfer states (virtual charge transfer). This mechanism involves transfer of an electron from the $^3P_0$ level to one of the closest lattice ions, relaxation to an intermediate state and then again transfer of electron to Pr^{3+} but now in $^1D_2$ level. These authors have given the following expression for the decay rate for such a process.

$$W = \frac{I_{\sigma D}}{I_{\sigma p}} \quad \frac{A_{\sigma p}}{A_{\sigma D}} \cdot \frac{1}{\tau_D} \cdot \frac{1}{\alpha(T)} \qquad (4.1)$$

where I_D and I_p are the relative intensities for $^1D_2 \rightarrow {}^3H_4$ and $^3P_0 \rightarrow {}^3H_4$ transitions. τ_D is the lifetime of $^1D_2$ level $\alpha(T) = \dfrac{1}{1 + e^{/kT}}$ is a factor taking into account the population in the sublevel $^1\Gamma_1$ of the $^1D_2$ term and

$$\frac{A_{\sigma p}}{A_{\sigma D}} = \nu^2_{\sigma p} / \nu^2_{\sigma D} \int \alpha_{\sigma p}(\nu)\,d\nu / \int \alpha_{\sigma D}(\nu)\,d\nu \qquad (4.2)$$

is the ratio of transition (radiative) probability. They have estimated $^3P_0 \rightarrow {}^1D_2$ decay rate for $PbMoO_4$ which is approximately five times higher than for $PbWO_4$. Our absorption intensity measurements (cf. Tables II-8 and II-10) show that

$$\frac{(A_{\sigma p}/A_{\sigma D})_{PbMoO_4}}{(A_{\sigma p}/A_{\sigma D})_{PbWO_4}} \simeq 1.5 \qquad (4.3)$$

Further, from our fluorescence intensity measurements (cf. Tables II-3 - 4) it is seen that

$$\frac{(I_{\sigma D}/I_{\sigma p})_{PbMoO_4}}{(I_{\sigma D}/I_{\sigma p})_{PbWO_4}} \simeq 1.1$$

The factors $\alpha(T)$ because of similar Stark splittings will be the same for $PbMo_4:Pr^{3+}$ and $PbWO_4:Pr^{3+}$ at a given temperature.

To require the decay rate in $PbMoO_4:Pr^{3+}$ to be five times higher than in $PbWO_4:Pr^{3+}$, the life-time of $^1D_2$ level in $PbWO_4:Pr^{3+}$ should be three times higher than that in $PbMoO_4:Pr^{3+}$. The validity of this hypothesis can be checked if the life-times of $^1D_2$ state in $PbMoO_4:Pr^{3+}$ and $PbWO_4:Pr^{3+}$ are measured. Anyhow, under these excitation conditions both $^3P_0$ and $^1D_2$ levels radiate strongly. The observed fluorescence spectra consist of well separated groups of sharp lines which are listed in Tables II-3 and II-4. Based on the absorption and fluorescence data and the electric dipole selection rules given in Table II-6, an energy level diagram for Pr^{3+} in $PbMoO_4$ crystals has been proposed. This is given in Fig. IV-1. The following groups of transitions are observed.

$^3P_0 \rightarrow {}^3H_4$
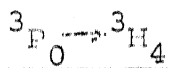
This group of transitions is shown in the segment a-b of Fig. II-12. Besides the fluorescence lines from $^3P_0$ to $^3H_4$ multiplet, some Raman lines also sometime appear in this group. These could be sorted out with the help of Raman spectra given in Fig. II-22. These

interfering Raman lines appear at 20174 and 19621 cm^{-1} when the sample is excited by 20492 cm^{-1} (4880 Å) Ar^{+} laser line and at 20116 cm^{-1} when excited by 20987 cm^{-1} laser line. However, Raman lines do not overlap with the fluorescence from $^{3}P_{0} \longrightarrow {}^{3}H_{4}$ when the sample is excited by 21838 cm^{-1} laser line. Excluding the Raman lines, a total of seven lines at 20499 (π), 20438 (σ), 20378 (π), 20324 (π), 20317 (π), 20238 (π) and 20101 (σ) cm^{-1} are observed. The lines at 20499, 20438 and 20101 cm^{-1} represent transitions from $^{3}P_{0}$ to $^{3}H_{4}$ Stark levels at $0(\Gamma_{2})$, $61(\Gamma_{3})$ and $398(\Gamma_{3})$ cm^{-1} respectively. Other lines which are weak (e.g. lines at 20378, 20238 cm^{-1} shifted by 60 and 200 cm^{-1} relative to the no phonon line at 20438 cm^{-1} and lines at 20324, 20317 cm^{-1} which are displaced by 175 and 182 cm^{-1} respectively relative to no phonon line at 20499 cm^{-1}) belong to the vibronic transitions. Their shifts are equal to Raman active vibrational frequencies (cf. Table II-11).

$^{1}D_{2} \rightarrow {}^{3}H_{4}$
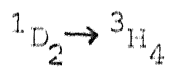
Five transitions at 16755 (π), 16632 (π), 16751 (σ), 16522 (σ) and 16452 (π) cm^{-1} are observed in this group (cf segment e - f of Fig. II-12). Three lower levels of $^{1}D_{2}$ multiplet at 16583 (Γ_{2}), 16632 (Γ_{1}) and 16820 (Γ_{3}) cm^{-1} and a $^{3}H_{4}$ level at 131 (Γ_{1}) cm^{-1}

could be established from this group of transitions.
The $^3H_4$ levels at 0 (Γ_2) and 61 (Γ_3) cm^{-1} already esta-
blished from $^3P_0 \longrightarrow ^3H_4$ group of transitions could be
confirmed.

$^3P_0 \longrightarrow ^3H_5$
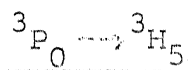
Three transitions at 18278 (π), 18254 (σ) and
18010 (π) cm^{-1} are observed in this group (cf segment
c - d of Fig. II-12). Reut et al have not reported
any spectral lines in this region. Three levels of
$^3H_5$ at 2221 (Γ_3), 2245 (Γ_3) and 2489 (Γ_2) could be
established.

$^1D_2 \longrightarrow ^3H_5$

Four very weak transitions at 14387 (σ),
14375 (π), 14361 (π) and 14338 (π) cm^{-1} have been
observed in this group (cf segment e - f of Fig. II-13).
The transition 14361 cm^{-1} has been placed between the
levels 16583 (Γ_2) cm^{-1} of $^1D_2$ and 2221 (Γ_3) cm^{-1} of
$^3H_5$ multiplets. Transitions 14387 and 14338 cm^{-1} ori-
ginate from the levels at 16632 and 16583 cm^{-1} of $^1D_2$
multiplet respectively and terminate at 2245 (Γ_3)
cm^{-1} level of $^3H_5$. The transition at 14375 cm^{-1} could
not be placed in this scheme.

$^3P_0 \longrightarrow {}^3H_6$
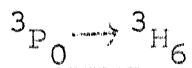
Two transitions at 16180 (π) and 16133 (σ) cm^{-1} have been observed for this group (cf segment a - b of Fig. II-13). This observation agrees well with that of Reut et al[8]. Two levels of $^3H_6$ at 4319 (Γ_2) and 4360 (Γ_3) cm^{-1} could be established from this data.

$^1D_2 \longrightarrow {}^3H_6$
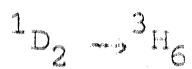
This group contains five lines at 12310 (π), 12210 (π), 12187 (π), 12085 (σ), 12028 (σ) cm^{-1} (cf segment a - b of Fig. II-14). Authors of Ref. 8 have not reported the weak transitions at 12085 and 12028 cm^{-1}. Further, we do not observe lines at 12266 and 12173 cm^{-1} reported by these authors. Levels at 4319 (Γ_2) and 4360 (Γ_3) cm^{-1} of $^3H_6$ already determined from the $^3P_0 \longrightarrow {}^3H_6$ fluorescence could be confirmed and two more levels at 4396 (Γ_1) and 4555 (Γ_3) cm^{-1} could be established from this group of transitions.

$^3P_0 \longrightarrow {}^3F_2$
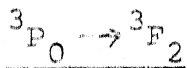
Two very strong lines at 15461 (π) and 15452 (σ) cm^{-1} shown in segment c - d of Fig. II-13 have been observed in this group. Two levels of $^3F_2$ at 5038 (Γ_2) and 5047 (Γ_3) cm^{-1} could be established. This assignment is in agreement with the one given in Ref. 8.

$^1D_2 \longrightarrow {}^3F_2$
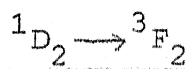
Only two lines at 11587 (σ) and 11533 (π) cm^{-1} are observed in this group (cf. segment c - d of Fig. II-14) instead of the three reported in Ref. 8. The missing line at 11593 cm^{-1} is probably obscured by the broad band at 11587 cm^{-1}. Further, the placement of the transition 11534 (σ) cm^{-1} between the Stark level 5062 (Γ_2) cm^{-1} of the multiplet $^3F_2$ and 16583 (Γ_2) cm^{-1} level of $^1D_2$ multiplet by these authors is not warranted from selection rules and energy considerations. In our level scheme the lines at 11587 and 11534 cm^{-1} originate from 16632 (Γ_1) and 16583 (Γ_2) cm^{-1} level of $^1D_2$ respectively and terminate at the level 5047 (Γ_3) cm^{-1} of $^3F_2$.

$^3P_0 \longrightarrow {}^3F_3$
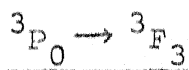
Four lines at 14115 (σ), 14036 (π), 14019 (π) and 13990 (σ) cm^{-1} are observed in this group (cf. segment f-g of Fig. II-13). The transition at 13990 cm^{-1} is not reported in Ref. 8. Three levels of $^3F_3$ at 6388 (Γ_3), 6413 (Γ_2) and 6480 (Γ_2) cm^{-1} could be determined from this information.

$^1D_2 \longrightarrow {}^3F_3$
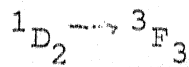
This group contains only four lines at 10195 (σ), 10153 (π), 10121 (π) and 10072 (σ) cm^{-1} (cf. section a-b

of Fig. II-15). The lines at 10215 and 10244 cm^{-1}
reported in Ref. 8 have not been observed by us. Apart
from the levels derived from $^3P_0 - ^3F_3$ fluorescence,
one more $^3F_3$ level at 6509 (Γ_3) cm^{-1} could be established.

$^3P_0 \longrightarrow ^3F_4$

Two lines at 13687 (σ) and 13662(π) cm^{-1} appear
in this group (cf. segment h-i of Fig. II-13). These
have been placed in the level diagram between $^3P_0$ (20499
cm^{-1}) and the levels 6812 (Γ_3) and 6837 (Γ_2) cm^{-1} of
$^3F_4$ respectively. This assignment is in agreement with
Ref. 8.

$^1D_2 \longrightarrow ^3F_4$
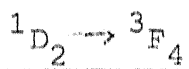
Six lines at 9813 (σ), 9792 (π), 9767 (σ), 9638
(π), 9598 (σ) and 9541 (π) cm^{-1} are observed in this
group (cf. segment c - d of Fig. II-15). In the energy
map, lines at 9813 and 9792 cm^{-1} have been placed bet-
ween the level 16632 (Γ_1) of $^1D_2$ multiplet and the
level 6812 (Γ_3) cm^{-1} of $^3F_4$. Transitions at 9767,
9638, 9598 and 9541 cm^{-1} are placed between the level
16583 (Γ_2) of $^1D_2$ and $^3F_4$ levels at 6812 (Γ_3), 6944
(Γ_1), 6985 (Γ_3) and 7044 (Γ_1) cm^{-1} respectively.
Transition at 9647 cm^{-1} reported by Reut et al[8] is not
observed here.
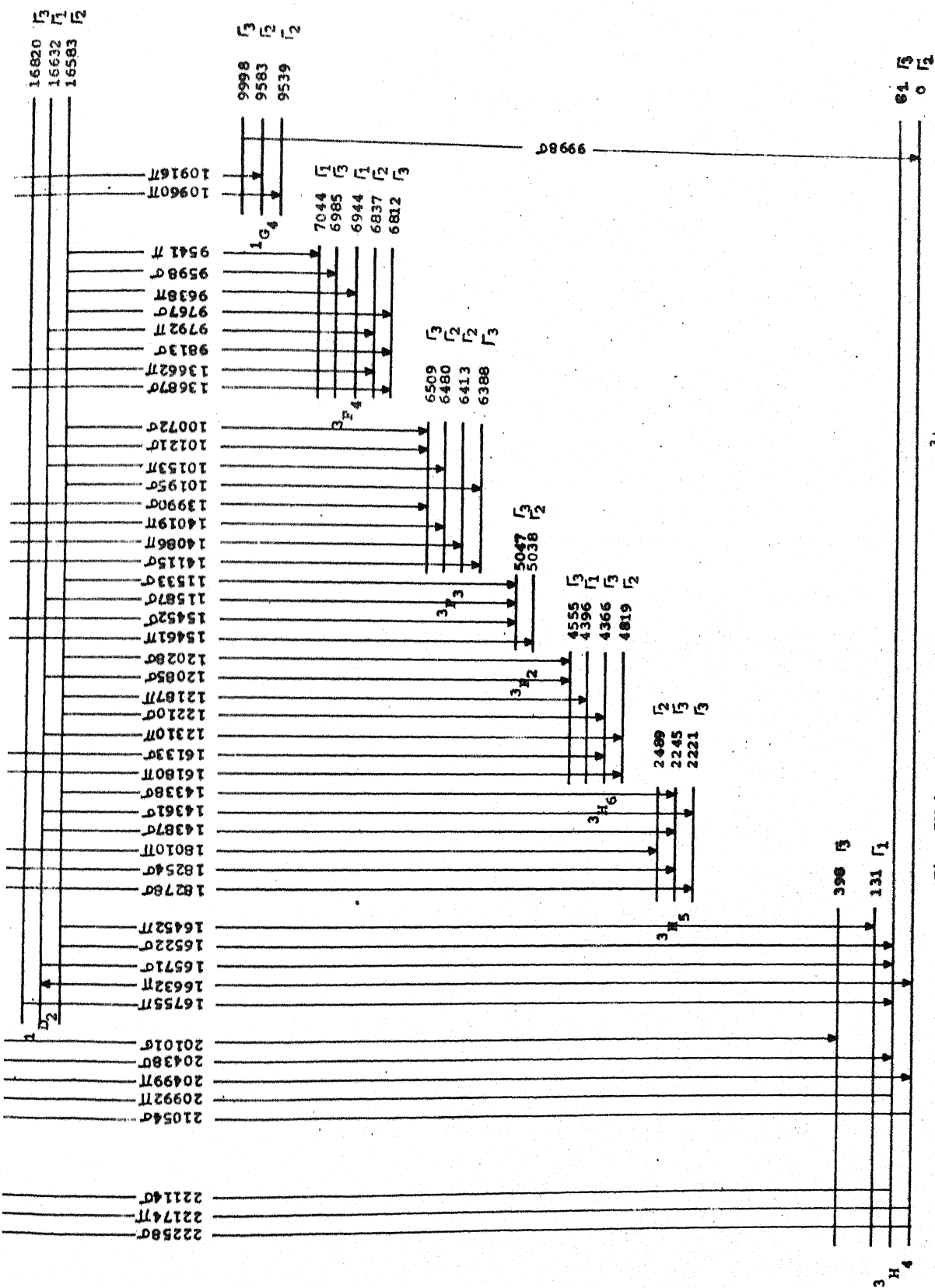
130

Fig. IV-1 : Energy Level Scheme for PbMoO$_4$:Pr^{3+}

Upward arrow - absorption transition
Downward arrow - emission transition

$$^3P_0 \longrightarrow {}^1G_4$$
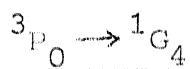
In this group we do not observed the line at 10752 (σ) reported in Ref. 8. Instead we see two lines at 10916 (π) cm^{-1} and 10960 (π) cm^{-1} (cf segment e - f of Fig. II-15). These are the transitions from the level $^3P_0$ to levels 9539 (Γ_2) and 9583 (Γ_2) cm^{-1} of $^1G_4$.

Apart from this observation one line at 9998 (σ) cm^{-1} is observed (cf segment b - c of Fig. II-14). This may be a transition from $^1G_4$ to $^3H_4$.

1.2 Fluorescence and Absorption Spectra of $PbWO_4:Pr^3$

The fluorescence and absorption spectra of Pr^{3+} in $PbWO_4$ and $PbMoO_4$ are quite similar. The major difference lies in the fact that for $PbWO_4:Pr^{3+}$ the two additional levels (located at ~22 cm^{-1} on either side of $^3P_0$ also show observable fluorescence to many of the lower Pr^{3+} multiplets. This feature is absent in $PbMoO_4$ crystals. These two levels may belong to $^1I_6$ multiplet. Most of the Pr^{3+} multiplets in $PbWO_4$ are somewhat higher (~30 cm^{-1}) than their energy positions in $PbMoO_4$. However, the limited Stark structure observed for $PbWO_4$ has splittings comparable to those observed for $PbMoO_4$. Based on the fluorescence (cf Table II-6 and 7) and absorption (cf Table II-10) data, an energy level diagram for $PbWO_4:Pr^{3+}$ (shown in Fig. IV-2) has

been proposed here. Relatively fewer levels could be established for $PbWO_4:Pr^{3+}$ because no near IR region fluorescence could be observed. Even the visible Pr^{3+} fluorescence in $PbWO_4$ is considerably weaker than one observed in $PbMoO_4$. The relatively weak fluorescence in $PbWO_4$ can be explained in the following manner. The absorption of laser radiation at 20492 cm^{-1} can not excite $^3P_0$ (20564 cm^{-1}) from the ground level $^3H_4$ (Γ_2) (0 cm^{-1}). The $^3P_0$ level in $PbWO_4$ can however be approached if substantial population exists in the excited level(s) of the ground multiplet. In case of $PbMoO_4$ this excitation takes place through the transition $^3H_4$ (Γ_2)(0 cm^{-1}) $\rightarrow$ $^3P_0$ (Γ_1) (20499 cm^{-1}). The laser radiation will be absorbed more efficiently in the later case (cf Tables II-8 and II-10). A similar situation occurs when 20987 cm^{-1} line is used to induce fluorescence in $PbWO_4:Pr^{3+}$. Fluorescence can be induced with the 4727 $\overset{o}{A}$ (21154 cm^{-1}) line of Ar^+ ion laser but this line is very weak compared to 20492 or 20987 cm^{-1} laser lines. Details of the observed groups of transitions in $PbWO_4:Pr^{3+}$ are given below.

$^3P_0 \rightarrow {}^3H_4$
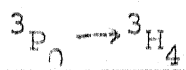
This group of transitions is shown in the a - b section of Fig. II-16. As in the case of $PbMoO_4:Pr^{3+}$,

here also some Raman line overlap in this region. The interfering Raman lines lie at 20249 cm^{-1} when fluorescence is induced by 21154 cm^{-1} line of Ar^+ ion laser. A total of nine lines at 20586 (π), 20564 (π), 20543 (σ), 20502 (σ), 20398 (σ), 20362 (σ), 20335 (π), 20245 (π) and 20155 (σ) cm^{-1} are seen in this group. The lines at 20586 cm^{-1} and 20543 cm^{-1} are from $^1I_6$ to ground level of $^3H_4$. The line at 20564 cm^{-1} is a transition between $^3P_0$ and the ground level of $^3H_4$, while the lines at 20502 and 20155 cm^{-1} have been placed between $^3P_0$ and the Stark levels of $^3H_4$ at 62 (Γ_3) and 409 (Γ_3) cm^{-1} respectively. The weak lines at 20398 cm^{-1} and 20362 cm^{-1} spaced by 181 cm^{-1} relative to no phonon lines at 20586 and 20543 cm^{-1} and 20245 cm^{-1} shifted by 319 cm^{-1} relative to no phonon line at 20564 cm^{-1} belong to vibronic transitions. Their shifts relative to no phonon lines match with observed Raman vibrational frequencies (cf Table II-12).

$^1D_2 \longrightarrow {}^3H_4$
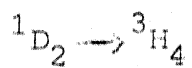
The structure of this group is different from that of the corresponding group in the case of $PbMoO_4:Pr^{3+}$. Six lines at 16865 (σ), 16661 (π), 16601 (σ), 16587 (π), 16557 (σ) and 16545 (σ) cm^{-1} are present in this group (cf section e - f of Fig.II-16).

Three lower levels of $^1D_2$ i.e. at 16865 (Γ_3), 16661 (Γ_1), 16617 (Γ_2) cm^{-1} could be established from this information. The $^3H_4$ levels at 0 (Γ_2) and 62 (Γ_3) cm^{-1} established from the fluorescence of $^3P_0 \longrightarrow {}^3H_4$ could be verified. Transitions at 16587 and 16545 cm^{-1} could not be placed in this scheme.

$^3P_0 \longrightarrow {}^3H_5$
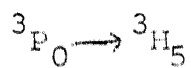
Only one strong transition at 18061 (π) cm^{-1} as shown in the section c - d of Fig. II-16 is seen in this group. This we believe is a transition from $^3P_0$ to 2503 (Γ_2) level of $^3H_5$ (analogous to 1810 cm^{-1} line in PbMoO$_4$:Pr^{3+}).

$^3P_0 \longrightarrow {}^3H_6$
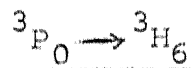
Two prominent lines at 16239 (π) and 16191 (σ) cm^{-1} (shown in the section a - b of Fig. II-17) are observed in this group. These transitions have been placed between $^3P_0$ and the levels 4325 (Γ_2) and 4373 (Γ_3) cm^{-1} of $^3H_6$ respectively.

$^3P_0 \longrightarrow {}^3F_2$
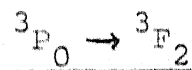
Here two rather strong lines at 15507 (π) and 15501 (σ) cm^{-1} are accompanied by several weak ones (cf segment c - d of Fig. II-17). In accordance with

the level scheme for $PbMoO_4$, these transitions are placed between $^3P_0$ and the levels 5057 (Γ_2) and 5063 (Γ_3) cm^{-1} of $^3F_2$. The line at 15529 (π) cm^{-1}, we believe is a transition from 20586 (Γ_1) cm^{-1} of $^1I_6$ level to 5057 (Γ_2) cm^{-1} of $^3F_2$.

$^3P_0 \rightarrow {}^3F_3$
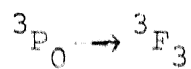
Three lines at 14191 (σ), 14165 (σ) and 14137 (π) cm^{-1} belong to this group (cf segment e - f of Fig. II-17). Analogous to $PbMoO_4:Pr^{3+}$ the transitions at 14165 and 14137 cm^{-1} are from $^3P_0$ to levels 6399 (Γ_3) and 6427 (Γ_2) cm^{-1} of $^3F_3$. Line at 14191 cm^{-1} is a transition from 20586 (Γ_1) cm^{-1} level of $^1I_6$ to 6399 (Γ_3) cm^{-1} level of $^3F_3$.

$^3P_0 \rightarrow {}^3F_4$
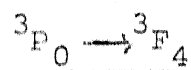
Three lines at 13737 (σ), 13710 (π) and 13721 (π) cm^{-1} are observed in this group (cf segment g - h of Fig. II-17). The lines at 13737 and 13710 cm^{-1} are transitions from $^3P_0$ to levels 6827 (Γ_3) and 6854 (Γ_2) of $^3F_4$ multiplet. The line at 13721 (π) cm^{-1} is a transition between the level 20543 (Γ_3) cm^{-1} of $^1I_6$ and level 6827 (Γ_3) cm^{-1} of $^3F_4$.

Fig. IV-2 : Energy Level Scheme for $PbWO_4:Pr^{3+}$

Upward arrow — absorption transition ; downward arrow — emission transition

136

1.3 Fluorescence and Absorption Spectra of $PbMoO_4:Nd^{3+}$

In the near IR region, fluorescence from $^4F_{3/2}$ multiplet of Nd^{3+} to lowlying $^4I_{9/2}$ and $^4I_{11/2}$ multiplets has been observed. Fluorescence from $^4F_{3/2}$ to $^4I_{13/2}$ and $^4I_{15/2}$ multiplets could not be observed due to the spectral range limitations of our monochromator. The observed near IR fluorescence due to Nd^{3+} ions despite their much higher concentration in the samples is much weaker compared to that of Pr^{3+} ions. The reason for this relatively weak fluorescence of Nd^{3+} ions is the unavailability of any strongly absorbing level in the blue region[1] (cf Fig. II-18) for an efficient excitation of Nd^{3+} ions by Ar^+ ion laser radiation, in particular 4880 Å laser line used for this purpose. The positions of $^4F_{3/2}$ levels could be easily ascertained from the $^4I_{9/2} \longrightarrow {}^4F_{3/2}$ absorption spectrum at 90 K (cf Fig. II-19 and Table II-9). The details of the observed groups of transitions in the fluorescence spectrum (cf Table II-5) are given below.

$^4F_{3/2} - {}^4I_{9/2}$

Eight lines at 11435 (π), 11397 (π), 11355 (π), 11304 (σ), 112251(π), 11191 (π), 11089 (π) and 11033 ($\pi\sigma$) are observed in this group (cf segment d-e of Fig. II-12). The line at 11451 cm^{-1}, observed by

Kariss and Feofilov, could not be observed here because
of the extremely weak fluorescence from Nd^{3+} in our case.
For the same reason, the line at 11394 cm^{-1}, observed by
these authors in both π and σ polarizations could be
observed here only in π polarization and not in σ. The
origin of the line at 11435 (π) cm^{-1} is not understood
as we could not attribute this line either to Nd^{3+} or Pr^{3+}
The observed polarizations and   wave number posi-
tions of other lines in this group are in agreement with
the data of Ref. 1.

$^4F_{3/2} \rightarrow {}^4I_{11/2}$
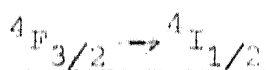
In this group (cf segment c - d of Fig. II-13),
the fluorescence lines observed at 9490 (π), 9447 (π),
9394 (σ), 9357 (π), 9294 (π) and 9262 (π) cm^{-1} are
in reasonably good agreement with their reported positions
in Ref. 1. However, lines at 9462, 9435, 9405, 9320,
9236 cm^{-1} reported in Ref. 1 could not be observed here
once again due to weak fluorescence.

These observed groups of transitions are repre-
sented in the energy level diagram given in Fig. IV-3.

1.4   Laser Power Dependence of Fluorescence Intensity

Intensity of $^1D_2 \rightarrow {}^3H_4$ and $^3P_0 \rightarrow {}^3H_6$ fluorescence
was measured as a function of laser power using neutral
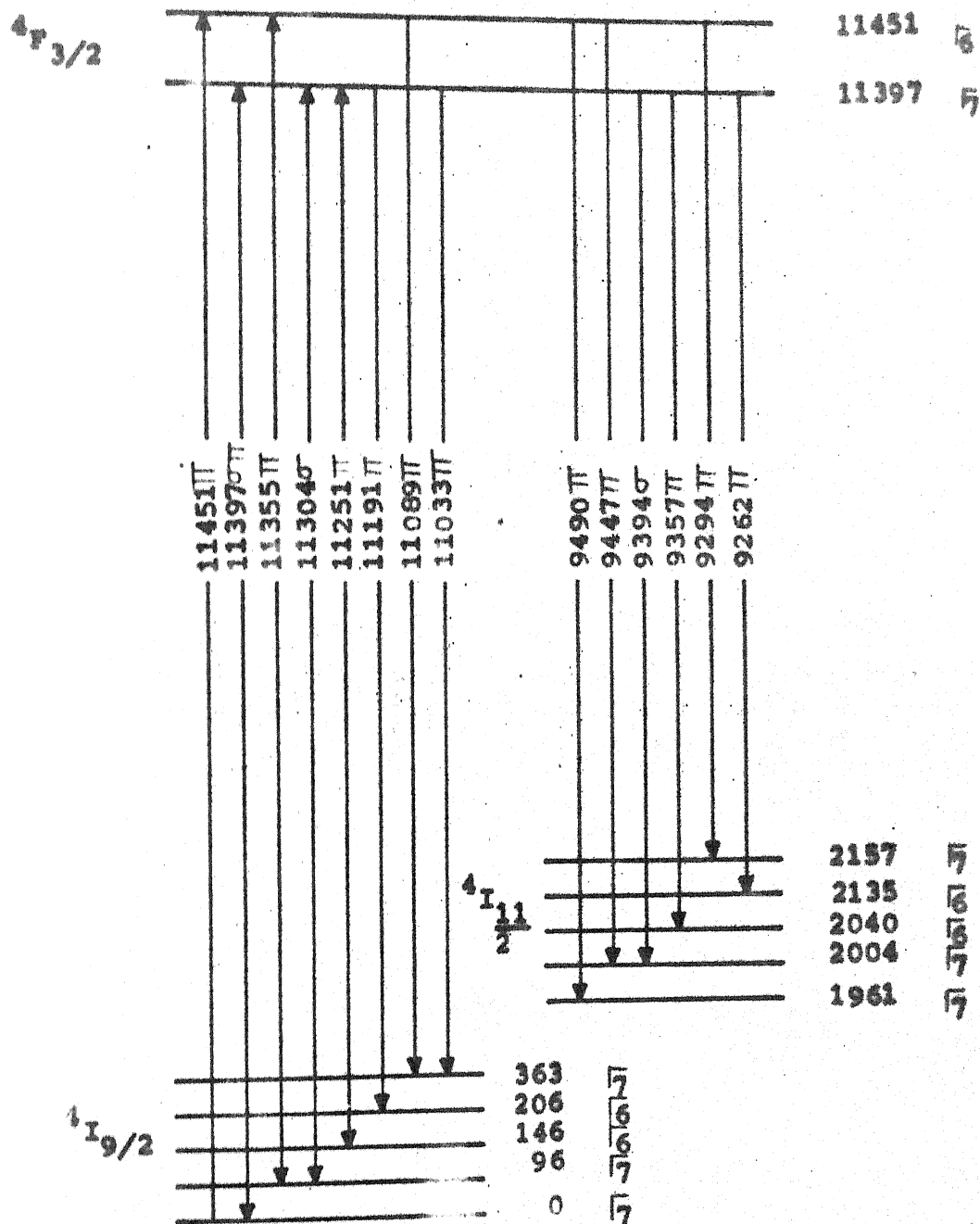
Fig.IV-3 : Partial Energy Level Diagram of $PbMoO_4 : Nd^{3+}$

Upward arrow - absorption transition
Downward arrow - emission transition
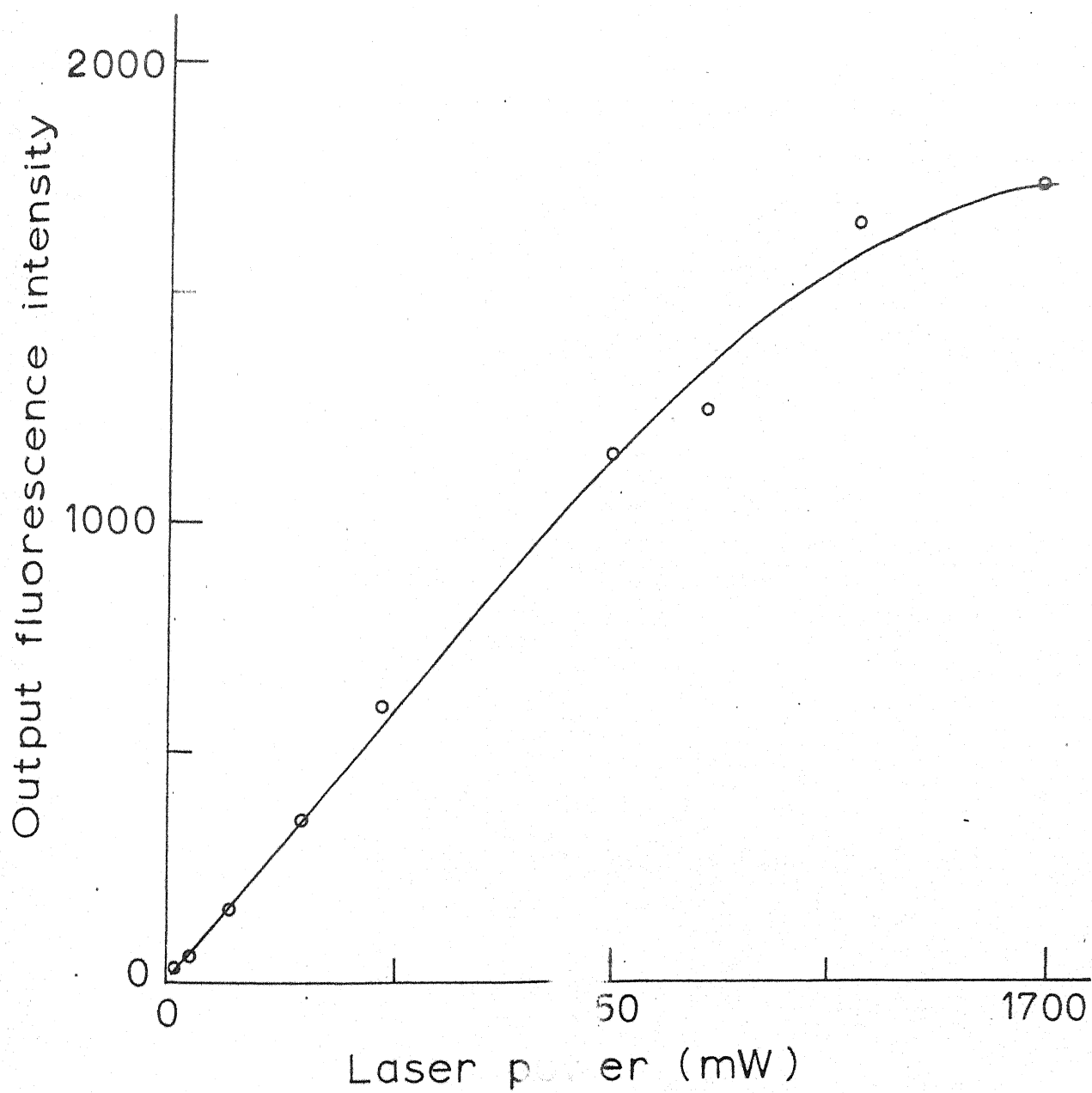
Fig. IV-4: Fluorescence   s- Laser power

density filters. This dependence is shown in Fig. IV-4.
It shows that at low power level of incident laser radia-
tion, the fluorescence output increases linearly with
the incident laser power, while at power levels greater
than 1 watt the fluorescence output tends to saturate.
At saturation all ions present in the optical path are
involved in the fluorescence.

2. QUANTITATIVE RESULTS

A detailed interpretation of the experimental
data will require the diagonalization of the complete
energy matrix in which the Coulomb, spin-orbit and
crystal field interactions are included. If the free
ion and crystal field parameters are simultaneously
treated as adjustable parameters in a least squares
fit, the crystal field parameters would try to compen-
sate for the inadequacies of the free ion parameters.
This may improve the fit for the C.G.'s of the levels
but the crystal field splittings will be adversely
affected. Hence, it is desirable to do the calcula-
tions in two steps. In the first step the free ion
parameters are adjusted to fit the "free-ion" levels.
In the second stage of calculations the crystal field
interaction is brought in and crystal field parameters
are adjusted in the same way.

2.1 Free Ion Calculations

To obtain the free-ion levels, one needs to calculate the C.G.'s of the Stark splitted levels of each multiplet. In rare earth spectrum all the Stark components are generally not seen. Sometimes the selection rules forbid some transitions and even all allowed transitions may not be observed; some lines are either weak or so broad as to blur the details. Further, it is also not always possible to separate levels of different J-multiplets with certainty. In such a situation an initial set of crystal field parameters can be used to estimate the positions of missing levels and thus approximate centre's of gravity can be estimated. The positions of centres of gravity can be improved with each refinement of crystal field until no appreciable change occurs in the position of free ion levels. Free ion C.G.'s were roughly estimated from the experimental data for the multiplets $^3H_4$, $^3H_6$. $^3F_2$, $^3F_3$, $^3F_4$, $^1D_2$, $^3P_0$ and $^3P_2$. For determining the C.G. of $^1D_2$ multiplet, we used the position of the uppermost Γ_2 Stark component as reported in Ref. 8 because this level was missing in our data. The C.G.'s of $^3P_0$, $^1D_2$, $^3F_3$ and $^3H_4$ multiplets were quite accurately determined from our experimental data while the estimate of C.G.'s of other multiplets e.g. $^3H_6$, $^3P_2$,

$^3F_4$ and $^3F_2$ was rather crude since complete structure of these multiplets could not be observed. Free ion energy matrices were constructed for Pr^{3+} in the intermediate coupling scheme following the procedure outlined in appendix III. Free ion Hamiltonian included electrostatic, spin orbit and configuration interactions. The angular parts of matrix elements were calculated using the formulae given in Chapter III. The program was written so as to arrange the eigenvalues in ascending order for each of the J-value. Program was tested with various sets of parameters available in the literature. It is seen from the earlier work[9] that four parameter fit (neglecting configuration interaction) leads to large r.m.s. deviation (~100 cm^{-1}) compared to the fit yielded by seven parameters. Hence a seven parameter fit was preferred over four parameter fit. The parameters given by Carnall, Rajanak and Fields for LaCl$_3$[9] predict free-ion levels which are in fair agreement with our estimated C.G.'s although some discrepancies remain. For $^3F_2$ and $^3P_2$ multiplets the disagreement was as high as 100 cm^{-1}. It was therefore necessary to improve upon these parameters to some extent. Thus a seven parameter fit was carried out for eight estimated free-ion levels using the parameters of Carnall et al as the starting parameters. The resulting parameters gave

an r.m.s. deviation[+] of 16 cm^{-1} and are listed in
Table IV-1 along with the estimated and calculated free-
ion C.G. In the parameter set so obtained, only two
parameters E^1 and γ differ substantially from their
initial values while others remain almost unaffected.
The two parameters E^1 and γ are related by common term[10]
S(S+1). If one of these changes other will also naturally
get affected. The levels which are included in the least
squares calculations are rather insensitive to these para-
meters. This can be verified from the numerically calcu-
lated partial derivatives of the chi-squares function
(sum of squares) with respect to the parameters
(cf Table IV-2) which is a measure of the sensitivity to
the parameters of the function. Thus we feel that the

[+] The r.m.s. deviation has been defined as

$$\sigma = \sqrt{\sum_i \Delta_i^2 / n}$$

where Δ_i is the differences between calculated and
observed levels, n is the the number of levels used in
the least square fit. $F = \sum_i \Delta_i^2$ is the chi-square
function to be minimized in least squares calculations.

TABLE IV-1

Free-ion parameters obtained from seven parameters least squares fitting* of the estimated experimental free-ion C.G.'s.

$E_1 = 5336.2 \text{ cm}^{-1}$; $E_2 = 21.83 \text{ cm}^{-1}$; $E_3 = 460.18 \text{ cm}^{-1}$

$\zeta_{4f} = 736.92 \text{ cm}^{-1}$; $\alpha = 20.79 \text{ cm}^{-1}$; $\beta = -821.51 \text{ cm}^{-1}$

$\gamma = -2527.78 \text{ cm}^{-1}$

S.N.	Multiplet	Experimentally estimated C.G a (cm^{-1})	Calculated C.G. b (cm^{-1})	Difference c = (a-b) (cm^{-1})
1	$^3H_4$	200	200	0.0
2	$^3H_6$	4442	4427.8	14.2
3	$^3F_2$	5056	5061.4	-5.4
4	$^3F_3$	6447	6443.5	-23.5
5	$^3F_4$	6900	6898.9	1.1
6	$^1D_2$	16776	16776.5	-0.5
7	$^3P_0$	20498	20466.8	32
8	$^3P_2$	22203	22231.0	-28

r.m.s. deviation = 16.9 cm^{-1}

*starting parameters were those given in Ref. 10 for $LaCl_3:Pr^{3+}$. These are listed in Table IV-2

TABLE IV-2

Parameter Dependence of Chi-Square Function Including
$^3H_{4,6}$, $^3F_{2,3,4}$, $^1D_2$, $^3P_{0,2}$ Multiplets Free-ion Energies

Free Ion Parameter	Starting Parameter's Value	Parameter Dependence of Chi-Square Function $\partial F / \partial X$
E^1	4713.8	108.15
E^2	21.89	25580.00
E^3	464.23	22594.00
ζ_{4f}	742.68	1708.00
α	22.8999	-14755.00
β	-676.97	91.06
γ	599.51	18.85

resulting set of parameters describe the C.G.'s of free ion levels well.

2.2   Crystal Field Calculations

The wavefunctions obtained in the free ion calculations are used as zero order functions for the perturbation calculations of H'_{cry}. Energy matrices for the three representations Γ_1, Γ_2 and Γ_3 of S_4 were constructed according to the procedure given in appendix III. Angular parts of the matrix elements were calculated using the formulae given in chapter III, sec.-3. Initial set of crystal field parameters were derived from those of $PbMoO_4:Nd^{3+}$ following the approach outlined in chapter III. Since the exact positions of the experimental 'free-ion' levels are not known accurately the energy differences among the Stark splitted levels for each multiplet were calculated with respect to the lowest observed level of that multiplet. A total of eighteen such energy diffe- rences from various multiplets were used in a least squares fit. It was found that the initial set of para- meters were considerably off the mark. A four parameter least squares fit was carried out for the four levels of $^1D_2$. These parameters gave an r.m.s. deviation of 8 cm⁻¹ and are listed in Table IV-3. However, these parameters

Initial Parameter Values

TABLE IV-3

Crystal Field Parameters for the Four Parameters
Least Squares Fit* for the Stark Levels of $^1D_2$
Multiplet

$$B_0^2 = 215.19 \text{ cm}^{-1} \quad ; \quad B_0^4 = -643.05 \text{ cm}^{-1} \; ;$$

$$B_4^4 = -1002.9 \text{ cm}^{-1} \quad ; \quad B_{-4}^4 = 230.38 \text{ cm}^{-1}.$$

Stark Component	Experimental Energy (cm^{-1})	Calculated Energy (cm^{-1})	Difference c = (a-b) (cm^{-1})
Γ_2	9	-6.4	15.4
Γ_1	49	52.6	-3.6
Γ_3	238	239.4	-1.4
Γ_2	444	442.6	1.4

r.m.s. deviation = 8 cm^{-1}

*Free-ion parameters given in Table IV-1 were used in
this calculations. The initial crystal field para-
meters were derived from those given in Ref. 12 for
$PbMoO_4:Nd^{3+}$ following the procedure described in
Section 3 of Chapter III.

do not match at all with those reported in Ref. 8 for $^1D_2$. At this stage more energy difference were brought in and seven parameter fit was carried out for eight energy differences resulting from $^3H_4$, $^3F_3$ and $^1D_2$ multiplets. Once again the starting parameters were those obtained from $PbMoO_4:Nd^{3+}$. Two sets of parameters result which give the same r.m.s. deviation of 6.7 cm^{-1}. The two sets of parameters were found to correspond to different choices of x and y axes. The local symmetry at the Pr^{3+} site fixes only the z axis and leaves the remaining axes unspecified in the x-y plane. The two sets of parameters are related by the following transformation equation[11]

$$\left(B^k_{(\pm q)}\right)' = B^k_{(\pm q)} \cos(q\phi) + B^k_{(\mp q)} \sin(\pm q\phi) \qquad (4.4)$$

where $\left(B^k_{(\pm q)}\right)'$ refers to the parameters in a coordinate system rotated anticlockwise through the angle ϕ about z axis with respect to the frame with parameters $B^k_{(\pm q)}$. The axial parameters B^2_0, B^4_0 and B^6_0 remain invariant under such a rotation of coordinates as they are independent of the choice of x and y axes. The two parameter sets for this fit along with the calculated and experimental energy differences are listed in Table IV.4. These parameter sets are related by the rotation of 9.3°

TABLE IV-4

Crystal-Field Parameters Corresponding to Seven Parameters Fit[*]
for Eleven Stark Components of $^3H_4$, $^3F_3$ and $^1D_2$ Multiplets

Set A

$B_0^2 = 235.77 \pm 2.29$ cm^{-1} ; $B_0^4 = -648.74 \pm 5.55$ cm^{-1} ;

$B_0^6 = -27.64 \pm 8.26$ cm^{-1} ; $B_4^4 = -1031.7 \pm 4.89$ cm^{-1} ;

$B_4^6 = -628.93 \pm 28.9$ cm^{-1} ; $B_4'^4 = 140.35 \pm 32.77$ cm^{-1} ;

$B_4'^6 = -864.48 \pm 21.68$ cm^{-1}

Set B

$B_0^2 = 235.77 \pm 2.29$ cm^{-1} ; $B_0^4 = -648.74 \pm 5.54$ cm^{-1} ;

$B_4^4 = -906.86 \pm 27.35$ cm^{-1} ; $B_4^6 = 21.26 \pm 58.23$ cm^{-1} ;

$B_0^6 = -27.63 \pm 8.25$ cm^{-1} ; $B_4'^4 = -511.63 \pm 48.99$ cm^{-1} ;

$B_4'^6 = -1068 \pm 6.56$ cm^{-1}

Both Sets of Parameters give Identical Stark Splittings(given below):

Multiplet	Stark Component	Calculated Stark Splittings a (cm^{-1})	Experimental Stark Splittings b (cm^{-1})	Difference c = (a-b) (cm^{-1})
$^3H_4$	Γ_2	0	0	0
	Γ_3	64.87	61	3.87
	Γ_1	123.4	131	-7.6
	Γ_1	222.6	–	–
	Γ_3	393.96	398	-4.04
	Γ_2	429.4	–	–
	Γ_1	455.3	–	–

TABLE IV-4 (contd.)

Multiplet	Stark Component	Calculated Stark Splittings a (cm^{-1})	Experimental Stark Splittings b (cm^{-1})	Difference c = (a-b) (cm^{-1})
$^3F_3$	Γ_3	0	0	0
	Γ_2	-25.17	-	-
	Γ_1	36.47	-	-
	Γ_2	103.41	92	11.41
	Γ_3	108.01	121	-13.01
$^1D_2$	Γ_2	0	0	-
	Γ_1	46.28	49	-2.72
	Γ_3	236.60	238	-1.4
	Γ_2	447.84	444	3.84

r.m.s. deviation = 7 cm^{-1}

---

*Free-ion parameters given in Table IV-1 were used.
Initial values of crystal field parameters were derived
from those given in Ref. 12 for $PbMoO_4$:Nd^{3+} following
the procedure outlined in Section 3 of the Chapter III.

about the z axis. The values of four parameters B_0^2, B_0^4, B_4^4, $B_4'^4$ are fairly close to those obtained from the four parameters fit for $^1D_2$ level. At this stage the eighteen energy differences from $^3H_4$, $^3F_4$, $^3H_6$, $^3F_2$, $^1D_2$, $^3P_2$, $^3F_3$ multiplets were included in the least squares calculations. The starting parameters were those given in Table IV-4. Both sets of initial parameters converge to the same final set of parameters. Final parameters are given in Table IV-5 along with the calculated and experimental energy differences. The r.m.s. deviation is 22 cm^{-1}. Free-ion C.G.'s were re-estimated at this point and a least squares fit for 8 free-ion energies was again carried out. Final free-ion parameters which yield an r.m.s. deviation of 12 cm^{-1} are given in Table IV-6 along with the calculated and estimated C.G.'s. Intermediate coupling wavefunctions calculated with these parameters are given in Table IV-7. Using these refined 'free-ion' parameters, least squares fit for crystal field energy differences was repeated. Results of this fit along with the parameters are given in Table IV-8. Free-ion C.G.'s were restimated but no appreciable change occured. It can be seen here that the values of $B_q'^k$ are very large compared to those reported in Ref. 1 for Nd^{3+} (cf Table IV-9). This indicates the relevance of S_4 symmetry in case of Pr^{3+}. It is to

TABLE IV-5

Crystal Field Parameters for least squares Fit* to 25 Stark
Components of $^3H_{4,6}$, $^3F_{2,3,4}$, $^1D_2$, $^3P_2$ Multiplets.

$B_0^2 = 226.44 \pm 1.59$ cm^{-1}; $B_0^4 = -462.25 \pm 4.31$ cm^{-1}; $B_0^6 = -87.78 \pm 6.06$ cm^{-1}

$B_4^4 = -946.44 \pm 47.6$ cm^{-1}; $B_4^6 = -196.88 \pm 108.65$ cm^{-1};

$B_4'^4 = -409.01 \pm 110.26$ cm^{-1}; $B_4'^6 = -931.07 \pm 23.40$ cm^{-1}.

Multiplet	Stark Component	Calculated Stark Splittings a (cm^{-1})	Experimental Stark Splittings b (cm^{-1})	Difference c = (a-b) (cm^{-1})
$^3H_4$	Γ_2	0	0	0
	Γ_3	73.94	61	12.94
	Γ_1	124.84	131	-6.1
	Γ_1	199.59	-	-
	Γ_3	383.58	398	-14.42
	Γ_1	405.58	-	-
	Γ_2	423.22	-	-
$^3F_4$	Γ_3	0	0	0
	Γ_2	-4.56	25	-29.56
	Γ_1	13.9	-	-
	Γ_1	144.03	132	12.03
	Γ_2	179.86	-	-
	Γ_3	189.62	173	16.62
	Γ_1	262.89	232	30.89
$^3H_6$	Γ_2	0	0	0
	Γ_3	60.70	47	13.7
	Γ_1	104.24	77	27.24
	Γ_2	188.24	-	-

TABLE IV-5 (contd.)

Multiplet	Stark Component	Calculated Stark Splittings a (cm^{-1})	Experimental Stark Splittings b (cm^{-1})	Difference c = (a-b) (cm^{-1})
	Γ_1	194.23	-	-
	Γ_3	203.00	236	-33
	Γ_2	290.35	-	-
	Γ_1	450.75	-	-
	Γ_3	505.87	-	-
	Γ_2	564.53	-	-
$^3F_2$	Γ_2	0	0	0
	Γ_3	-4.39	9	13.39
	Γ_1	3.382	-	-
	Γ_2	63.29	-	-
$^1D_2$	Γ_2	0	0	0
	Γ_1	71.79	49	22.79
	Γ_3	213.2	238	-24.8
	Γ_2	443.5	444	--0.5
$^3P_2$	Γ_1	0	0	0
	Γ_3	43.6	-	-
	Γ_2	64.79	-	-
	Γ_2	143.0	148	-5.0
$^3F_3$	Γ_3	0	0	0
	Γ_2	-19.88	25	-44.8
	Γ_1	26.7	-	-
	Γ_2	90.41	92	-1.59
	Γ_3	99.24	121	-21.76

r.m.s Deviation = 22 cm^{-1}.

*

TABLE IV-7

Intermediate Coupling Wavefunctions

(a) for the Free-ion Parameters Set Given in Table IV-1

J	Eigen Values	Basis States		
		$^1S_0$	$^3P_0$	
0	57502	0.9976	−0.0687	
	2 266	0.0687	0.9976	
		$^3P_1$		
1	20810	1.000		
		$^1D_2$	$^3F_2$	$^3P_2$
2	22031	0.2952	−0.0315	0.9549
	16576	0.9433	−0.1488	−0.2966
	4861	0.1515	0.9883	−0.0142
		$^3F_3$		
3	6243	1.000		
		$^1G_4$	$^3H_4$	$^3F_4$
4	9616	0.7974	−0.1142	0.5925
	6699	−0.5808	0.1207	0.8050
	0.0	0.1634	0.9861	−0.0298
		$^3H_5$		
5	2065	1.000		
		$^1I_6$	$^3H_6$	
6	21146	0.9986	0.0534	
	4227	−0.0534	0.9986	

contd.

TABLE IV-7 (contd.)

(b) <u>for the Free-ion Parameters Set Given in Table IV-6</u>

J	Eigen Value	Basis States		
		$^1S_0$	$^3P_0$	
0	94832	0.9993	-0.0353	
	20268	0.0353	0.9993	
		$^3P_1$		
1	20738	1.000		
		$^1D_2$	$^3F_2$	$^3P_2$
2	42004	0.3031	-0.0331	0.9523
	16546	0.9402	-0.1518	-0.3046
	4800	0.1547	0.9878	-0.0148
		$^3F_3$		
3	6223	1.000		
		$^1G_4$	$^3H_4$	$^3F_4$
4	9678	0.7967	-0.1163	0.5929
	6690	-0.5807	0.1241	0.8046
	0.0	0.1672	0.9854	-0.313
		$^3H_5$		
5	2123	1.0000		
		$^1I_6$	$^3H_6$	
6	20762	0.9984	0.0564	
	4336	-0.0564	0.9984	

TABLE IV-8

Crystal Field Parameters Corresponding to the Least-Squares
Fit[*] for 26 Stark Components of $^3H_{4,6}$, $^3F_{2,3,4}$, $^1D_2$, $^3F_2$

$B_0^2 = 222.6 \pm 1.59$ cm^{-1}; $B_0^4 = -463.48 \pm 4.35$ cm^{-1} ;

$B_0^6 = -81.65 \pm 6.09$ cm^{-1} ; $B_4^4 = -951.38 \pm 52.77$ cm^{-1} ;

$B_4^6 = -183.07 \pm 118.51$ cm^{-1} ; $B_4'^4 = -417.72 \pm 120.17$ cm^{-1}
$B_4'^6 = -936.98 \pm 23.5$ cm^{-1}

Multiplet	Stark Component	Calculated Stark Splittings a (cm^{-1})	Experimental Stark Splittings b (cm^{-1})	Difference c = a-b (cm^{-1})
$^3H_4$	Γ_2	0	0	0
	Γ_3	72.6	61	11.6
	Γ_1	125.0	131	-6.0
	Γ_1	202.3	–	–
	Γ_3	384.1	398	-13.9
	Γ_1	407.6	–	–
	Γ_2	423.8	–	–
$^3F_4$	Γ_3	0	0	0
	Γ_2	-4.9	25	-29.9
	Γ_1	16.5	–	–
	Γ_1	145.3	132	13.3
	Γ_2	181.6	–	–
	Γ_3	190.5	173	17.5
	Γ_1	263.8	232	-31.8
$^3H_6$	Γ_2	0	0	0
	Γ_3	60	47	13
	Γ_1	103.5	77	26.5
	Γ_2	191.1	–	~

TABLE IV-8 (contd.)

Multiplet	Stark Component	Calculated Stark Splittings a (cm^{-1})	Experimental Stark Splittings b (cm^{-1})	Difference c = a-b (cm^{-1})
	Γ_1	194.8	—	—
	Γ_3	203.6	236	-32.4
	Γ_2	294.8	—	—
	Γ_1	451.9	—	—
	Γ_3	507.5	—	—
	Γ_2	567.1	—	
$^3F_2$	Γ_2	0	0	0
	Γ_3	-4.2	9	-13.2
	Γ_1	3.4	—	—
	Γ_2	62.5	—	—
$^1D_2$	Γ_2	0	0	0
	Γ_1	73	49	24.0
	Γ_3	213	238	-25.0
	Γ_2	441.7	444	-2.3
$^3P_2$	Γ_1	0	0	0
	Γ_3	44.4	—	—
	Γ_2	61.6	—	—
	Γ_2	142.4	148	-5.6
$^3F_3$	Γ_3	0	0	0
	Γ_2	-19.8	25	-44.8
	Γ_1	27.6	—	—
	Γ_2	91.1	92	-0.9
	Γ_3	99.4	121	-21.6

r.m.s. Deviation = 22 cm^{-1}

*Free-ion Parameters given in Table IV-6 were used for this fitting and initial crystal field parameters were those given in Table IV-5

TABLE IV-9

Comparison of Crystal Field Parameters

Ion	Host	Crystal Field Parameters (cm^{-1})							r.m.s. Dev. cm^{-1}
		B_0^2	B_0^4	B_0^6	B_4^4	B_4^6	$B_4'^4$	$B_4'^6$	
Pr^{3+} :	$PbMoO_4$[a]	226.6	-463.48	-81.55	-951.38	-123.07	-417.7	-936.98	22.0
Pr^{3+} :	$LiYF_4$[b]	488.9	-1043.0	-42.0	1242.0	1213.0	--	22.5	15.0
Nd^{3+} :	$PbMoO_4$[c]	432.1	-583.6	-101.6	-933.4	-683.0	206.0	-43.2	11.90
		432.5	-605.0	-102.4	-919.6	-692.9	2.4	-35.5	12.3

a — present work

b — taken from Ref. 6

c — taken from Ref. 12

be noticed here that the r.m.s. deviation of 22 cm^{-1}
is quite large. Similar r.m.s. deviations for Pr^{3+}
ion have been reported in the literature . Further,
for some multiplets the calculated and experimental
order of energy levels does not agree e.g. $^3F_2$ (Γ_3)
is higher than $^3F_2$ (Γ_2), whereas calculations show it
otherwise. If one looks at the relative separation of
various lowlying multiplets (e.g. $^3H_6$, $^3F_2$, $^3F_3$ and
$^3F_4$ etc.) and their crystal field splittings, it is
evident that the assumption of neglecting J-J mixing
is not well justified atleast for these multiplets. In
the following discussion we have tried to estimate the
extent of J-J mixing present amongst various multiplets.

2.3 J-J Mixing

Crystal field energy matrices for Γ_1 , Γ_2 and Γ_3
representations involving levels of $^3H_6$, $^3F_2$, $^3F_3$ and
$^3F_4$ multiplets were diagonalized with the parameters of
Table IV-5. The results are shown in Table IV.10. We
notice here that the order of the lowest two levels of
$^3F_2$ is reversed bringing it in agreement with the experi-
mental results. Similar improvement is seen for $^3F_3$
multiplets. But the situation for $^3F_4$ becomes worse.
A careful look at the intermediate coupling wavefunctions
for $^3F_4$ readily provides an explanation for this discre-
pancy. The wavefunctions for the $^3F_4$ multiplet have

TABLE IV-10

Energy level calculations for $^3H_6$, $^3F_2$, $^3F_3$, $^3F_4$ multiplets with J-J mixing using the parameters of Tables IV-1 and IV-5.

Multiplet	Stark Component	Calculated Stark Splittings (cm^{-1})		Experimental Stark Splittings (cm^{-1})
		with J-J Mixing	without J-J Mixing	
$^3H_6$	Γ_2	0	0	0
	Γ_3	79	60.7	47
	Γ_1	142	104.24	77
	Γ_2	172	188.24	~
	Γ_3	228	203.0	236
	Γ_1	234	194.23	~
	Γ_2	282	290.35	~
	Γ_1	464	450.75	~
	Γ_3	509	505.87	~
	Γ_2	559	564.53	~
$^3F_2$	Γ_2	0	0	0
	Γ_1	10	3.382	~
	Γ_3	17	-4.39	9
	Γ_2	98	63.29	~
$^3F_3$	Γ_3	0	0	0
	Γ_2	-1	-19.88	25
	Γ_1	11	26.7	~
	Γ_3	97	99.24	121
	Γ_2	133	90.41	92

TABLE IV-10 (contd.)

Multiplet	Stark Component	Calculated Stark Splittings (cm^{-1})		Experimental Stark Splittings (cm^{-1})
		with J–J Mixing	without J–J Mixing	
$^3F_4$	Γ_3	0	0	0
	Γ_2	–10	–4.56	25
	Γ_1	30	13.9	–
	Γ_1	101	144.03	132
	Γ_2	135	179.86	–
	Γ_3	108	189.62	173
	Γ_1	111	262.89	232

large mixing from $^1G_4$. We are therefore not justified
in diagonalizing the $^3F_4$ and $^1G_4$ matrices separately.
To do full justice to these calculations one must carry
out a least squares fit including J-J mixing. However,
due to sparsity of available experimental data such an
attempt can not be justifiably made. Still the effect
of J-J mixing is clearly demonstrated. It is therefore,
desirable to obtain more complete experimental results.
Calculations including J-J mixing completely will not
be formidable for this system. Since the Stark split-
tings for $PbMoO_4:Pr^{3+}$ are comparable, no separate cal-
culations for $PbWO_4:Pr^{3+}$ are needed.

3.   RAMAN SPECTRA OF $PbMoO_4$ AND $PbWO_4$ SINGLE CRYSTALS

Raman spectra of $PbMoO_4$ (cf Fig. II-22 - 23) and
$PbWO_4$ (cf Fig. II-24$^{-25}_\lambda$) single crystals have been analysed
following the approach outlined in sec. 4 of chapter III.
Details of the analysis are given below :

3.1   Selection Rules

The structure of $PbMoO_4$ and $PbWO_4$ single crys-
tals has been described in sec. 4 of chapter II. It
may be recalled here that these crystals have the
point group symmetry C_{4h} and space group symmetry I_4 $_1/a$
The unit cell has four formula units. The molecules

at the body centre are related to the molecules at the corner of the unit cell by the simple translations operations. Thus the primitive cell has only two formula units with 12 atoms. There are 36 degrees of freedom. The isolated tetrahedral unit XO_4^{2-} has T_d symmetry and its vibrations span the representations $A+E+2F_2$. In the lattice each X atom occupies S_4 site and there are two XO_4^{2-} units per primitive cell. Thus each representation of S_4 must cover vibrations from both XO_4^{2-} units. Site and factor group splittings of the vibrational modes of XO_4^{2-} units are shown in the correlation table IV-11(a). It is seen from here that the internal vibrations of the two XO_4^{2-} units will span the C_{4h} group representations

$$2A_g + 3B_g + 2E_g + 3A_u + 2B_u + 2E_u$$

The species with the subscript g are Raman active and those with the subscript u are IR active. Table IV-11(b) gives the site and factor group splittings of the external modes (Rotational and Translational) involving the motions of the rigid XO_4^{2-} units. The rotational modes span the C_{4h} point group representations

$$A_g + E_g + B_u + E_u$$

and external modes of XO_4^{2-} cover

$$B_g + E_g + A_u + E_u$$

TABLE IV-11 a

Site and Factor Group Splittings of the Vibrations of XO_4^{2-} Unit.

	T_d	S_4	C_{4h}	
X-O Symm. Stretching	ν_1 A	A	A_g	$\alpha_{xx}+\alpha_{yy}$, α_{zz}
XO_4 deg. bend.	ν_2 E	B	B_g	$\alpha_{xx}-\alpha_{yy}$, α_{xy}
X-O asymm. bend.	$\nu_3 (F_2)$	E	E_g	α_{yz} , α_{zx}
XO_4 asymm. bend.	$\nu_4 (F_2)$		B_u	
			A_u	
			E_u	
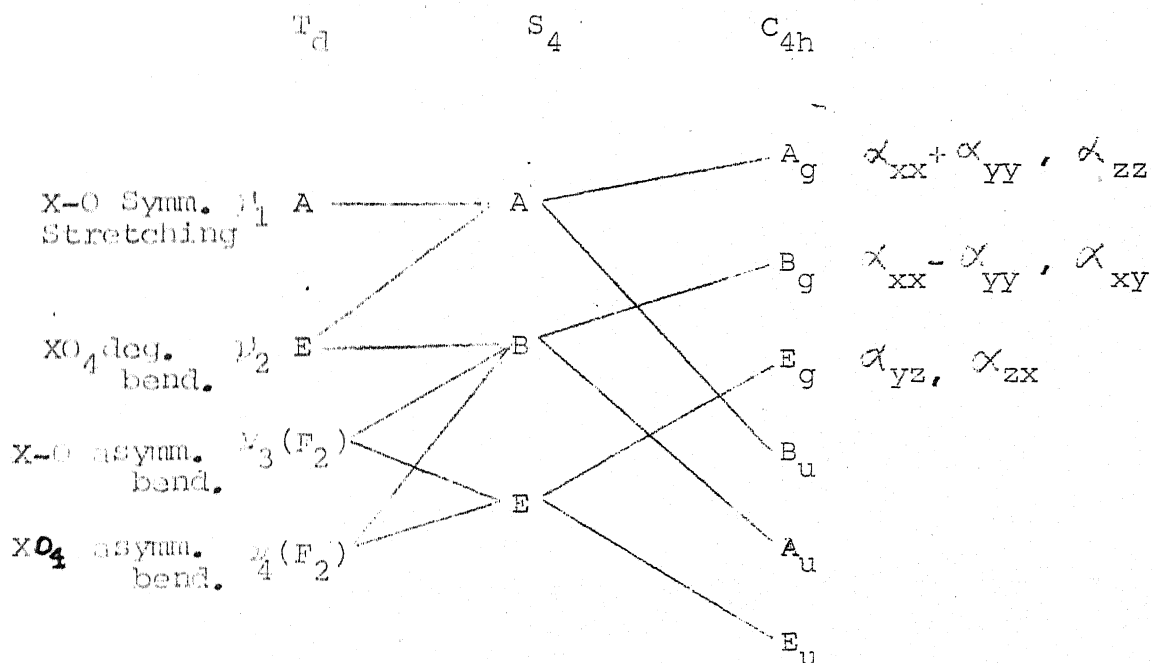
TABLE IV-11(b)

Site and Factor Group Splitting of External Modes of XO_4^{2-} Units.

T_d	S_4	C_{4h}

Rotation $\quad F_1 \quad$ — $\quad A$

Translation $\quad F_2 \quad$ B

E

A_g

B_g

E_g

B_u

A_u

E_u
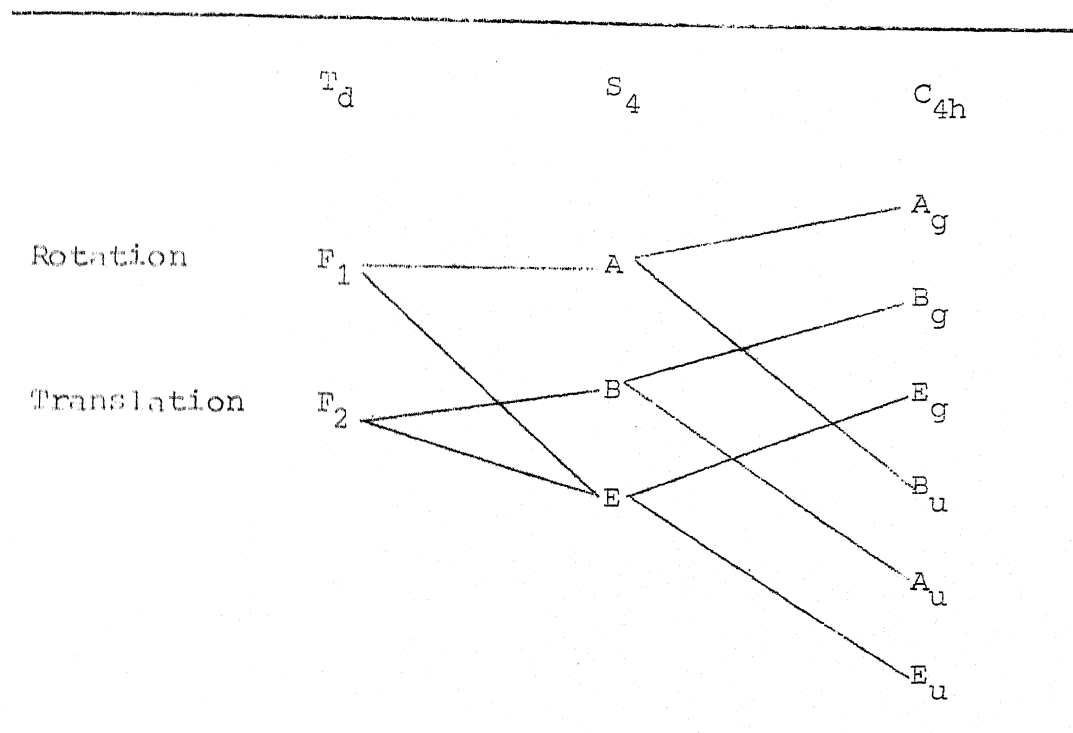
TABLE IV-11(c)

Correlation Table for the Translational Modes of Pb^{2+} Ions

S_4	C_{4h}

A

$T_z \quad B$

$(T_x, T_y) \quad E$

B_g

E_g

A_u

E_u
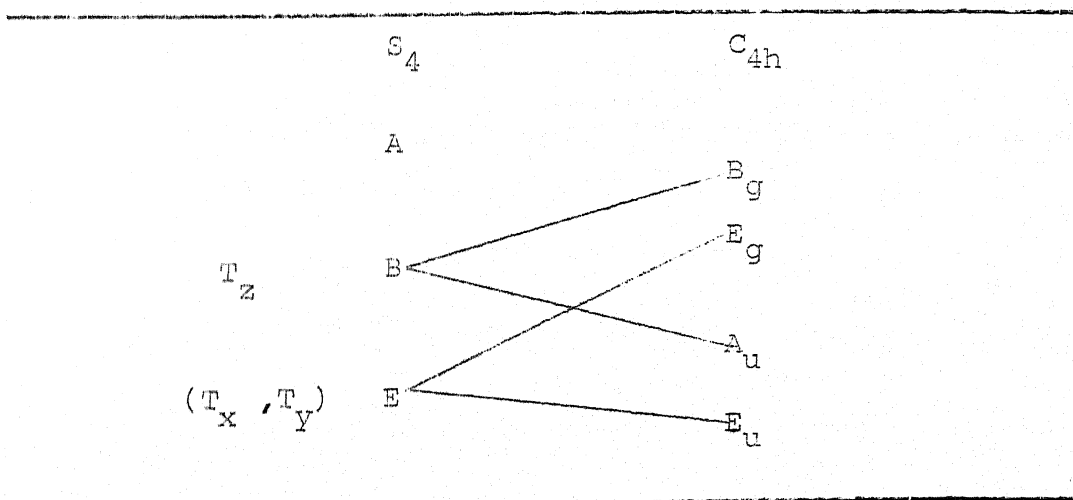
The external modes of two Pb^{2+} ions occupying the S_4 site also have the same distribution among irreducible representations of C_{4h} as that of XO_4^{2-} units (cf Fig. IV-11(c)). Thus the 26 modes of two formula units in the primitive cell are distributed into the irreducible representations of C_{4h} as below

$$3A_g + 5B_g + 5E_g + 5A_u + 3B_u + 5E_u$$

3.2 Symmetry Assignments

The polarizability tensors are given below :

$$A_g : \begin{pmatrix} \alpha_{xx} & 0 & 0 \\ 0 & \alpha_{yy} & 0 \\ 0 & 0 & \alpha_{zz} \end{pmatrix} ; \quad B_g : \begin{pmatrix} \alpha_{xx} & \alpha_{xy} & 0 \\ \alpha_{yx} & -\alpha_{yy} & 0 \\ 0 & 0 & 0 \end{pmatrix}$$

$$E_g : \begin{pmatrix} 0 & 0 & \alpha_{xz} \\ 0 & 0 & \alpha_{yz} \\ \alpha_{zx} & \alpha_{zy} & 0 \end{pmatrix}$$

It becomes evident from here that measurement of α_{zz} will yield only A_g type vibrations; measurement of α_{xz} will yield only E_g vibrations, measurement of α_{xy} will yield only B_g vibrations and that of α_{yy} will give $A_g + B_g$ vibrations. From these considerations the symmetries of the observed lines could be readily

assigned on the basis of their relative intensities (cf Table II-11 and 12) in various geometries. Though the three A_g modes have α_{xx}, α_{yy} and α_{zz} nonzero in the x(zz)y geometry only two $\nu_1(A_g)$ band (at 905 cm^{-1} for PbWO$_4$ and at 871 cm^{-1} for PbMoO$_4$) and $\nu_2(A_g)$ band (at 319 cm^{-1} for PbMoO$_4$ and at 328 cm^{-1} for PbWO$_4$) appear while the third one corresponding to the rotation (F_1) about z-axis does not appear here. This appears in the x(yy)z geometry. Apparently, the dipole matrix element for this mode in x(zz)y geometry should be small. All the bands could be assigned unambiguously. The observed Raman active internal and external modes of PbMoO$_4$ and PbWO$_4$ single crystals are listed in Tables IV-12 and IV-13 along with their symmetry assignments, respectively. This table also provides a comparison with earlier works[13-14] on these and other similar crystals. According to Khanna et al[13], the two bands $\nu_2(A_g)$ and $\nu_2(B_g)$ are degenerate in PbWO$_4$ and show correlation field splitting of 3 cm^{-1} in PbMoO$_4$ crystals. We observe the correlation field splitting of 3 cm^{-1} in PbWO$_4$ and 1 cm^{-1} in PbMoO$_4$ for these bands. Further, the band $\nu_2(A_g)$ appears with the higher frequency than $\nu_2(B_g)$ band. This is not in agreement with earlier works on these and other similar crystals[13-14]. Correlation field splitting for $\nu_4(B_g)$ and $\nu_4(E_g)$ bands of only 2 cm^{-1} is seen here for both

$PbMoO_4$ and $PbWO_4$ crystals while Khanna et al. have reported a splitting of 8 cm^{-1} in $PbMoO_4$ and 5 cm^{-1} in $PbWO_4$ crystals. The two bands which appear at the same frequencies 61 cm^{-1} (E_g) and 75 cm^{-1} (B_g) in both $PbMoO_4$ and $PbWO_4$ crystals should correspond to the motion of Pb^{2+} ions in x-y plane and along z-direction respectively. The other two external modes at 64 cm^{-1} (B_g) and 104 cm^{-1} (E_g) in $PbMoO_4$ (at 52 cm^{-1} (B_g) and 88 cm^{-1} (E_g) in $PbWO_4$) will belong to the translations of XO_4^{2-} units. All observed Raman lines are in accordance with the group theoretical predictions except one extra line appearing at 54 cm^{-1} (B_g) in both $PbMoO_4$ and $PbWO_4$ crystals. Origin of this line is not clear.

Assignments of $(XO_4)^{2-}$ Vibrational Modes in Scheelites

Vibration Modes and Their Symmetry		Vibrational Frequencies (cm^{-1})							
Isolated Tetrahedron T_d	Tetrahedron in Lattice C_{4h}	$PbMoO_4$[a]	$PbWO_4$[a]	$PbMoO_4$[b]	$PbWO_4$[b]	$CaMoO_4$[c]	$CaWO_4$[c]	$SrMoO_4$[c]	$SrWO_4$[c]
$\nu_1(2A_1)$	$\nu_1(A_g)$	871	905	868	900	878	912	887	925
	$\nu_1(B_u)$[d]								
$\nu_3(2F_2)$	$\nu_3(A_u)$[d]								
	$\nu_3(B_g)$	768	766	764	764	844	838	842	839
	$\nu_3(E_g)$	744	753	744	748	797	797	797	797
	$\nu_3(E_u)$[d]								
$\nu_4(2F_2)$	$\nu_4(A_u)$[d]								
	$\nu_4(B_g)$	348	358	348	348	393	401	367	370
	$\nu_4(E_g)$	350	360	356	353	401	409	381	378
	$\nu_4(E_u)$[d]								
$\nu_2(2E)$	$\nu_2(A_g)$	319	328	314	322	333	336	327	334
	$\nu_2(B_g)$	318	325	317	322	339	336	327	334
	$\nu_2(A_u)$[d]								
Rotation $(2F_1)$	B_u[dd]								
	A_g	167	178	164	178	205	218	181	187
	E_g[d]	191	193	190	187	263	275	131	238
	E_u[d]								

a — present work
b — Ref. 13
c — Ref. 14
d — Forbidden (Infrared active)

TABLE IV-13

Identification of External Vibrations in Single Crystals of Scheelites

Symmetry	Frequency (cm^{-1})							
	$PbMoO_4$ [a]	$PbWO_4$ [a]	$PbMoO_4$ [b]	$PbWO_4$ [b]	$CaMoO_4$ [c]	$CaWO_4$ [c]	$SrMoO_4$ [c]	$SrWO_4$ [c]
E_g	62	62	61	61	145	117	111	101
B_g	65	52	64	52	110	84	94	75
E_u [d]								
A_u [d]								
B_g	74	76	75	76	219	210	157	—
E_g	102	89	100	86	189	195	137	131

a = Present work

b = Ref. 13

c = Ref. 14

d = Forbidden (infrared active)

REFERENCES

1. I.S. Minhas, K.K. Sharma, J.B. Gruber, Phys. Rev. B. $\underline{8}$, 385 (1973).

2. G.H. Dieke, Spectra and Energy Levels of Rare Earth Ions in Crystals, Interscience Publishers, 1968, p.55.

3. Ref. 2, p. 193

4. Ref. 2, p. 17.

5. Ya.E. Kariss and P.P. Feofilov, Opt. Spectry. $\underline{17}$, 387 (1

6. L. Esterowitz, F.J. Bartoliand R.E. Allen, Phys. Rev. B, $\underline{19}$, 6442 (1979).

7. E.G. Reut and A.I. Ryskin, Opt. Spectrosk. $\underline{35}$, 501 (1973

8. A.M. Morozov, E.G. Reut and A.I. Ryskin, $\underline{21}$, 314 (1966).

9. W.T. Carnall, P.R. Fields and K.J. Rajnak, J. Chem. Phys $\underline{49}$, 4424 (1968).

10. D.A. Wensky and W.G. Moulton, The J. of Physics, $\underline{53}$, 3957 (1970).

11. Jaochim Stohr, David. N. Olsen and John B. Gruber, Jl. of Chem. Phys. $\underline{55}$, 4463 (1971).

12. I.S. Minhas – A Study of the Optical Properties of $Nd^{3+}:PbMoO_4$ System – Ph.D. Dissertation.

13. R.K. Khanna, W.S. Brower, B.R. Guscott and E.R. Lippinco J. of Research of the National Bureau of Standards – A. Physics and Chemistry $\underline{72A}$ (1968).

14. S.P.S. Porto and J.F. Scott, Phys. Rev. $\underline{157}$ 716 (1967)

CHAPTER V

CONCLUSIONS

In the present work we have attempted to interpret the fluorescence, absorption and vibrational spectra of $PbMoO_4$ and $PbWO_4$ single crystals doped with Nd^{3+} and Pr^{3+}. We have assumed here that Nd^{3+} and Pr^{3+} substitute for Pb^{2+}. The site symmetry at this site is S_4. The symmetry assignments of the Raman active vibrations in $PbMoO_4$ and $PbWO_4$ crystals are in agreement with earlier works on these and other similar crystals. These samples when excited by the blue lines of Ar^+ ion laser showed very strong fluorescence which does not agree with the known energy level scheme of Nd^{3+}. The visible fluorescence has been attributed to Pr^{3+} ions while the near IR region fluorescence is due to both Nd^{3+} and Pr^{3+} ions. The estimated concentration of Pr^{3+} in these crystals is less than a ppm. In the near IR region very weak fluorescence of Nd^{3+} from $^4F_{3/2}$ multiplet to eleven low lying levels of $^4I_{9/2}$ and $^4I_{11/2}$ multiplets have been observed. The positions of observed Nd^{3+} fluorescence transitions are in fair agreement with the earlier work of Kariss and Feofilo . Crystal field calculations for Nd^{3+} ion in $PbMoO_4$ crystal have been done in the past and the spectra are well understood. Therefore, we have not attempted

any energy level calculations for Nd^{3+}. Fluorescence from $^3P_0$ and $^1D_2$ multiplets of Pr^{3+} ion to low lying $^3H_{4,5,6}$, $^3F_{2,3,4}$ and $^1G_4$ multiplets has been observed. From the absorption and fluorescence data, a total of 33 levels of Pr^{3+} in $PbMoO_4$ and 19 Pr^{3+} levels in $PbWO_4$ have been obtained. In case of Pr^{3+} many Stark components could not be obtained because the transitions to these levels were either not allowed or very weak. The weak transitions may become observable if Pr^{3+} concentration in the crystals is increased. This is supported by our limited study on concentration effects. These studies need to be extended. Some of the lines, in particular the one at 9998 cm^{-1} could not be identified. Such problems can be resolved if dye laser is used for selective excitation of fluorescence.

For Pr^{3+} only a preliminary analysis has been carried out by Reut et al. They have determined the values of B_0^2, B_0^4, B_4^4 parameters using the Stark splittings of $^1D_2$ multiplet only. They have assumed D_{2d} symmetry at Pr^{3+} site for this analysis. In this work we undertook detailed theoretical energy level calculations for Pr^{3+} ion in these hosts. The quantities which could not be obtained from ab-initio calculations were parameterized. Empirical values of these parameters are

obtained by the method of least squares fit. Energy
level calculations for $PbWO_4:Pr^{3+}$ have not been attempted
in this work. We expect the crystal field parameters of
$PbWO_4:Pr^{3+}$ to be somewhat similar to $PbMoO_4:Pr^{3+}$ parameters.
The bulk of the energy level calculations for $PbMoO_4:Pr^{3+}$
have been performed without J-J mixing. The calculations
are done in two stages. In the first stage the free ion
energy eigenvalue problem has been solved in the inter-
mediate coupling scheme. The 'free ion' Hamiltonian
included electrostatic, spin-orbit and configuration
interactions. This entails the parameterization of the
following quantities E^1, E^2, E^3, ζ_{4f}, α, β and γ. A
least squares fit to the estimated c.g's of eight Pr^{3+}
multiplets ($^3H_{4,6}$, $^3F_{2,3,4}$, $^1D_2$ and $^3P_{0,2}$) in $PbMoO_4$
host was carried out to determine these parameters. The
resulting parameters yielded an R.M.S. deviation of 16 cm^{-1}.
In the second stage of calculations, the crystal field
interaction, which is treated as a small perturbation
to the free ion Hamiltonian is brought in. A four para-
meter fit to the Stark splittings of $^1D_2$ multiplet yielded
an R.M.S. deviation of 8 cm^{-1}. The resulting crystal
field parameters B_0^2, B_0^4 and B_4^4 did not agree to the
corresponding values reported by Reut et al. A seven
parameter least squares fit to 11 levels of $^3H_4$, $^1D_2$
and $^3F_3$ multiplets yielded two sets of parameters giving

the same "r.m.s." deviation of 7 cm^{-1}. These sets of parameters were found to correspond to different choices of x and y axes which are not fixed by the site symmetry. The axial parameters B_0^2, B_0^4 and B_0^6, however, remain invariant as they are independent of the choice of x and y axis. The two sets of parameters are equivalent as they give identical "r.m.s." deviation. These calculations were further extended to include 25 levels of $^3H_{4,6}$, $^3F_{2,3,4}$, $^1D_2$, $^3P_2$ multiplets of Pr^{3+}. The resulting B_q^k parameters gave an R.M.S. deviation of 22 cm^{-1}. The free ion C.G.'s were reestimated at this point and the free ion parameters refined to yielding an R.M.S. deviation of 12 cm^{-1}. The crystal field calculations for 25 levels were repeated with these refined free ion parameters but the fit did not improve any further. A comparison of $B_q'^k$ parameters for Pr^{3+} and Nd^{3+} in this host indicates the relevance of S_4 symmetry for Pr^{3+} ion. The theoretically predicted order of some levels in $^3F_{2,3,4}$ multiplets is not in accordance with the experimental results. It has been demonstrated that the cause of such discrepancy is the neglect of J-J mixing in our calculations. An attempt to estimate the extent of J-J mixing was made. The energy matrix for the Hamiltonian including both free ion and crystal field interactions was solved using the free ion and crystal field parameters

from the above calculations. It has been shown that the inclusion of J-J mixing effects can alter the level positions by as much as 25 cm^{-1}. One can expect greater correspondence between theory and experiments if the least square analysis is done including J-J mixing. Such calculations could not be performed here due to insufficient experimental data.

In conclusion, we believe that these studies help us towards a better theoretical understanding of the role of various interactions in the Pr^{3+} spectra. The observation of such strong visible fluorescence from such dilute samples of Pr^{3+} speaks for its high quantum efficiency which is an important requirement for efficient laser materials. Further, studies on quantum efficiency and lifetime measurements can be done to determine the potential of these materials for laser applications. Lifetime measurements will also be helpful in understanding the $^3P_0 - {}^1D_2$ relaxation.

APPENDIX I

DOUBLE MONOCHROMATOR GDM1000

This double monochromator employs two autocollimated monochromators, each with a concave mirror and a grating (651 lines/mm) in Littrow arrangement, placed one behind the other so that the dispersion of gratings are added and coma aberration of mirrors anulled. This results in an outstandingly sharp image of the entrance slit in the outlet slit plane which is free from coma. Other image aberrations (e.g. spherical, astigmatism etc.) are negligible due to the chosen focal length of the mirrors (f = 1100 mm, aperture ratio 1:10.4) and the small angle of incidence of rays on the concave mirror. A field flattening lens in front of the outlet slit is used to compensate for

(1) the curvature of the field arising from the concave mirrors

(2) wavenumber dependence of line curvature

Field flattening lens forms an image of the aperture area at a distance of 235 mm behind the outlet slit. The monochromator has a built in 25 cps chopper and an automarking generator.

APPENDIX I

CALIBRATION CHART

Source used for calibration : Ne discharge tube

Spectral region 23000-17000 cm^{-1} (IInd order)

Standard Wave No. (cms^{-1})	Observed on GDM1000 (cms^{-1})
1. 22037.33	22034
2. 21256.71	21253
3. 21236.55	21233
4. 21231.55	21228
5. 21222.11	21219
6. 21207.35	21205
7. 20881.52	20878
8. 20715.32	20712
9. 20471.17	20468
10. 20173.35	20170
11. 18758.98	18756
12. 18722.75	18719
13. 18715.08	18712
14. 18516.59	18513
15. 17347.8	17344
16. 17086.75	17083
17. 17001.32	16998

APPENDIX I

CALIBRATION CHART

Source used for calibration : Ne discharge tube
Spectral region 17000-11000 cm^{-1} (Ist order)

Sl.No.	Standard Wave No. (cm^{-1})	Observed on GDM1000 (cm^{-1})
1.	16734.9	16734
2.	16583.75	16583
3.	16462.7	16462
4.	16224.7	16223.5
5.	16084.2	16084
6.	15957.88	15957
7.	15786.74	15786
8.	15666.68	15666
9.	15619.51	15619
10.	15154.21	15153.5
11.	14431.123	14430.5
12.	14219.87	14219.5
13.	13939.345	13939
14.	13802.305	13802
15.	12047.721	12047
16.	11936.583	11936
17.	11771.132	11771
18.	11581.249	11581
19.	11554.837	11554
20.	11521.41	11522
21.	11518.18	11519
22.	11279.35	11280

APPENDIX II

Ar^+ ION LASER

1. DESCRIPTION

In an argon ion laser, stimulated emission between population inverted energy levels of the argon ions take place. In Fig. AII.1 the energy levels of Ar^+ ion and laser transitions are shown. The most prominent one is at 4880 $\overset{o}{A}$. The Ar^+ ion laser can be operated in the pure Ar discharge. The excitation mechanism of the lasing levels involves the multiple collision of ground state ions with the energetic electrons (4-5 eV) followed by a number of cascaded paths. The ionization and excitation of the gain medium requires heavy direct discharge within a narrow bore (segmented graphite, ceramic etc.) sustained between two high power electrodes. An axial magnetic field concentrates the discharge along the bore axis. Lasing action is sustained with the help of a resonator cavity consisting of a highly reflecting mirror and one semitransparent output mirror. The difference in the gain for different lasing lines requires different excitation conditions. For Carl Zeiss model ILA 120 Ar^+ ion laser, the threshold current and maximum power output are given in Table AII.1. The power for 5145, 5017 and 4965 $\overset{o}{A}$ laser lines increases with decreasing magnetic field while
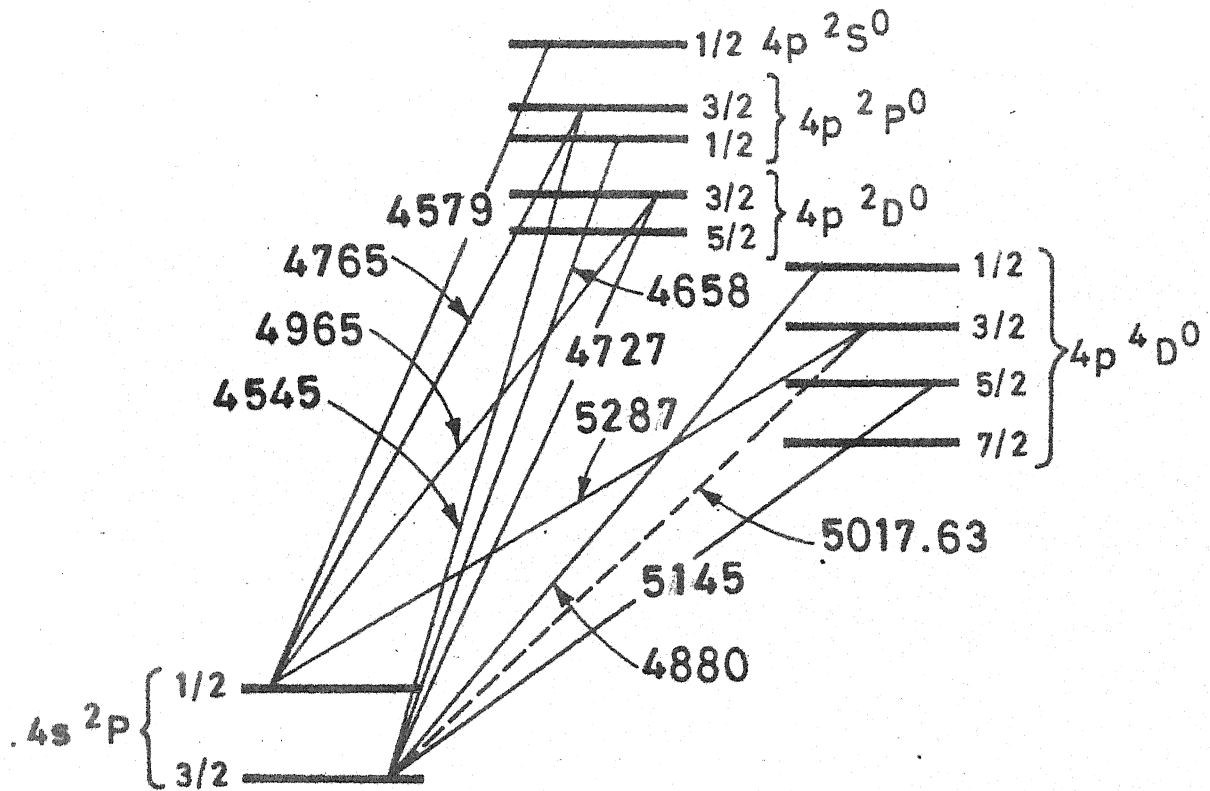
Fig.A-II.1 Energy levels of Ar$^+$ and laser transitions.
(taken from "Quantum electronics" by A Yariv)

APPENDIX II

Table A-II.1

Threshold current and maximum output power for various laser lines.

Lasing line wavelength ($\overset{o}{A}$)	Threshold current (Amps)	Maximum output power (m Watts)
4579	13.5	250
4727	16.5	180
4765	11.5	600
4880	10.0	1700
4965	12.0	450
5017	17.5	240
5145	15.5	1500

for other lines the power increases with the increase
in magnetic field. Optimum setting for the magnet
current is 5 Amps. The plasma tube and the solenoid
are coaxially mounted and are water cooled to dissipate
heat. Due to hard water usage the scale builds up in
the cooling jacket. Scale can be partially removed by
circulating dilute acetic acid (5-7%) for three to four
hours.

2. LASER POWER SUPPLY

Excitation requirements of Carl Zeiss Model ILA 120
Ar^+ ion laser are furnished by Carl Zeiss Model NG-300
power supply which can operate between 240 - 320 volts
and for discharge currents between 10 - 30 Amp.

The 380 volts a-c.mains is fed to a 3 phase-variable
voltage rectifier bridge consisting of six thyristors.
Output voltage of the rectifier bridge can adopt any vol-
tage between 0 and E_{max} depending upon the firing angle
of the thyristors. The rectifier voltage after proper
filtering is fed to the plasma tube through a current
stabilizer. A voltage control loop whose output acts
on the control element of the thyristor keeps the voltage
tapped between the plasma tube and the current stabilizer
at a constant value. After switch-on the voltage to the
control loop rises slowly so that the capacitors are pro-
tected against over current. Desired current can be
manually adjusted between 10 Amp - 30 Amps.

Laser's magnet coil is energized by a seprate stable and low ripple power supply consisting of 3 phase half wave rectifier in star connection. Filtered d-c voltage is fed to the magnet through current stabilizer. Magnet current is adjustable between 2 - 7 Amps. The regulator passbank of supply is water cooled. The plasma tube cathode is heated for 6 minutes prior to starting. The filament current is automatically switched off when discharge current exceeds 22 amps.

The power supply incorporates a number of interlocks and display functions. Interlocks and displays are facilitated through logic gate circuitary. Following parameters are monitored which affect interlock of control circuits.

(1) Coolant flow rate

(2) Gas pressure in the plasma tube

(3) Coolant temperature in the laser head

(4) Instrument malfunctions

Breakdown of any of these parameters is indicated by the blinking of the corresponding pilot light.

For safe operation of power supply a delay circuit becomes active between switch-on and starting of the laser. After swithcing-on the main circuit the magnet coil is energized and cathode heating starts. After the heating period of 5 minutes the voltage across the filter capacitors rises to the set point of 320 volts which adds to

the take-over voltage of 50 volts. Thus a net voltage of 370 volts is applied to the plasma tube. Now on the indication of ignition,laser can be started. The electrical layout of the power supply is shown in Fig. A-II-2. Whole of the electrical circuitry is installed in five chasis units mounted in a rack one above the other.

Lowest chasis unit carries connections of mains phase and R.F. interference filter circuit.

Second chasis incorporates the water sensor switch, main circuit breaker, water inlet and outlet connections for the coolant. For cooling, the laser head and the power supply are connected in series. Three fuses are provided for protecting the thyristor starting unit against input voltage overload. A set of test points is provided in this chasis to monitor the functioning of various blocks.

Fourth unit accommodates the rest of the tube, magnet and take over circuitory.

The fifth chasis is the control unit containing 13 circuit cards, which implement all control, display and interlock functions.and mains 1.25 Amp. fuses for the control unit.
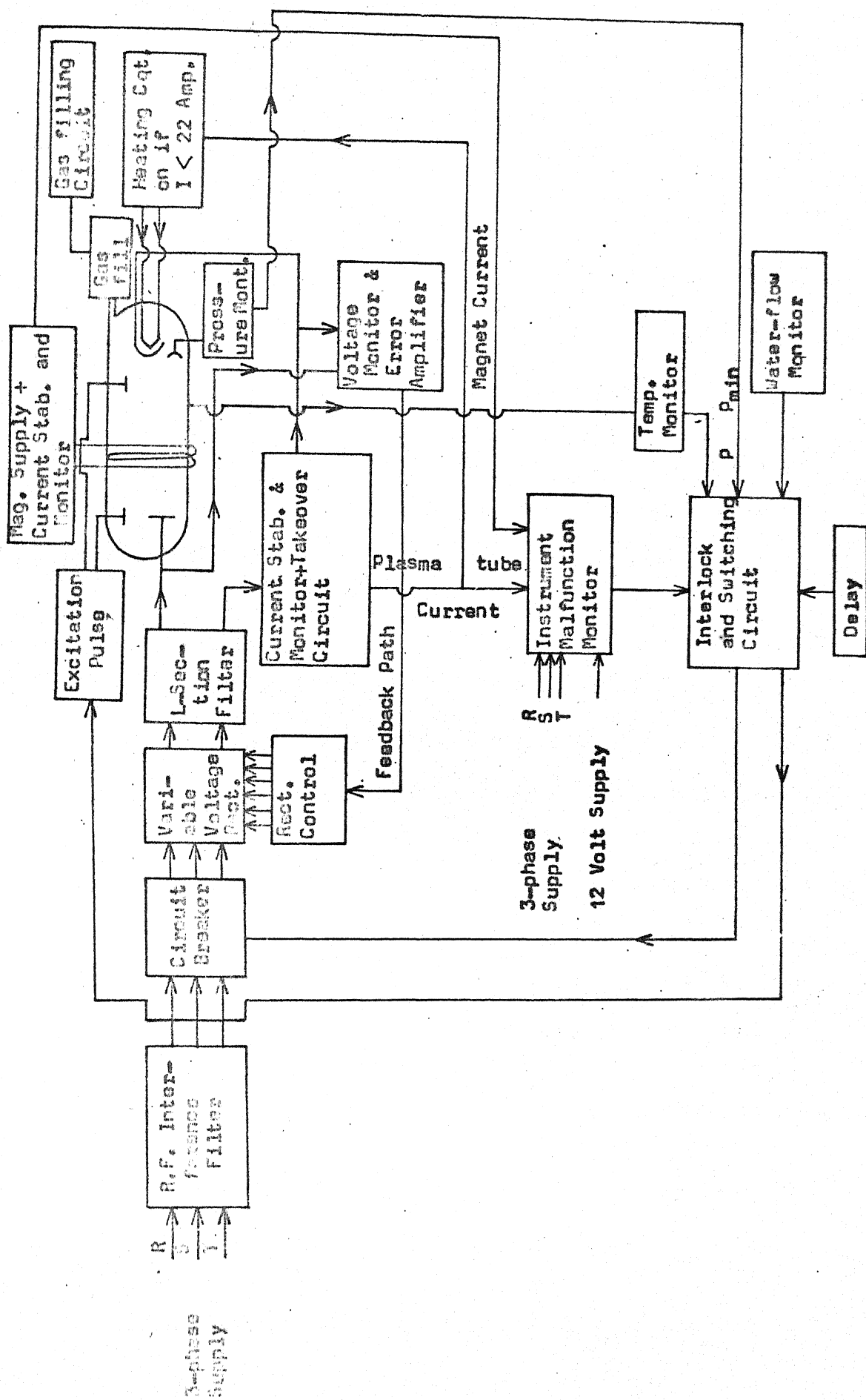
Fig. A-II-2 : Layout of the Laser Power Supply

3. OPERATION

Below we outline the procedure for starting the laser in case the laser fails to excite according to the prescribed procedure.

(A) Switch-on the power to the control unit.

(B) If all display lights illuminate steadily, switch on the mainpower circuit after the second lamp starts blinking.

(C) When the ignition light blinks after six minutes of previous operation, laser can be ignited. The ignition light will become steady. In case, the discharge is not sustained increase the magnet current in step of 0.25 Amp and try to ignite. If the laser still does not start even with maximum magnet current, monitor the gas pressure. It may be high. In such a situation, the discharge voltage should be increased very slightly (by one or two volts) but never exceeding 380 volts. Laser should now start. In case the circuit breaker breaks immediately after starting, tube voltage should be reduced a bit and the process repeated.

Caution: Firing with high voltage will result in gas pressure reduction. After the circuit breaker breaks, the voltage should be reduced. Too many consecutive strikes with high voltage might result in gas pressure

deficiency. Hence, to avoid circuit breaking many times, voltage should be increased very carefully and in the fine steps. Gas pressure should be monitored on the display meter. Alternatively it can be monitored from the discharge voltage. After 5 minutes warm up, the tube voltage should be 245 volts, if the gas pressure in the tube is sufficient.

4. TROUBLESHOOTING

Now in what follows, we will outline the trouble-shooting procedure. The flow chart in Fig.AII.3 gives the systematic approach for fault finding.

(A) If just after putting on the main switch which energise the control unit, instrument malfunction is indicated. Possible cause of the malfunction is blown fuses in one of the three phases or 12 volt power supply (to energise the control circuits).

(B) If main circuit breaker breaks just after putting on the main circuit, possible fault is with the heating cir-cuit or the magnet power supply. In case of diodes blown in the magnet supply rectifier or transistor failure in the magnet current stabilizer circuit following replacements are suggested.
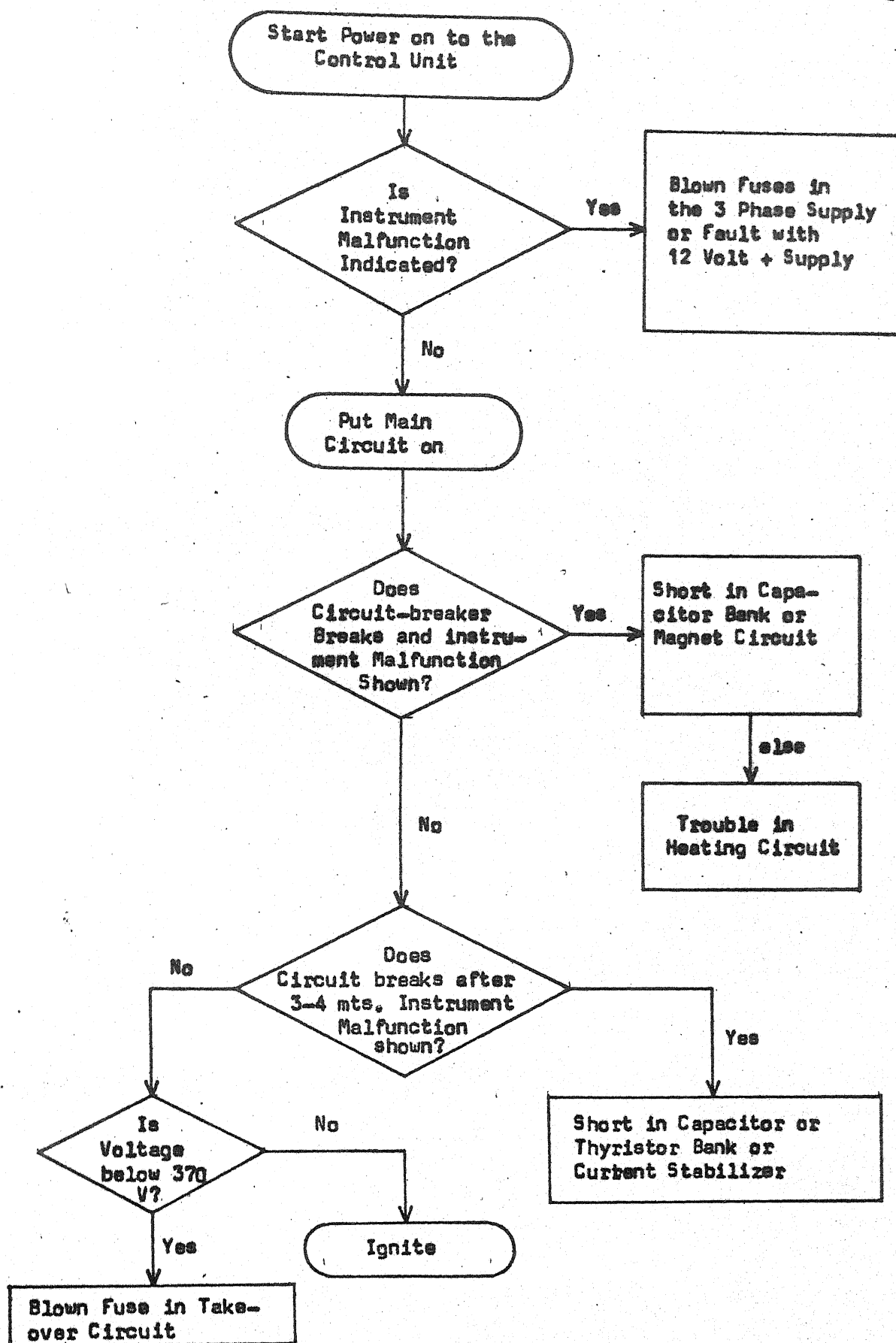
Diodes — 12SM15

Power transistor — 2N3055

Fig. A-II-3 : Flow Chart for Trouble Shooting

(C) If the circuit breaker breaks at the end of the heating time, there can be short circuit in the plasma tube supply. Possible causes of short circuit are blown thyristors or capacitor bank. Suggested replacement of the thyristors is T12F1000. In case of no faults with the thyristors and capacitor bank, the likely trouble is in the current stabilization circuit. Further by monitoring voltage at various test points and comparing the values and waveforms given in the circuit diagrams, one can exactly locate the fault.

Caution: Due to the leakage in the capacitor bank, high charging current might result in circuit breaking. This current surge can be dangerous for thyristors and hence, prolonged non use of the system should be avoided. Each time the capacitor bank is detached from the unit, it should be charged using the circuit of Fig. A II-4.

(D) Just before igniting the laser the voltage meter should show 370 ± 10 volts. In case the voltage indicated is less and is 320 volts, laser can not be started. Possible cause in the voltage reduction is the blown fuse in the take over circuit.

(E) If the output power is low, the resonator optics should be cleaned with the spectroscopic grade acetone.
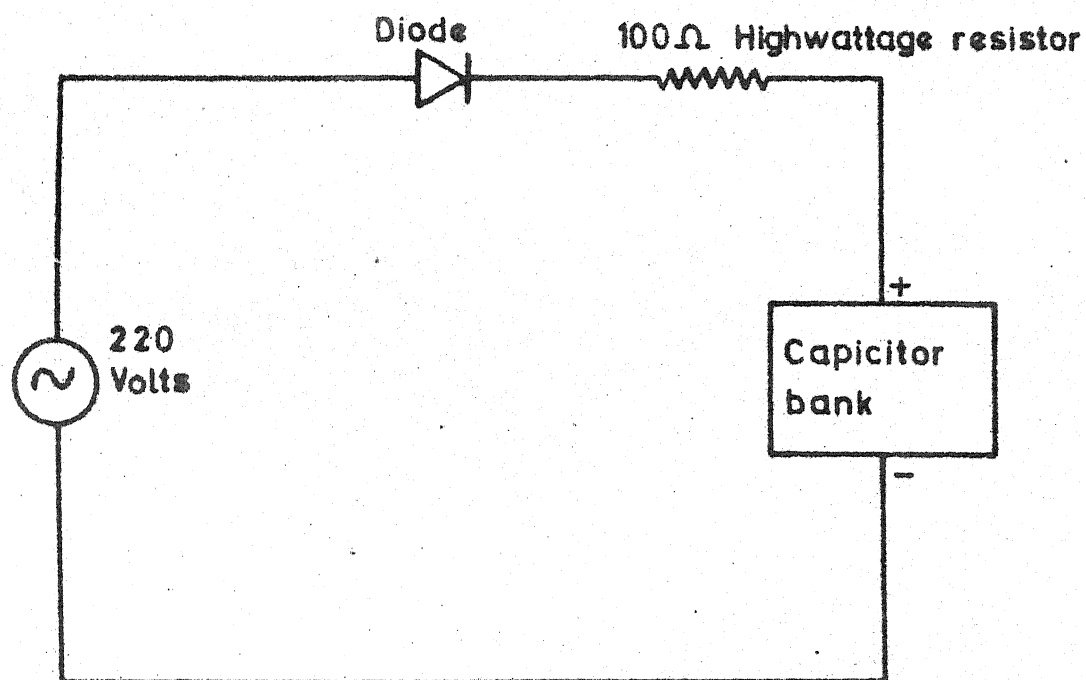
Fig. A-II.4 Capicitor bank charger.

APPENDIX III

1. PROGRAMMING OF FREE ION CALCULATIONS

For performing free ion calculations in intermediate coupling scheme, it is required to calculate the matrix elements of combined electrostatic, spin-orbit and configuration interactions. Since the Hamiltonian is real, the energy matrix will be real and symmetric. Then one needs to calculate the matrix elements along and on one side of the diagonal only. A typical matrix element is of the form

$$E(I) = E' \times A_1(I) + E^2 \times A_2(I) + E^3 \times A_3(I)$$
$$+ \zeta_{4f} \times A_4(I) + \alpha \times A_5(I) + \beta \times A_6(I)$$
$$+ \gamma \times A_7(I) \qquad \qquad ...(A3.1)$$

where $A_i(I)$ are the angular parts of the matrix elements and quantities multiplying them are the radial parts for which the usual notations have been adopted. For $4f^2$ configuration (e.g. Pr^{3+} ion) only twenty one matrix elements of this type are to be calculated. All $A_i(I)$ were stored sequentially and were then broken into sub-matrices one for each value of total angular momentum J. Matrices were diagonalized using the subroutine 'EIGEN' obtained from IBM 360 scientific subroutine package. The eigenvalues were printed out taking the energy eigen

value of the lowest level $^3H_4$ as the zero of the energy scale. Eigenvectors could be printed out whenever needed.

2. PROGRAMMING OF CRYSTAL FIELD CALCULATIONS

These calculations were done in two stages. First stage without J-J mixing and in second stage with J-J mixing.

2.1 Calculations Neglecting J-J Mixing

The expression for the crystal field Hamiltonian is

$$H_{cry}(S_4) = \sum_{k=2,4,6} B_0^k C_0^{(k)} + \sum_{k=4,6} \left[B_4^k(C_4^{(k)} + C_{-4}^{(k)}) \right.$$

$$\left. + B'^k_4(C_4^{(k)} - C_{-4}^{(k)}) \right] \qquad (A3.2)$$

To calculate the matrix elements of the crystal field Hamiltonian the following quantities were defined

$$ATOM(k) = (-1)^{S+L'+J+k} \left[(2J+1)(2J+1) \right]^{1/2} \begin{Bmatrix} J-J' & k \\ L' & L & S \end{Bmatrix}$$

$$x < f^3 U W SL \| U^{(k)} \| f^3 U'W'SL' > \qquad (A.3.3)$$

$$F(k,q) = (-1)^{J-J_z} \begin{pmatrix} J & k & J' \\ -J_z & q & J'_z \end{pmatrix} < f \| C^{(k)} \| f > \qquad .. (A3.4)$$

A matrix element is then obtained by writing $ATOM(k) \times F(k,q)$ in place of $C_q^{(k)}$ in the expression A-3.2. The quantities $<\| U^{(k)} \|>$ were taken from the

tables and 3-j and 6-j symbols were calculated using the appropriate subroutines. The crystal field energy matrix is complex. It was converted into a real symmetric matrix of twice the dimensionality. A general subroutine written for this purpose was used. The real matrix was then diagonilized using the subroutine 'Eigen'.

2.2 Calculations Including J-J Mixing

The energy matrix for the entire Hamiltonian

$$H' = H'_{Coul} + H'_{so} + H'_{config.} + H'_{cry} \qquad (A-3.5)$$

was generated by a procedure similar to those described in Sections 1 and 2.1. The resulting complex matrix is diagonalized as described in Sec. 2.1.

3. MENFUN

3.1 Source

The program was written by W. E. Humphrey at the Lawrence Radiation Laboratory[1]. This program was modified for some of its input requirements.

3.2 Purpose

To minimize a function of several variables. It can be used for the following two distinct purposes:

(a) Finding the minimum of a function of n parameters as a mathematical problem.

(b) Finding a fit for a set of experimental data to a given function by minimizing the sum of Chi-squares or the negative logrithim of maximum likelihood function.

3.3 Theory : (Procedure)

This method is based on a program presented by A.A. Tyapkin[2] at the tenth Rochester Conference (1960). It uses the Ravine stepping method for finding the minimum. The philosophy of the method has been described by I.M. Gelfand[3] without mathematical details. The minimization procedure is analogous to the one a mountaineer will adopt for exploring valleys (minima) i.e. following the river (Ravine). It would be appropriate in connection with this analogy here to quote the concluding remark of the authors of Ref. 2. "..... it seems likely that there is a link between the simplex servomechanism, blind search methods, local and nonlocal methods of automatic optimization on the one hand, and the level of motion forming in humanbeings or in higher animals, investigated for the first time by N.A. Bernshtein, on the other hand. Below the method is illustrated by the simple case of two parameters. Level lines of the function are shown in Fig. 1(a). The variable names which are used in the following discussion, appear as symbols in the Minfun. The function F, parameter vector X and derivative vector G at a given point

are labelled by the name of the corresponding point
in the Fig. 1(a).

Operation 1:   At the starting point B, the initial
direction of the search $\overrightarrow{EXVEC}$ is taken opposite to
that of the gradient i.e. $-\overrightarrow{GB}$.

Operation 2:   A step is taken from the point B to point
C such that

$$\overrightarrow{XC} = \overrightarrow{XB} + (STEP . WT) \overrightarrow{EXVEC} \qquad (A-3.6)$$

where step is the step size and WT is the scalar array
of parameters relative weights.   FC, $\overrightarrow{GC}$ are evaluated
at this point and a hyperplane is defined so as to
include $\overrightarrow{GC}$ and $\overrightarrow{EXVEC}$.   A unit vector $\overrightarrow{PERP}$ is defined
which is perpendicular to $\overrightarrow{EXVEC}$ and parallel to $-\overrightarrow{GC}$ +
Comp. $\overrightarrow{EXVEC}$, where Comp $= -GC.\overrightarrow{EXVEC}$ and is roughly the
change in F for another step of same length along BC.

Operation 3:   Along $\overrightarrow{PERP}$ a step is then taken from
point C to another point T at a distance ALPHM, which
is of the order of twice the step size and is determined
by the program, in the following manner

$$\overrightarrow{XT} = \overrightarrow{XC} + (ALPHM . WT) \overrightarrow{PERP} \qquad (A-3.7)$$

In the ideal case the direction CT will cross a ravine.
A point A now can be found at a distance ALPH from point
C on the parabola passing through the point C and T, such
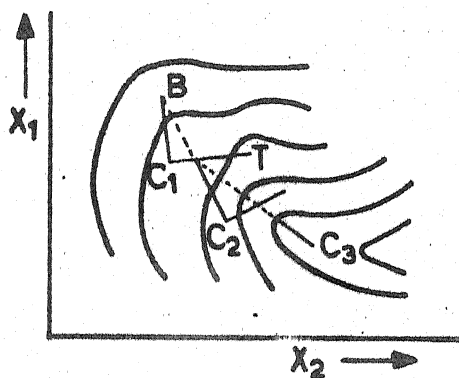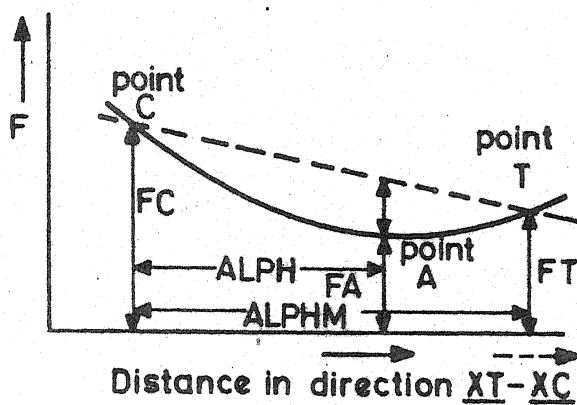that FA is less than FC and FT.   Point A now becomes the

Fig.1(a)

Fig.1(b)
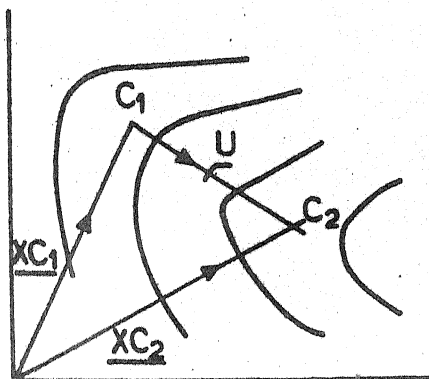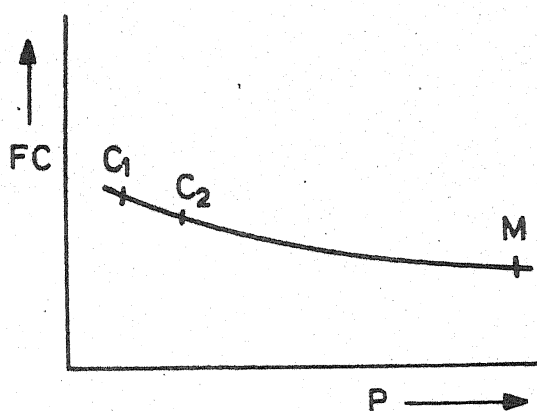
Fig.1(c)

Fig.1(d)

Fig. A-III.1

LEVEL- LINES AND
RAVINE METHOD

new starting point. A new $\overrightarrow{EXVEC}$ is defined as a unit
vector in the direction of $(\overrightarrow{XA} - \overrightarrow{XB})$ and the whole
process is repeated from operation 2, leading to the
points C_2, C_3 etc. If FA is not a new minimum then
the control is returned to the beginning of the current
operation with ALPHM half of it previous value. If
during a step ALPHM becomes more than twice the step
size then the present step is shelved, and a new step
starts along $\overrightarrow{GC}$ from point C. In order to speed up the
initial stages of the search, the program also uses an
alternative method of minimization (can be called as
'multiple stepping ravine' method.) which departs from
the certain stage of the normal method. The program
keeps a note of function values FC, the parameters $\overrightarrow{XC}$
and the gradients $\overrightarrow{GC}$ for successive points of type C.
An attempt is made to fit a parabola through the values
FC_1 and FC_2 in a special way so as to find another point,
as far away as possible, which would give yet lower value
of the function. Tests are made at each stage, if results
are not acceptable the control is returned to the original
method. As shown in Fig. 1(c) a unit vector U is in the
direction $\overrightarrow{XC_2} - \overrightarrow{XC_1}$ and variable p is defined as a scalar
product $\overrightarrow{XC} \cdot \overrightarrow{U}$. Assuming the quadratic relationship
between FC and p as below

$$FC(p) = a_3 p^2 + a_2 p + a_1 \qquad (A-3.8)$$

This is shown in Fig. 1(d). Now let the point M on the line $C_1 C_2$ give the minimum FM i.e.

$$FM = a_1 - \frac{a_2^2}{4a_3} \quad \text{at } p = -a_2/2a_3 \quad (A-3.9)$$

The curvature at M is $2a_3$, along the length of the ravine. A least squares fit to a parabola through C_1 and C_2, taking the gradients $\overrightarrow{GC_1}$ and $\overrightarrow{GC_2}$ also into account, is made to determine coefficients a_1, a_2 and a_3. Once M is found the fit is repeated with the three points C_1, C_2, M and their gradients and a new minimum point V is determined. An estimate of the equivalent number of steps is given by

$$STPS = |\overrightarrow{XM} - \overrightarrow{XC_2}| / STEP \quad (A-3.10)$$

and the direction of the ravine is given by the normalized vector EXV parallel to $(\overrightarrow{XM} - \overrightarrow{XC_2})$.

The program has two modes. In convergence mode it finds out a minimum and then terminates while in the search mode it just explores a region of the parameter space without converging. At the end of the convergence run it carries out an error analysis which is applicable for the purpose (b) only. The theory of error analysis has been discussed by J. Ovear[4].

3.4 Error Analysis

Let X be the parameter vector for the minimum, F the function value and δX the current value of the increments. (if minfun is doing the differentiation numerically). Now since $\partial F/\partial x_i(\underline{X}) = 0$ at the minimum, the differential relation

$$d(\partial F/\partial x_i) = \sum_{j=1}^{N} \frac{\partial^2 F}{\partial x_i \partial x_j} dx_j \qquad (A-3.11)$$

will reduce to the following set of simultaneous equation upon the replacement of differentials by finite differences

$$\delta F = E \delta X \qquad (A-3.12)$$

where δF is a vector defined as

$$\delta F_i = \frac{\partial F}{\partial x_i}(X, \ldots X_i + \delta x_i \ldots X_n) \qquad (A-3.13)$$

and E is matrix with the following elements.

$$E_{ij} = \frac{\partial^2 F}{\partial x_i \partial x_j} \qquad (A-3.14)$$

These equations can be solved to give

$$\delta X = E^{-1} \delta F \qquad (A-3.15)$$

It can then be shown that the standard deviations in $\underline{X}$ are

$$\sigma_i = \sqrt{2 \, E_{ii}^{-1}} \qquad (A-3.16)$$

Minfun checks whether $\underline{X} - \underline{\delta X}$ will give a new minimum and then repeats the process in the second pass with a new $\underline{\delta X}$ such that

$$\delta X_i = \sqrt{E_{ii}}^{-1} \qquad (A\text{-}3.17)$$

3.5 Input Parameters

Following inputs are required by the program :

1. ISWS (1-6): Each element of this array controls the corresponding sense switch and can have the value 0 or 1. For details see Table (AIII-1).

2. NPAR: Number of variable parameters n of function.

3. NSTEP: The maximum number of steps for this run.

4. STEP: Magnitude of the step for ravine stepping method. If STEP is positive, search mode is used. If STEP is negative, convergence mode is used. If STEP is zero, it is put = +1.0 by the program.

5. F SI. The tolerance. Normally it is zero. In the converging mode, if the function does not change by more than this amount for each of eleven consecutive steps, the run is terminated.

6. X: The starting values of the parameters.

TABLE A-III-1

Sense Switches

Value of i option No.	Comment
1	= 0 for maximum liklihood function = 1 for chi-squared function This affects only the error analysis.
2	not referenced—may be set to zero
3	Different minimizing procedures will be used by MINFUN, subject to certain tests, in order to give quicker convergence.
4	Error analysis is carried out at termination of run, including the error matrix and estimates of standard deviations of parameters. This option must not be used in the searching mode, as the error analysis is then carried out for the last point reached, and not at the minimum.
5	Additional intermediate print-out is produced, describing each new maximum and minimum as it is discovered; and giving summary tables with graphs of the function and each parameter over each group of 50 steps.
6	= 0 for end of run = 1 if data follows

7. WT: The weighting factors corresponding to the
           changes in the above parameters. These
           must be nonzero. However, we have noticed
           that a proper choice of weighting factors
           is very important for an efficient and
           successful run of the minimization routine.
                This point has been discussed in
           details in the next section.

8. DIRIN: The initial direction for the first step.
           The individual elements of this vector may
           be of any size, as they are normalized by
           Minfun. However, their signs are taken into
           account. These may be put as zeros, if no
           special direction is required.

9. FCNDATA: Data for the input to FCN subroutine, if any.

3.6 Modifications

     Since no rigid criterion was available for the
choice of WT's in help of Minfun. Following criterion
was evolved. The significance of the weighting factors,
WT's, in the program is as follows. The change in each
parameter at every step is proportional to the product
of the corresponding weight and the value of STEP.
Hence, if the function is known to vary more rapidly

with respect to some parameters, the corresponding weights
should be small so that all the parameters are treated on
equal footings. Thus the weight of the parameters refer
to their relative increments required to carry out the
same change in the function value for the variation of
each parameter. Let us consider the following differen-
tial relation (first-order approximation of Taylor's
series)

$$\delta F_\lambda = \delta X_\lambda \, \text{grad}_\lambda \, F \qquad (A\text{-}3.18)$$

where $\lambda = 1,2,3 \ldots i-1, i, i+1, \ldots n$,

$$\delta X_\lambda \equiv (X_\lambda - X_{0\lambda}) \text{ is the increment}$$

(uncertainty) in the λth parameter, δF_λ is the corres-
ponding change in the function value and

$$\text{grad} \; F_\lambda \equiv F'(X_\lambda) = \partial F / \partial X_\lambda \qquad (A\text{-}3.19)$$

Thus the weights (relative iuncertainties, μ_λ's or rela-
tive increments of the parameters as defined above,
with respect to i-th parameter will be

$$\mu_\lambda \equiv \frac{\delta X}{\delta X_i} = \frac{\text{grad}_i \, F}{\text{grad}_\lambda \, F} \qquad (A\text{-}3.20)$$

Depending upon the magnitude of $\text{grad}_i F$ (derivative of
the parameter chosen as basis), the search will be coarse
or fine. The program was modified so as to generate the
WT's internally. For this the derivative are typed on

the terminal and user is asked to specify the basis

parameter, depending upon his choice for the nature

of search (coarse or fine). Since no specific direc-

tion is required for the first step, the vector DIRIN

was set to zero in the program. Thus no input data for

WT's and DIRIN was required by the modified version of

the program.

REFERENCES

1. W.E. Humphrey, "A general minimizing routine - Minfun", Programmer's Notes P-6, 9.7.62, UCRL Berkley.

2. A.A. Tyapkin, "Phase shift analysis of p-p scattering", Proceedings of 10th Rochester Conference, pp 138-140 (1960).

3. I.M. Gelfand and M.L. Tsetlin "The principle of nonlocal search in automatic optimization systems.

4. J. Orear, "Notes on statistics for physicists", UCRL, 8417, Berkley.

"............. And those structures
and theories which man calls knowledge
and art are naught except shackles
and golden chains which man drags,
and he rejoices with their glittering
reflections and ringing sounds".

                            _ Khalil Gibran

PHY-1983-D-SIN-SPE